

Business Jet Design Using Laminar Flow

Thesis Report
J.Y. Boersma

Delft University of Technology



Cover image: www.dassaultfalcon.com

Business Jet Design Using Laminar Flow

Thesis Report

by

J.Y. Boersma

to obtain the degree of Master of Science
at the Delft University of Technology,
to be defended publicly on Friday November 18, 2016 at 13.30.

Student number:	4009525	
Project duration:	February, 2015 – November, 2016	
Thesis registration nr.:	101 # 16 # MT # FPP	
Thesis committee:	Prof. dr. ir. L. L. M. Veldhuis,	TU Delft, supervisor
	Dr. ir. M. Kotsonis,	TU Delft
	ir. K. J. Groot,	TU Delft

An electronic version of this thesis is available at <http://repository.tudelft.nl/>.

Preface

At the culmination of several years of attending Delft University, the MSc graduation at the department of Flight Performance & Propulsion seems as quite a challenge. Not because it is an insurmountable task, but simply by how it presents itself; an unfamiliar format. The skills I acquired during my education have to be synthesized in one grand product. Not unsurprisingly to people who know me, I responded to this challenge by diving in headfirst.

The first impression that stuck with me when embarking on the almost two year project, was the intended nature of the thesis: The first possibility for a student to contribute to the body of knowledge of his scientific field. In retrospect, such a prospect is tantamount to failure considering the state of the art within aerospace. What might seem like a stagnation in aircraft design over the past decades in the conventional 'tube-and-wing' concept obscures the incremental improvements that push the performance of aircraft ever further. Knowing this, what is the healthy choice regarding a graduation topic? One the one hand, why not remaining in shallow waters and verify existing knowledge, proving your capacity to perform research? One the other, why not test the limits of your abilities and see what you find at the deep end?

By diving in headfirst, I refer to the initial project plan in which the prospect of laminar flow on the empennage of a Dassault business jet was to be investigated. The first draft, following an extensive (both in content and time) literature study, was a naive proposal to create a brand new program to compute my way out of this. This was in addition to a plan to overhaul the Initiator, a conceptual aircraft design tool, to implement business jets and improve its accuracy. After several months of inevitable delay, I was guided into the direction of the Aerodynamics department of our faculty with the silent advice to not reinvent the wheel. This proved to be a great step forwards in the progress of the thesis but simultaneously more than doubled the time I would spend on my graduation.

Under the close guidance of people who understood the complexities of laminar flow, the research started to take shape. Approximately one year after starting my graduation the finishing line came into view, just before I was invited to join in a new project: A cooperation between Delft and the Brazilian aircraft manufacturer Embraer, who intend to apply laminar flow in their future designs. The goals of this venture and my own work were surprisingly similar and I soon found myself being financially compensated for graduating. Fast-forward to September of my final year in which I joined a delegation to Embraer's facilities in São José dos Campos. There I spend three weeks to successfully implement a new laminar flow toolbox into the company's optimization framework. Needless to say, the deep end did not turn out so bad after all.

I can wholeheartedly say that I enjoyed my time as a student in Delft. In an atmosphere of curiosity and ambition I believe to have grown as both a person and a professional. Over the course of the thesis project I have enjoyed the company and relied upon the support of multiple persons. I would like to address these people in acknowledging their contribution to the work that is presented in this report.

The unwavering support of my family and friends has been invaluable and my gratitude goes without question. Particularly for graduation, the pleasant people and welcome environment of 'Kamertje 1' has been very motivational. I do not think I would have been as productive anywhere else, or accomplished as much for both the Initiator and my own work.

I would like to thank my supervisors, starting with Leo Veldhuis and Mark Voskuijl for not saying *stop* when I overburdened myself but giving me the opportunity to find my own way. In addition, I am grateful for the close cooperation with Marios Kotsonis and Koen Groot, for the incredibly mentorship and unlimited motivation that were instrumental in finishing this work. Also, I have been very fortunate in being invited to join the collaboration with Embraer, which would not have happened were it not for your confidence in my contributions.

*J.Y. Boersma
Delft, November 2016*

Abstract

The design of more efficient aircraft is a prevalent research topic in aerospace. It is related to the reduction of fuel burn, important for the demand of low emissions and costs. As efficiency is linked to aerodynamic performance, the drag of aircraft is to be lowered. Skin friction drag is a dominant drag component in conventional aircraft and is influenced by the state of the viscous boundary layer. Laminar boundary layers are known to produce less friction than the turbulent kind, so postponing the transition from laminar flow to turbulence will reduce drag. Laminar design is the goal of developing an aircraft on which boundary layer transition to turbulence is postponed in an effort to reduce the skin friction drag, increasing the aerodynamic performance and lowering the fuel burn.

Transition of the boundary layer is a complex phenomenon that might be the most researched topic in fluid dynamics. In engineering, prediction of transition has long been modeled by virtue of linear stability theory: The e^N method is used in most applications to simulate the exponential growth of small disturbances up to the breakdown of laminar flow. It is heavily reliant on proper experimental calibration, but the theory is applicable to the most common transition mechanisms. On swept wings, the crossflow (CF) and streamwise propagating Tollmien-Schlichting (TS) waves are the two flow phenomena leading to transition. To facilitate the design of laminar aircraft a framework is required to automate the stability computations for both types of instability, but other than simplified correlation methods for TS waves no such tool is available.

A new linear stability tool connects the three parts of the problem: An inviscid (edge) flow solution of an airfoil, an exact laminar boundary layer solution relating to this outer flow, and the TS and CF amplifications present in this laminar mean flow. The inviscid solution is an input to the process and can be obtained through an external solver. Using the infinite-wing assumption, the three-dimensional boundary layer flowfield is computed using a finite-difference marching scheme up to the point of separation. The velocity profiles are mapped with Chebyshev polynomials collocated at a scaled cosine distribution to minimize the number of polynomials. The amplifications are obtained by solving the spatial formulation of the Orr-Sommerfeld equation for either TS or stationary CF modes.

To automate the internal process it was required to determine the discretization of the stability calculations before any computations take place, which has been resolved by using empirical and heuristic correlations to define limits, stepsizes, etc. Also, the stability solvers required manual input to identify the correct amplification mode from a spectrum of eigenvalues for each point in the boundary layer. This made automatic calculations impossible, so a filtering procedure was developed to identify the true physical disturbance by analyzing the shape of the eigenfunctions in this spectrum. Filtering spectra on a per-case basis removed the need for mode-tracking algorithms that prevented parallel processing of the stability computations of arbitrary size. The last step of the tool is to integrate the amplifications on multiple physical frequencies to produce the N-factor curves and their envelope, which is the output of the program. The framework is found to be highly accurate, resolving the boundary layer in the vicinity of both stagnation and separation, and robust enough to be utilized in optimization frameworks.

Although the workload to obtain the N-factor envelope has reduced, the computational time for one airfoil is still significant for conceptual aircraft design. Therefore, a surrogate model of the envelopes can be created by evaluating the airfoil under a range of conditions and interpolating the results. This proved to be an excellent compromise between fidelity, accuracy and computational time. One surrogate model is only valid for one airfoil shape, but it is an acceptable drawback in the conceptual design phase.

The intention is to apply the linear stability tool to the design of business jets. These aircraft operate at lower Reynolds numbers than conventional transport aircraft but are of similar design, hence make excellent candidates to attempt laminar design. The conceptual design program *Initiator* has been thoroughly updated in accuracy and expanded with the capability to model business jets. In addition, the differences between conventional and business jet design were investigated to assess the limits of empirical sizing methods. As such it is possible to reproduce reference aircraft and modify their design for laminar flow to quantify the sensitivities of the main aircraft design parameters with respect to a reduction in drag.

Regarding design of business jets, the empirical methods used for conventional aircraft were found to be appropriate, although it is advised to investigate the use of additional scaling factors. Also, the influence of fuselage fuel storage and the shifts of center of gravity were experienced to be more stringent design requirements. Finally, the influence of laminar flow on aircraft design was investigated with Initiator. The correlation between an increase of laminar flow and reduction in zero-lift drag was quantified, resulting in a remarkable similarity between different aircraft sizes. Also, it was found that the primary applicability of laminar flow were long haul, smaller aircraft, because the fuel burn per unit of payload per unit range was impacted more for these mission types.

Contents

Preface	iii
Abstract	v
List of Figures	ix
Glossary	xi
1 Introduction	1
1.1 Laminar flow	1
1.2 Boundary layer stability.	2
1.3 Swept wings.	4
1.4 Boundary layer crossflow	5
1.5 Aircraft design	7
1.6 Business jet design	8
1.7 Research plan	9
1.8 Thesis structure.	9
2 Linear stability tool	11
2.1 Overview	11
2.2 Boundary layer code	12
2.2.1 Boundary layer solver	12
2.2.2 Crank-Nicolson	13
2.2.3 Infinite wing assumption	14
2.2.4 Leading edge singularity	14
2.3 Orr-Sommerfeld	15
2.3.1 Spectrum	16
2.3.2 Mapping of collocation points	17
2.4 Eigenfunction filtering	19
2.4.1 Utility	19
2.4.2 Eigenfunctions.	19
2.4.3 Filters	23
2.5 Pre-process	24
2.5.1 Critical Reynolds number	24
2.5.2 Wall curvature error	25
2.5.3 Reynolds number stepsizes	25
2.6 Verification	26
2.6.1 Flat plate.	26
2.6.2 Falkner-Skan.	28
2.6.3 Similarity	30
3 Case study	33
3.1 HSNLF(1)-0213 airfoil.	33
3.1.1 Pressure distribution.	33
3.2 Boundary layer solution.	34
3.3 Stability solver preparation	36
3.3.1 Wall curvature	36
3.3.2 Critical Reynolds number	36
3.3.3 Grids.	36

3.4	Stability solver solution	37
3.5	N-factor.	38
3.5.1	N-curves	38
3.5.2	Envelope.	39
3.6	Transition.	40
3.6.1	Setup.	41
3.6.2	Observations.	41
3.7	Surrogate model	43
3.7.1	Variables	43
3.7.2	Discretization	43
3.7.3	Results	44
3.7.4	Utility	44
4	Aircraft design	47
4.1	Fuselage design	47
4.1.1	Cabin design	47
4.1.2	Inside-out optimization	49
4.1.3	External geometry	49
4.1.4	Cargo	50
4.1.5	Fuel tank.	50
4.2	Airfoil definition	51
4.2.1	Parsing.	51
4.2.2	Sampling.	52
4.2.3	Parametrization	54
4.3	Wing definition	55
4.4	Drag polar.	56
4.4.1	Drag breakdown	56
4.4.2	Drag module	57
4.5	Parasite Drag Estimation	57
4.5.1	Considerations.	58
4.5.2	Xfoil implementation	58
4.5.3	Zero-lift drag coefficient	59
4.5.4	Enhanced drag polar.	60
4.6	Initiator results	62
4.6.1	Baseline aircraft	62
4.6.2	Embraer Phenom 300	64
4.6.3	Business jet convergence	66
4.7	Laminar Results.	68
4.7.1	Embraer Phenom 300	68
4.7.2	Trendlines	68
5	Conclusions and Recommendations	71
5.1	Conclusions.	71
5.2	Recommendations	72
A	Aircraft database	79
B	Initiator modifications	81
C	Initiator results	85
D	Eigenfunction mapping study	87

List of Figures

1.1	Difference in velocity profile between laminar and turbulent boundary layers [5]	1
1.2	N-factor envelope for a flat plate boundary layer [13]	2
1.3	Attachment line	3
1.4	Concave surfaces	3
1.5	Infinite wing reference frames	4
1.6	Three dimensional flow of boundary layers	6
1.7	Typical drag breakdown of transport aircraft [27]	7
1.8	MTOM fractions comparisons between conventional and business jets	8
1.9	Cutaway of Dassault Falcon 8X showing fuel tanks in the wing-body fairing [33]	9
1.10	Technical structure of the thesis	10
2.1	Linear stability tool flowchart	12
2.2	Boundary layer solver grid	12
2.3	Effect of inflow averaging on the velocity profile curvature at the wall.	15
2.4	Eigenvalue spectrum of the Orr-Sommerfeld equation	17
2.5	Characteristic cross-flow velocity profile	17
2.6	Mapping example using $y_{max} = 50$ and $y_i = 10$	18
2.7	Drift of eigenvalue with increasing number of polynomials	19
2.8	Characteristic branches of the eigenvalue spectrum	20
2.9	Characteristic eigenfunctions shapes	20
2.10	Application of the eigenfunction filters	22
2.11	Critical Re_{δ^*} versus shape factor [21]	24
2.12	Comparison of Re_{δ^*} solution with the critical Re_{δ^*} from the shape factor correlation	24
2.13	Variation of amplification with ω of TS instability at various Reynolds numbers	25
2.14	Estimate of interpolation error of the N-curves	26
2.15	Solution to the Blasius equation	27
2.16	Error in solver velocity profiles compared to Blasius similar solution	28
2.17	Stability diagram of Blasius profile	28
2.18	Solutions to the Falkner-Skan(-Cooke) equations	29
2.19	Error in solver velocity profiles compared to Falkner-Skan similar solution	30
2.20	Falkner-Skan stability diagram neutral curves	31
2.21	Falkner-Skan-Cooke similar solution in the inviscid streamline reference frame	31
3.1	HSNLF(1)-0213 airfoil definition	33
3.2	HSNLF(1)-0213 airfoil with pressure coefficient distributions	34
3.3	Wall force imbalance by comparison of wall curvature of input and solution	35
3.4	Boundary layer characteristic thicknesses	35
3.5	Boundary layer profiles at six separate stations	36
3.6	Critical Reynolds number comparison	37
3.7	Stability tool preparation grid spacing	37
3.8	Stability solver grid structure to discretize the parameter space	38
3.9	Example of an integration path of a physical frequency ω for TS instability N-curves	39
3.10	Collection of N-curves per type of stability	40
3.11	N-factor envelopes over the airfoil chord length for both surfaces	40
3.12	$N_{TS} - N_{CF}$ diagram constructed from the ELFIN projects [43]	41
3.13	Transition locations on both surfaces of both types of instability for three different critical N-factors	42
3.14	Surrogate model parameters	43
3.15	N-factor contours of the Embraer Phenom 300 wing in cruise flight using the HSNLF airfoil	45

3.16 N-factor contours of the Learjet 45 wing in cruise flight using the HSNLF airfoil	45
4.1 Cabin layouts generated for several reference aircraft	48
4.2 Inside-out optimization parameters and constraints applied to an Airbus A380 [48]	49
4.3 External geometry creation of the Airbus A320-200	50
4.4 Geometry of freight bay and fuselage tank in an Embraer Phenom 300	51
4.5 Initiator airfoil class UML definition	51
4.6 Closed airfoil check by excluding trailing edge from original airfoil data set	52
4.7 NACA 23012 airfoil camber line from linear interpolation	53
4.8 NACA 23012 airfoil coordinate transformation	53
4.9 NACA 23012 airfoil detailed sampling result	54
4.10 Errors when fitting an airfoil using CST or Bezier splines using 5 degrees of freedom	54
4.11 Wing class definition, including get and set relations with Airfoil class	55
4.12 Empirical Drag Estimation drag polars of a G650	56
4.13 Drag Module drag polars of a G650	57
4.14 Parasite Drag Estimation drag polars of a G650	58
4.15 Xfoil analysis of HSNLF airfoil on the main wing of a G650	59
4.16 Airfoil thickness location correction factor	60
4.17 Lifting surface correction factor	61
4.18 Wing-body interference factor, figure 4.1 from Roskam Part VI [27]	61
4.19 Comparison of maximum take-off mass results of the Initiator	62
4.20 Baseline aircraft [48]	63
4.21 Reconstruction of the Embraer Phenom 300 geometry by the Initiator	64
4.22 Design point for the Phenom 300 in the wing-thrust loading diagram	65
4.23 Payload-range diagram for the Phenom 300	66
4.24 Class 2 weight estimation breakdown for the Phenom 300 using Torenbeek and EMWET	66
4.25 Drag polars for Phenom 300	67
4.26 Comparison of business jet results of the Initiator with reference aircraft	67
4.27 Surfaces of the aircraft with increased laminar flow	68
4.28 Aircraft results regarding C_{D0}	69
4.29 Decrease in fuel burn, reduced by payload and range, normalized by turbulent reference	70
B.1 Initiator design convergence progress of an Airbus A320-200	82
B.2 Non-convergence of the MTOM in the Learjet 45 model	83
B.3 Initiator design convergence N2 chart	84
D.1 NC parameter convergence 1	88
D.2 y_{max} parameter convergence 1	88
D.3 y_i parameter convergence 1	89
D.4 NC parameter convergence 2	89
D.5 y_{max} parameter convergence 2	90
D.6 y_i parameter convergence 2	90

Glossary

Acronyms

APU	Auxiliary Power Unit
CF	Cross Flow
CG	Center of Gravity
CST	Class-function Shape-function Transformation
DATCOM	Data Compendium
DUT	Delft University of Technology
EDE	Empirical Drag Estimation
ELFIN	European Laminar Flow Investigation
EMWET	Elham Modified Weight Estimation Technique
FAR	Federal Aviation Regulations
FSC	Falkner-Skan-Cooke
FF	Fuel Fraction
HSNLF	High Speed Natural Laminar Flow
LE	Leading Edge
MAC	Mean Aerodynamic Chord
MGC	Mean Geometric Chord
MTOM	Maximum Take-Off Mass
NACA	National Advisory Committee for Aeronautics
OEM	Operative Empty Mass
PM	Payload Mass
PDE	Parasite Drag Estimation
PSE	Protuberances, Surface roughness & Excrescences
TDMA	Tri-Diagonal Matrix Algorithm
TE	Trailing Edge
TLR	Top Level Requirement
TOM	Take-Off Mass
TS	Tollmien-Schlichting
XML	eXtensible Markup Language

Symbols

Symbol	Units	Description
A / a	-	TDMA coefficient
A	-	aspect ratio
a	-	wave amplitude
$B / \bar{B} / b$	-	TDMA coefficient
	m/s	speed of sound
b	m	wing span
C / c	-	(TDMA) coefficient
c	m	chord
	m/s	climb speed
D / d	$N / (N/m)$	drag
		TDMA coefficient
d	-	derivative
e	-	Oswald factor (efficiency factor)
f	-	Blasius function
	-	Falkner-Skan function

g	-	Cooke function
H	-	shape factor
i	-	index along x
j	-	index along y
K	-	constant
k	-	absolute wavenumber
	-	constant
L / l	$N / (N/m)$	lift
L	m	length
	-	thickness correction factor
l	m	Blasius length scale
M	-	Mach number
m	-	Falkner-Skan parameter
N	-	amplification factor
NC	-	number of Chebyshev polynomials
n	-	number of nodes
	-	loading factor
O	-	order
Q	m/s	velocity in freestream
Re	-	Reynolds number
S	m^2	surface area
	m	starting point
s	m	field length
Tu	-	turbulence
t	s	time
	m	thickness
U / u	m/s	velocity along X
V / v	m/s	velocity along Y
W / w	m/s	velocity along Z
W	kg	weight
X / x	m	dimension along the chord
Y / y	m	dimension normal to the surface
Z / z	m	dimension along the span

Greek symbols

Symbol	Units	Description
α	-	wave number, chord-wise
	deg, rad	angle of attack
β	-	wave number, span-wise
	-	Hartree parameter
Δ	-	finite step
δ	m	boundary layer thickness
∂	-	partial derivative
η	-	normalized y coordinate
θ	m	momentum thickness
	rad	angle
Λ	deg, rad	sweep angle
λ	m	wavelength
μ	$kg/(m \cdot s)$	dynamic viscosity
ν	m^2/s	kinematic viscosity
ρ	kg/m^3	density (of air)
σ		growth ratio
τ	N/m	shear stress
Φ	rad	phase angle
ϕ		amplitude function
ψ		stream function
ω	s^{-1}, Hz	wave frequency

Sub- & Superscripts

Symbol	Description
*	displacement thickness
0	point of neutral stability
	zero-lift
99	boundary layer thickness
cr	cruise
$crit$	critical
e	edge
f	friction
i	imaginary
	induced
	intermediate point
L	landing
ls	lifting-surface
m	maximum thickness line
max	maximum point
p	pressure
r	real
s	streamline
TO	Take-Off
tr	transition
w	wave
wb	wing-body
wet	wetted
∞	infinity

Introduction

Within aircraft design it is essential to improve the performance of aircraft to increase their profitability and allow airlines to remain competitive. Due to well known global phenomena such as climate change, the volatile price of oil and an the exponentially growing aviation sector, prioritizing environmental factors is becoming more and more on par with profitability. As a result, a renewed focus is placed on reducing not only cost, but also noise and emissions, thereby redefining the idea of an optimized aircraft.

Large collaborative research projects such as the European CleanSky program are meant to reinvigorate the sector and meet these new goals [1, 2]. Various technologies are available to provide the necessary changes in aircraft design in accordance with this new paradigm. In terms of performance, new aircraft configurations such as blended-wing bodies and Prandtl planes are examples of very fundamental solutions that promise large improvements [3, 4]. These revolutionary concepts are not yet broadly produced or are to become prevalent in the near future, because they are either still in a conceptual state or have practical limitations. As such, more conventional solutions are needed for the fleet of conventional aircraft currently in operation. One of these options is the use of laminar flow technology to reduce the aerodynamic drag of aircraft.

1.1. Laminar flow

Extending laminar flow in boundary layers by either active or passive means is one of the most researched areas in aeronautics and is known to provide significant drag reduction [6, 7]. It uses the principle of postponing boundary layer transition from laminar to turbulent flow to reduce *skin friction* drag. While this is in essence a simple concept, it suffers from a number of practical limitations and requires intricate design methods for modern transport aircraft. However, it already sees use on simpler aircraft such as sailplanes where such limitations are smaller or and lower drag is of higher importance [8]. The reduction in drag from laminar flow relies on the difference of the velocity profile gradient at the surface between laminar and turbulent boundary layers, see figure 1.1.

$$\tau = \mu \left(\frac{dU}{dy} \right) \quad (1.1)$$

Compared to the laminar flow, the turbulent profile has a higher velocity gradient at the wall, due to the mixing of fast and slow moving fluid along the height of the boundary layer. Although this can be beneficial for postponing boundary layer separation, the higher gradient leads to a higher friction drag, according to equation 1.1. The velocity defined as U has a high gradient perpendicular to the wall (along y) to meet the no-slip condition. By definition, the shear stress at the wall τ is obtained by multiplication with the dynamic viscosity μ [5]. The integral of τ over the length of the surface results in the total skin friction, which will be therefore be

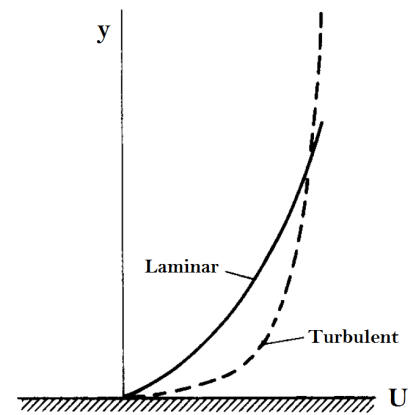


Figure 1.1: Difference in velocity profile between laminar and turbulent boundary layers [5]

proportional to the gradient of the velocity profiles within the boundary layer. Hence, postponing laminar to turbulent transition will reduce the skin friction drag. On aircraft such as sailplanes, this can be adequately accomplished by shaping the profiles of the wing. Placing the point of maximum thickness more aft is a common design rule for laminar airfoils. This creates a favorable, negative pressure gradient that will locally increase shear stress but is inherently *stable* for two-dimensional flow, thereby preventing transition to turbulence and even higher shear stresses.

Unfortunately, there are significant hurdles to overcome before laminar flow technology can be applied to conventional transport aircraft [9]. To achieve reliable laminar flow a wing has to be manufactured to rigorous standards to avoid early transition from roughness and waviness of the surface. Also, contamination of the wing surface by bugs, dust or ice accretion makes durable, day-to-day application a struggle. Then, the poorly understood concept of receptivity, in which external effects such as sound can influence the boundary layer state, can invalidate any careful theoretical analysis that did not include these effects. However, before all these complications become relevant, a laminar wing has to be designed. Under the assumption that all practical problems will be resolved, there is a clear need for a computational model. Methods based on linear stability theory are often used to quantify the stability of the boundary layer that ultimately causes transition.

1.2. Boundary layer stability

Most transition prediction methods for engineering purposes use the e^N method, originally proposed by Smith & Gamberoni and van Ingen [10, 11]. By application of linear stability theory, this method calculates the amplification of disturbances of different frequencies throughout the boundary layer. The integral of these amplifications with respect to the first point of neutral stability is referred to as the *N-factor*, see figure 1.2. There are several strategies in which these amplifications can be integrated, leading to different results [12]. Transition has experimentally been observed to occur at relatively constant values of this N-factor, if corrected for effects such as turbulence, roughness, etc. Originally, a consensus on a *critical* of $N = 9$ was formed, leading to terminology such as the e^9 method. This value is still an accepted baseline for transition in cruise flight, or low turbulence conditions [13]. For stream-wise transition mechanisms this method has been incorporated into tools such as Xfoil using fast correlation methods [14]. However, the different transition mechanisms found on swept wing boundary layers require a different approach.

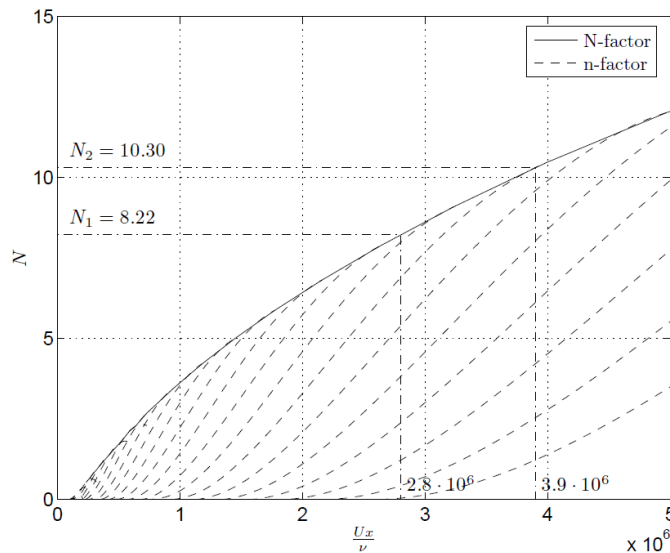


Figure 1.2: N-factor envelope for a flat plate boundary layer [13]

In general there are considered to be four types of transition mechanisms. In arbitrary order, these are streamwise, crossflow, attachment line and centrifugal instability [15].

1. Streamwise instability caused by Tollmien-Schlichting waves (TS) is a two-dimensional phenomenon. It is the type of instability predicted in the results of figure 1.2. The TS instability will be discussed in detail throughout this thesis.

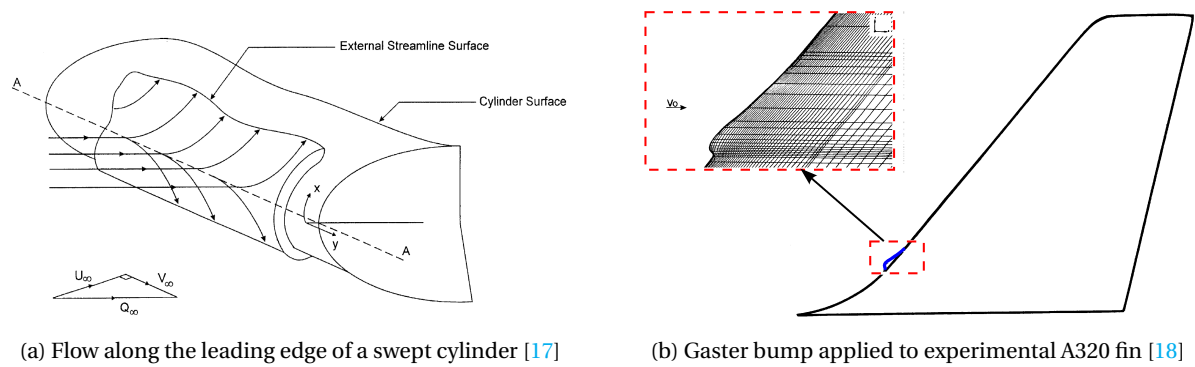
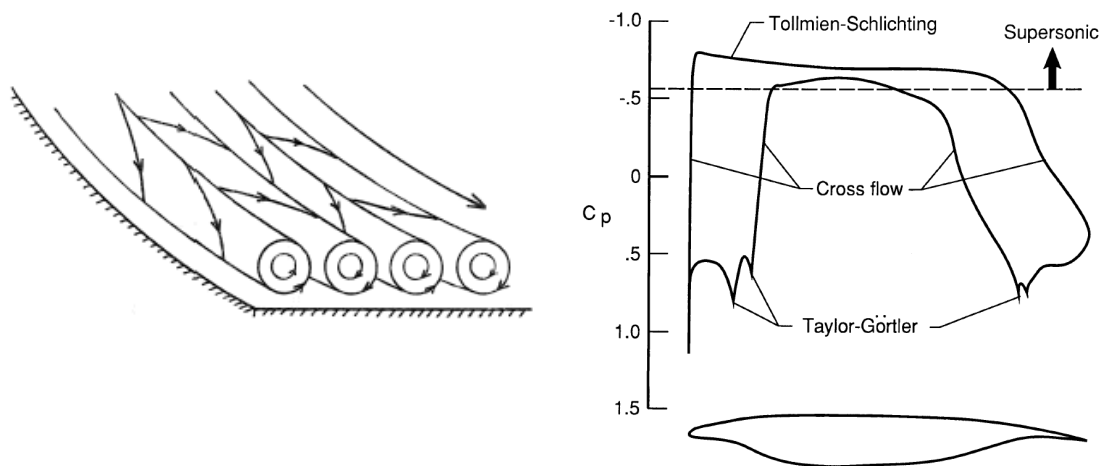


Figure 1.3: Attachment line

2. Instability from boundary layer crossflow is a result of the spanwise flow that occur because of stream-wise pressure gradients on swept wings. Depending on the receptivity of disturbances, the crossflow will result in traveling or stationary crossflow vortices, whom are approximately aligned with the inviscid streamlines. Only stationary crossflow will be considered in this report, as traveling crossflow is not expected on aircraft in cruise flight because of the low turbulence levels. The nature of boundary layer crossflow is explained in more detail below.
3. The attachment line along the leading edge of a swept wing can become unstable and transition to turbulent or transport turbulent flow from the wing root, in both cases contaminating the outboard wing, see figure 1.3a. However, this type of transition can be averted by using airfoils with a small leading edge radius to prevent transition or even using devices such as a *Gaster bump* to prevent contamination from the root [16]. An example of such a bump is given in figure 1.3b.
4. Centrifugal instability is a result of Görtler vortices that arise in the boundary layers of concave surfaces, see figure 1.4a. Although these vortices are highly unstable, concave surfaces are rarely seen in the laminar regions of conventional airfoils. An exception can be made for airfoils designed for active flow control, such as the profile in figure 1.4b. Boundary layer suction is required to maintain laminar flow in the concave parts of this design. The pressure coefficient distribution clearly shows the different types of instability originating from such a design.



(a) Gortler vortices found in the boundary layer of a concave wall [19] (b) Intentional concave airfoil design suited for active flow control [20]

Figure 1.4: Concave surfaces

While streamwise TS waves are well understood and easily modeled, it is transition from stationary cross-flow vortices that is the critical mechanism that has prevented common laminar wing design on modern transport aircraft. Hence, this type of instability will be the main focus of the work presented here. A fundamental understanding of the viscous flow over swept wings is the starting point for such a discussion.

1.3. Swept wings

As will be explained in the next section, pressure gradients perpendicular to the external, inviscid streamlines induce a crossflow within the boundary layer. These CF velocity profiles have an inflection point as a consequence of the no-slip conditions at the wall and continuity with the freestream, where the velocities per definition are equal to zero. Inflection points are a strong source of boundary layer instability and will lead to early transition at lower N-factors [21]. While fast database methods exist to predict transition in two-dimensional cases, because transition is mostly induced by planar TS waves, CF instability requires a three-dimensional boundary layer solution. Resolving the boundary layer and the stability equations for three-dimensional flow has been thoroughly researched, but practical tools to predict CF instability similar to how Xfoil models TS instability have not been found in open literature [22, 23, 24]. Frameworks created by NASA and DLR are mentioned and utilized in literature but remain confidential [25, 26].

The viscous solution of the flowfield over a three-dimensional surface like a wing requires far more computational power than a two-dimensional solution. A simplification is required to reduce the problem of laminar swept wing design to a reasonable timeframe. Three-dimensional boundary layers can be effectively approximated by assuming the swept wings to be of infinite span. Such an assumption is valid for high aspect ratio wings, excluding the vicinity of the root and tip [21]. Application of this method is illustrated in figure 1.5, where the reference frame is aligned with the leading edge. That is, x and U are perpendicular to the leading edge while z and W are parallel to it.

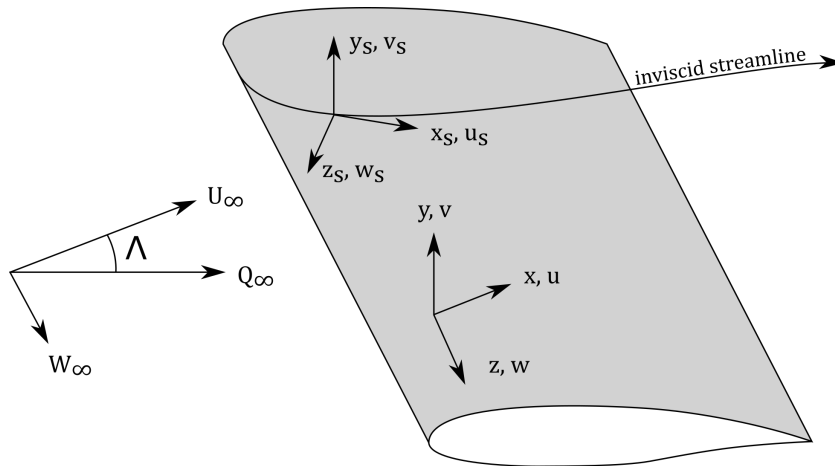


Figure 1.5: Infinite wing reference frames

In mathematical terms, the infinite wing assumption implies that any property of the flow is invariant along the span of the wing, but not necessarily equal to zero, i.e. $\partial/\partial z = 0$. This invariance is also known as the *independence principle*. A consequence of the infinite wing is that the external velocity component W_e becomes a constant, as the flow does not experience any curvature along the span. In addition, the velocity components can be represented in a reference frame aligned with the inviscid streamline at the edge of the boundary layer, as is indicated in figure 1.5. The orientation of this frame is therefore a function of the flowfield and changes along the chord of the wing. This 'streamline' reference frame is labeled with the subscript s . It is of use when the true crossflow velocity components have to be considered separately from the streamwise components.

The simplification of an infinite wing makes it possible to include three-dimensional effects using two-dimensional computations, saving considerable time with only small sacrifices in accuracy. To understand the nature of the three-dimensional boundary layer, the characteristic conditions of such a flowfield are discussed next.

1.4. Boundary layer crossflow

Consider an inviscid streamline over a swept wing successively experiencing a negative and positive pressure gradient as depicted in figure 1.6a (based on [24]). It qualitatively explains the nature of the boundary layer in three-dimensional flow. The profiles are normalized by the local boundary layer thickness to illustrate their differences in shape and the thinning effect of a negative pressure gradient. The velocity components are given in the streamline reference frame, as the bold line at the top is the inviscid streamline (not a straight line in reality). This figure illustrates the changes in crossflow under different external pressure gradients in addition to the direction of the wall shear force. The path of different streamlines in the boundary layer is illustrated in figure 1.6b, so that an intuitive understanding of the flowfield on swept wings can be formed.

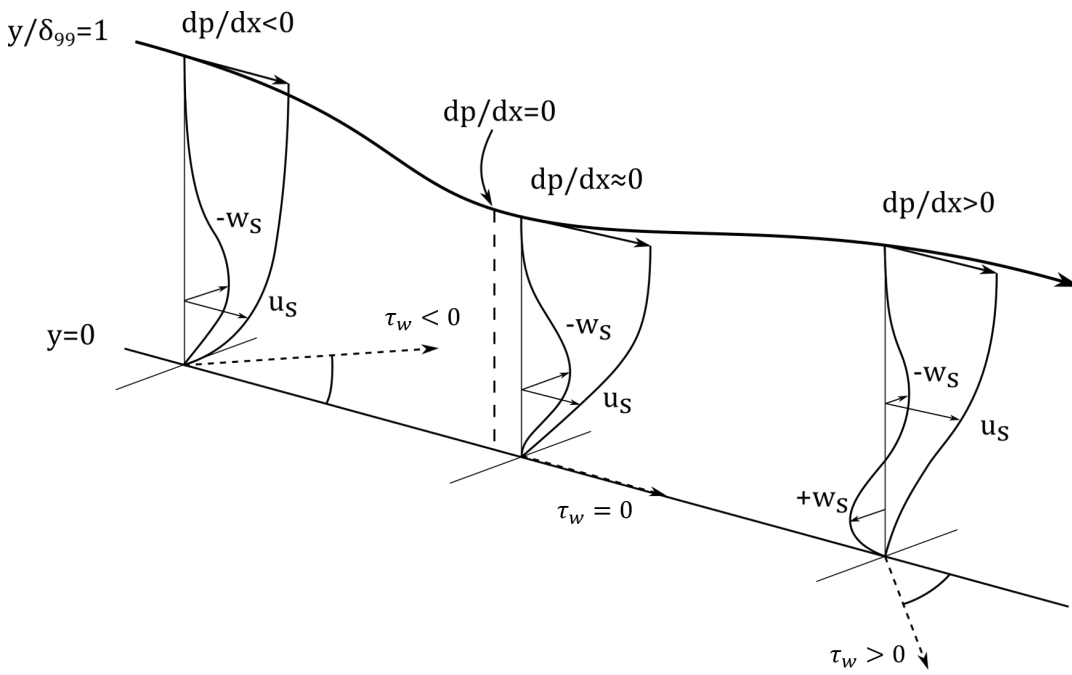
Inviscid streamline First, the location of the inviscid streamline at $y = \delta_{99}$ can be understood from the pressure distribution. Given as the top streamline in figure 1.6b, this streamline originates along the attachment line on the leading edge of the wing, where the U_e component is still zero and the pressure coefficient C_p is equal to one. Therefore, the streamline will be oriented along the span. In this example the W_e component remains constant over the chord, so the streamline direction is only a function of the magnitude of the pressure distribution. It aligns with the freestream at $C_p = 0$ and reaches a maximum angle at the point of minimum pressure. With increasing pressure, the line curves back towards the freestream direction. At the point of separation, the pressure remains constant and the streamline remains straight in accordance with a constant C_p .

Velocity profiles Before considering the streamline on the surface, we have to include the effects of the pressure distribution on the velocity profiles. The direction of the inviscid streamline just described explains the crossflow behavior seen in figure 1.6a. The gradient of pressure is not aligned with this streamline, i.e. in x instead of x_s . What can be concluded from a simple balance of forces is that the pressure gradient induces a force perpendicular to this direction, i.e. along z_s . The negative pressure gradient will cause a negative crossflow *bulge*, as seen in the most left velocity profile of figure 1.6a. The resulting shear stress on the surface is also negative and hence can be said to generally share the sign of the pressure gradient. The exact angle of the shear is *not* aligned with the pressure gradient, as this only defines the velocity profile curvature, see section 2.2. The history of the boundary layer up to this profile determines the actual velocity profiles shape.

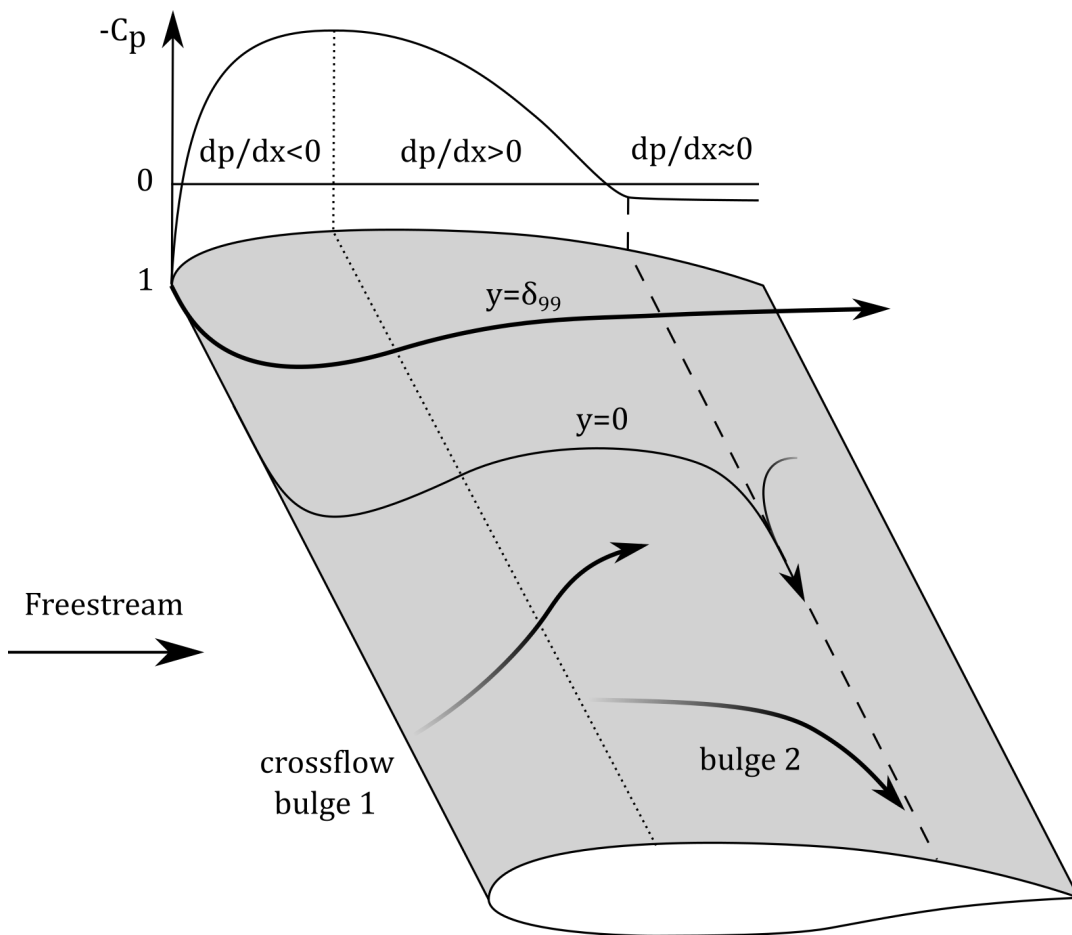
Using the same logic on the second and third velocity profiles, we see two new phenomena. At some point just aft of zero pressure gradient, the existing bulge obtains a gradient equal to zero at the wall, resulting from the inverted pressure gradient. In the positive pressure gradient aft of the pressure minimum we encounter a *second* crossflow bulge. As the bulge is a consequence of the shear stress with the wall, it originates at the wall. The direction of the crossflow is inverted, as is the sign or orientation of the shear stress. The original bulge is still present but will keep decreasing in magnitude. As long as it is still present, the crossflow w_s experiences two inflection points. This is an important observation when considering stability of the boundary layer.

Surface streamline The direction of the surface streamline at $y = 0$ is deduced from the direction of the shear stress components, see the second streamline in figure 1.6b. Like the inviscid streamline, it starts at the attachment line and curves towards the line of minimum pressure, which it roughly crosses in orthogonal direction. It inverts its curvature in the reversed pressure gradient, until it aligns with the line of separation, where by definition the gradient of the u_s velocity profile is zero and shear is solely due to the gradient of the w_s profile. From here, the surface streamline flows down the span of the wing towards the tip. Aft of the line of separation, the backflow in the boundary layer causes the reversed effect, with a surface streamline moving *upstream* towards the line of separation.

Crossflow streamlines Finally, the crossflow bulges depicted in figure 1.6a cause the streamlines in the domain $0 < y < \delta_{99}$ to follow a path that can be predicted qualitatively. The exact path will always be a function of the precise pressure coefficient distribution. The first bulge moves in the negative w_s direction, reaching a maximal velocity at the line of minimum pressure. Just aft of minimum pressure, the streamline has an inflection point and reduces in magnitude until the bulge disappears or fades into the second bulge. This second bulge starts at some point aft of the line of minimum pressure and builds up in magnitude towards the line of separation. There it will become more dominant than the u profile in the vicinity of the wall, as is seen in the right velocity profile in figure 1.6a.



(a) Evolution of the velocity profiles with changing pressure gradient on a swept wing



(b) Characteristic streamlines in the boundary layer of a swept wing

Figure 1.6: Three dimensional flow of boundary layers

1.5. Aircraft design

To design aircraft that use laminar flow, the e^N method has to be placed in a tool that can evaluate the three-dimensional boundary layer and apply linear stability theory to determine the point of transition with minimal user interaction. The application of such a *linear stability tool* would be in the airfoil design of laminar wings, for example. Quantifying the influence of laminar flow on the aircraft as a whole is of interest to determine the potential of this technology.

It is common knowledge that aircraft design is a compromise between different disciplines, such as aerodynamic performance and structural mass. The best compromise can be found if the contribution of each discipline to the aircraft design is thoroughly understood and quantified. Consider the *drag polar* shown in figure 1.7 that illustrates the breakdown of the drag coefficient C_D as a function of lift coefficient C_L . The contribution of skin friction drag (profile drag) to the aerodynamic drag is at times the most dominant part in cruise conditions, between $0.2 < C_L < 0.6$. This leads to a need to determine the sensitivities between laminar flow and aerodynamic performance, even more so the relation between laminar flow and global aircraft parameters such as maximum take-off mass.

Effects on costs are relevant, but these are not included in this discussion because a judgment on costs would require in-depth research into manufacturing methods and operational details of laminar flow aircraft.

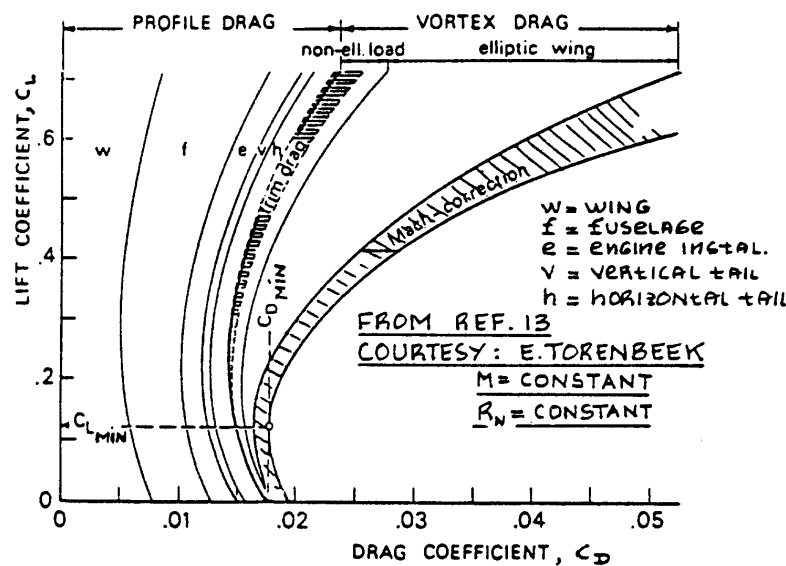


Figure 1.7: Typical drag breakdown of transport aircraft [27]

To enable research on topics such as these, a conceptual and preliminary design program is required. Within the department of Flight Performance and Propulsion of the Aerospace Engineering faculty of Delft University of Technology, a significant amount of effort has been put in the *Initiator*, a sizing tool intended for both conventional and unconventional aircraft configurations such as blended-wing-bodies and Prandtl planes [28]. As such, it is intended to be accurate for aircraft of different shapes and sizes that experience vastly different aerodynamic conditions. The iterative nature of aircraft design is included in the program's framework, allowing quantification of the snowball effect that occurs due to laminar flow design, a highly appreciated utility when considering both redesign and retrofitting of laminar technology.

There is an academic interest into modeling business jets instead of conventional aircraft: An important observation relating to transition is that for a given object, transition occurs further upstream when the Reynolds number is increased [21]. Therefore, extended laminar flow will be achieved with less effort at lower Reynolds numbers. As such, it was decided to investigate the benefits of laminar flow primarily on business jets, which operate at similar freestream conditions as conventional transport aircraft but are smaller in size and hence operate at a lower Reynolds number. It is expected that comparing a regular business jet with the same jet modified for laminar flow design will be more realistic than the same comparison between full-size transport aircraft. However, the *Initiator* does not yet incorporate the design of business jets, so its capabilities have to be extended. Ultimately, the same investigation can easily be repeated for any other aircraft that are included in the program.

1.6. Business jet design

Existing aircraft play an import role during conceptual design. A database of parameters related to existing aircraft is necessary for most methods in this design phase. For example, Class-I design methods are directly based on the trendlines of reference aircraft. These trends usually correlate global aircraft parameters, such as the payload mass (PM), operative empty mass (OEM) and maximum take-off mass (MTOM) [29, 30, 31]. In addition, to reproduce the details of an existing aircraft the Initiator requires input and setting files with top level requirements and other constants as a basis for its design routines. These values are not easily obtainable global parameters such as PM, but include more detailed information. This can vary from the configuration such as the tail type or wing location, up to the minute details such as seat dimensions or spar materials (insofar these data can be found in open literature). A business jet database was constructed to provide reference data for both the global trendlines and the detailed parameters [32]. The complete list of aircraft included in the database can be found in appendix A. Some of the characteristics differences between business jets and conventional aircraft can be shown by comparing the database to the existing Initiator database of conventional jet aircraft.

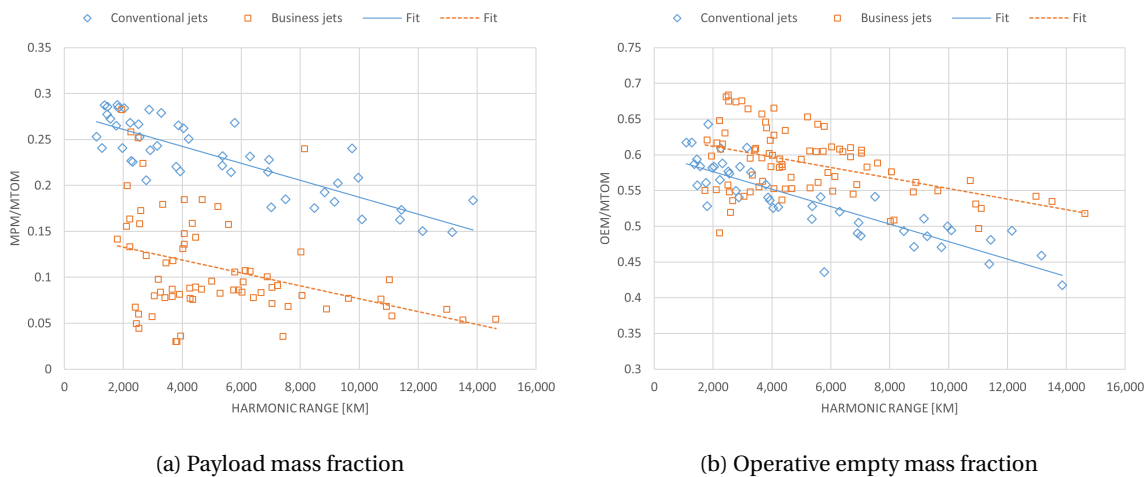


Figure 1.8: MTOM fractions comparisons between conventional and business jets

Business jets do not necessarily use the standard seating layout found on passenger aircraft. Although a conventional row layout is certainly a possibility, business jets usually contain cabins with a low passenger density. As such, the payload (consisting of people and their luggage) that is carried by the business jet is relatively low compared to its size. This is illustrated in figure 1.8a in which the fraction of the maximum PM with respect to the MTOM is laid out against the range for maximum PM (harmonic) mission of each aircraft. There is a clear distinction between the conventional aircraft and business jets, with the exception of a few conventional jets that are retrofitted with business cabins and listed as business jets. For both types of aircraft, short harmonic ranges seem to relate to higher payload fractions. This is especially true for the business jets with a harmonic range below 6,000 km. Note that a longer range does not necessarily relate to a larger aircraft.

For the OEM fractions in figure 1.8b the databases show a similar trend, with slightly lower values for conventional than for business jets. A small decrease with respect to range is seen, because fuel becomes a larger fraction of the total aircraft mass over longer distances. As there is no large difference in the operative empty mass fraction between both types of jets, the corollary effect of a lowered payload fraction is the increase of the fuel fraction for these harmonic missions. Hence, the location of fuel will predominately drive the center of gravity (CG) location and its shift during cruise, opposed to passengers and cargo. This is in addition to the fuselage tanks within the wing-body fairing of most long range business jets or the aft-of-cabin tanks in older jets, see figure 1.9. These inherently have a larger distance to the CG and thereby increase the shift of CG during cruise. The limits of the CG location are fundamental for landing gear sizing methods and longitudinal or lateral stability calculations. Positioning of the wing and its fuel tanks in addition to any tanks in the fuselage or empennage can therefore be predicted to be of higher influence for business jets.

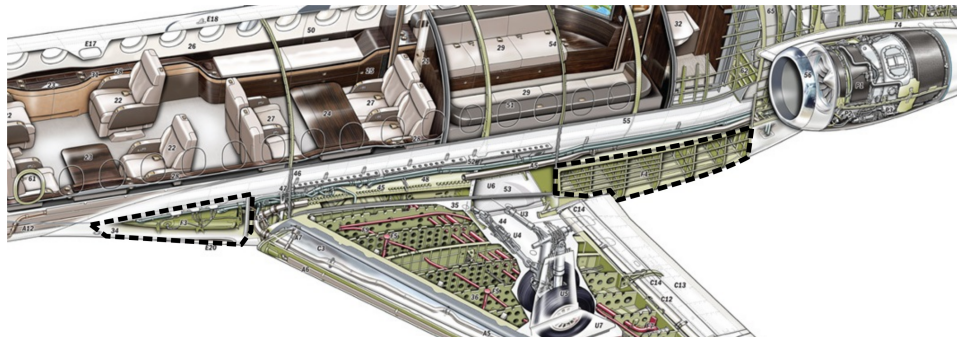


Figure 1.9: Cutaway of Dassault Falcon 8X showing fuel tanks in the wing-body fairing [33]

1.7. Research plan

A broad range of topics have been discussed in the preceding sections, ranging from fundamental aerodynamic analyses up to aircraft design methods. As such, there are many important topics worth investigating within this thesis project. The general impression from literature is that non-existence of laminar aircraft is a combination of practical problems and the inherent complexity of laminar flow. The latter illustrates a separation of disciplines that could be bridged using simple analysis methods and the benefits of modern computational power. Making this leap will be the focus of this thesis project.

The observations made from literature can be summarized in a research plan that specifies the content of the thesis. The plan will be formulated with several research questions. The main research question of the thesis will be:

What are the effects of laminar flow technology on swept wing business jet design?

This main question can be subdivided into several topics with their own research questions:

1. With respect to aircraft design, the Initiator will have to be updated for business jet design. Therefore, the following questions may be asked to compare between conventional aircraft and business jets: What differences underscore the distinction? What are the differences in design process? To what extent can empirical methods be extrapolated to business jets?
2. Specific to the topic of laminar flow technology on aircraft design, the next items are relevant: How is the effect of laminar flow technology included in aircraft design? How can you compute the extend of laminar flow? How large is the effect of extended laminar flow on the total drag reduction of an aircraft? How are airfoils designed to operate in laminar conditions?
3. Finally, focusing on the linear stability tool: How is linear stability theory applied to boundary layers? How can the point of boundary layer transition be determined using this theory? What contributions are needed to automate calculations using linear stability theory? How are the results of the stability calculations best implemented into aircraft design?

1.8. Thesis structure

Drawing from the research questions, a plan to complete the thesis can be formulated. In reverse order, the first item to be resolved is the linear stability tool. A tool will be build to automatically find the transition location on an airfoil by computing an external pressure gradient, producing a laminar boundary layer solution and calculating its stability. For the external pressure gradient, a simple method such as Xfoil will be used. Already existing Matlab tools are available for the laminar boundary layer solution and the stability calculations. The tool itself will consist of a framework to link these three components.

Then, to produce a reference aircraft on which laminar flow can be applied, the Initiator will be utilized. Its methods can be extended to include business jets as to create a consistent reference aircraft. Afterwards, this program will make it possible to obtain the quantitative differences to a laminar aircraft. The direct differences in performance, plus the post-convergence result can illustrate both the immediate benefits and the snowballing effect, respectively.

To connect the high-fidelity stability calculations with aircraft design, the point of transition can best be used as a scaling variable. The point of transition is used to determine the extend of laminar versus turbulent flow on a wing or tail surface. A direct aerodynamic analysis on the local geometry will costs too much time for an iterative conceptual design program such as Initiator. Therefore, a surrogate trendline in transition location from the detailed analysis has to be used to calculate the skin friction components fore and aft of transition. The structure of the research plan is illustrated using the diagram given in figure 1.10.

The method of the linear stability tool will be discussed in chapter 2, followed by an in-depth review of the implementation with a case-study as example in chapter 3. The modifications of the Initiator tool and the laminar flow aircraft designs are discussed in chapter 4. Finally, the conclusions on this work and further recommendations are found in chapter 5.

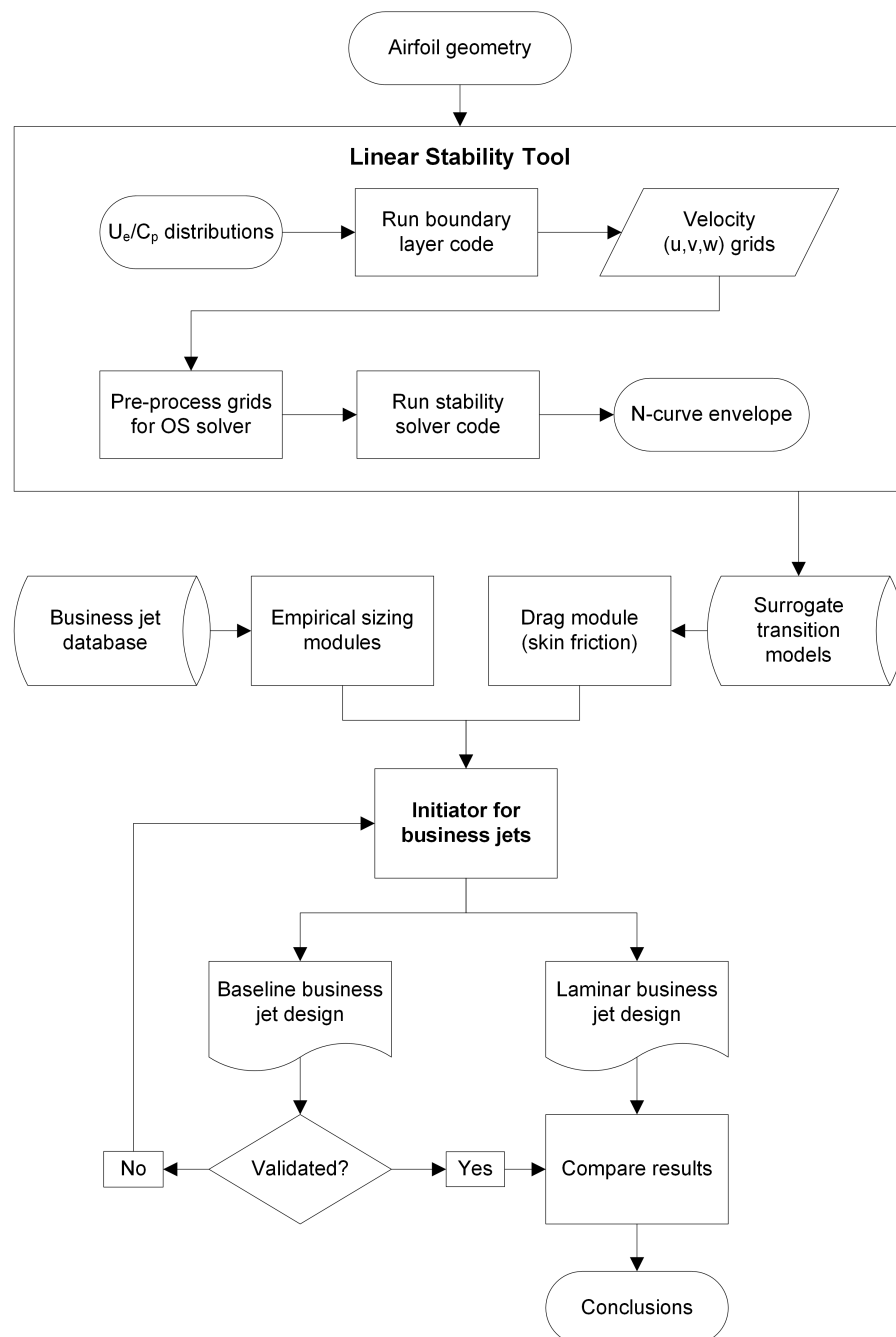


Figure 1.10: Technical structure of the thesis

2

Linear stability tool

Transition prediction using linear stability theory is a well-known topic with a broad basis in literature. On the contrary, a tool to automate the application of this theory for any given airfoil is not discussed in open literature, see the discussion in the Introduction. This chapter will explain the framework which surrounds the Orr-Sommerfeld solver and show the methods used to automate the process. A brief overview of the tool is given to explain the implementation.

2.1. Overview

The tool contains three processes that require explanation, illustrated by a flowchart seen in figure 2.1, which is an excerpt from the thesis layout diagram in figure 1.10. These are the boundary layer code, which calculates a laminar boundary layer from the leading edge point up to separation, and the stability code, which creates the N-factor envelope from the boundary layer solution. Before the stability code is used, the boundary layer is analyzed and converted to a useful format. This is done as a preparation and yields several important parameters which are necessary for the stability code to run without logical problems. The input to the tool is an edge velocity (or pressure) distribution, with the output being the N-curve envelope.

The actual linear stability computations are performed sequentially with a coarse and a fine grid. The grid discretizes the problem so that the Orr-Sommerfeld equation is solved for a unique set of the parameters (Re, ω, β) , where each parameter set corresponds to an amplification ratio α_i . The pre-process phase is necessary to decide on the bounds for these parameters, as not all combinations can be solved or are needed. The coarse grid over the entire (feasible) variable domain is evaluated to identify the trends of the solution of the case at hand. Then, the important regions can be identified and are evaluated with a fine grid. The completed set of solutions forms a grid that can be interpolated at any point as is needed to integrate an N-curve for a specific frequency or wavelength.

Integration is performed on the amplification ratios α_i for one physical frequency or wavelength according to the semi-definite integral in equation 2.1 [34]. The domain starts at the point of neutral stability, i.e. $\alpha_i = 0$ at x_0 for that frequency. The upper limit is the domain ordinate x such that the N-factor is a function of x and produces an N-factor curve. The entire set of N-curves, each relating to a single frequency, is then compared to determine the maximum N-factor of all curves per x position. This will produce an envelope of the N-factors that can be used to determine transition by intersection with a predefined critical N-factor, an example of which was given in figure 1.2.

$$N(x) = - \int_{x_0}^x \alpha_i dx \quad (2.1)$$

The process is separated into evaluation of the $\beta = 0$ and $\omega = 0$ domains, solving for either the Tollmien-Schlichting or cross-flow transition cases in sequence. The framework iterates over both types of instability and the sides of an airfoil to determine the upper and lower surface transition points. This finalizes the output of the tool, by providing N-curves of both types of stability on both surfaces that can be intersected with a critical N-factor. The algorithm makes use of several scripts and functions that require detailed explanation. The following sections will discuss these subroutines in further detail.

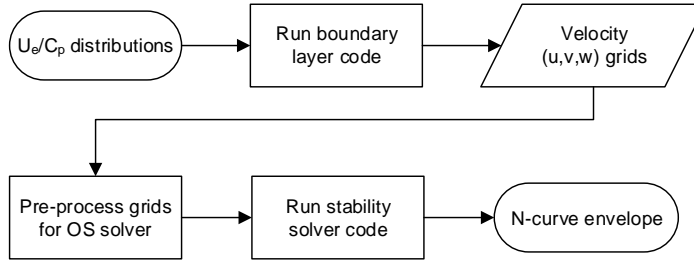


Figure 2.1: Linear stability tool flowchart

2.2. Boundary layer code

The input to the linear stability tool is an inviscid solution that specifies the external velocity, or pressure, of the boundary layer. The boundary layer is then computed using a finite difference scheme described in several textbooks, such as Schlichting-Gersten [35]. The implementation of the formulation in Schlichting-Gersten is discussed below, as well as some numerical problems when resolving the boundary layer in the vicinity of the stagnation point of an airfoil, i.e. high external (or inviscid) pressure gradients.

2.2.1. Boundary layer solver

The boundary layer equations which have to be solved are the momentum and continuity equations for two-dimensional, steady, incompressible flow. These are given by equations 2.2 and 2.3, respectively, which can be found after simplifying the Navier-Stokes equation using the aforementioned assumptions. This process can be found in any introductory textbook to aerodynamics, such as Anderson [5].

$$u \frac{\partial u}{\partial x} + v \frac{\partial u}{\partial y} = U_e \frac{dU_e}{dx} + \nu \frac{\partial^2 u}{\partial y^2} \quad (2.2)$$

$$\frac{\partial u}{\partial x} + \frac{\partial v}{\partial y} = 0 \quad (2.3)$$

The equations are solved over a predefined orthogonal grid, detailed in figure 2.2. The parameters which define the domain are height H , starting station S and length L , all in meters. The grid is discretized using n_x nodes along the surface and n_y nodes perpendicular to the surface. The subscripts i and j are used to indicate a specific station in x or y , respectively. Increments Δx and Δy are defined by:

$$\Delta x = \frac{L - S}{n_x - 1} \quad \Delta y = \frac{H}{n_y - 1} \quad (2.4)$$

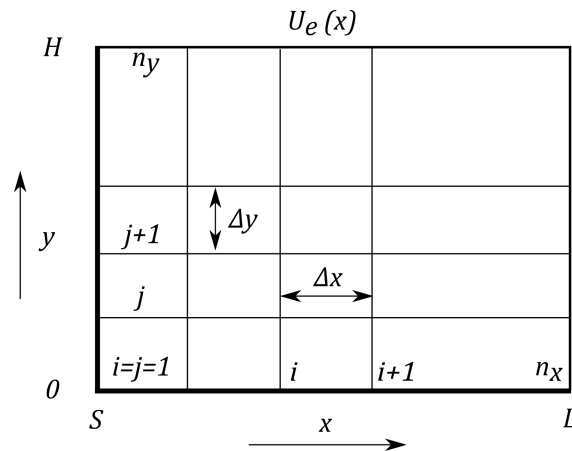


Figure 2.2: Boundary layer solver grid

To numerically solve the boundary layer equations, the partial derivatives are replaced by difference quotients, which are formulated differently, but equivalently, depending on the author. White and Schlichting-Gersten agree on the use of a marching method to resolve the boundary layer per station in the direction of the flow [21, 35]. The solution per station is obtained by integrating one of the difference formulations, assuming a flat plate with an external velocity distribution $U_e(x)$, also indicated in figure 2.2.

An inflow velocity profile is required to start the marching procedure. This problem can be resolved by assuming a Falkner-Skan velocity profile proportional to the pressure gradient of the first station. A detailed discussion of the Falkner-Skan solutions can be found in section 2.6. The wall conditions for u and v are assumed to be zero (no-slip), while an inviscid freestream solution is required for the edge condition: $u = U_e$ or $w = W_e$. In case of boundary layer suction or blowing, the wall condition for v can be adjusted to a non-zero value: positive for blowing and negative for suction.

2.2.2. Crank-Nicolson

The *Crank-Nicolson scheme* is an implicit, central space differencing method that uses the quotients in equations 2.5 [35]. It is implicit as the quotients use nodes that are known, upstream ($j - 1$) and unknown, downstream ($j + 1$). It is central space as the quotients along y are the average of the quotients at i and $i + 1$, hence the subscript $i + 1/2$.

$$\begin{aligned} \left(\frac{\partial u}{\partial x}\right)_{i,j} &= \frac{u_{i,j+1} - u_{i,j}}{\Delta x} \\ \left(\frac{\partial u}{\partial y}\right)_{i+1/2,j} &= \frac{u_{i+1,j+1} - u_{i+1,j-1} + u_{i,j+1} - u_{i,j-1}}{4\Delta y} \\ \left(\frac{\partial^2 u}{\partial y^2}\right)_{i+1/2,j} &= \frac{u_{i+1,j+1} - 2u_{i+1,j} + u_{i+1,j-1} + u_{i,j+1} - 2u_{i,j} + u_{i,j-1}}{2(\Delta y)^2} \end{aligned} \quad (2.5)$$

Substituting equations 2.5 into the momentum equation 2.2 results into the Crank-Nicolson scheme given in equation 2.6. Note, the coefficients in Schlichting omit the v and use as the forcing term $-dP/dx$ instead of $+U_e dU_e/dx$ [35].

$$A_{i+1/2,j}u_{i+1,j+1} + B_{i+1/2,j}u_{i+1,j} + C_{i+1/2,j}u_{i+1,j-1} = D_{i+1/2,j} \quad 2 \leq j \leq n_y \quad (2.6)$$

with coefficients:

$$\begin{aligned} A_{i+1/2,j} &= \frac{v/\Delta y - v_{i,j}/2}{2\Delta y} & B_{i+1/2,j} &= -\left[v/(\Delta y)^2 + u_{i,j}/\Delta x\right] \\ C_{i+1/2,j} &= \frac{v/\Delta y + v_{i,j}/2}{2\Delta y} & \bar{B}_{i+1/2,j} &= -\left[v/(\Delta y)^2 - u_{i,j}/\Delta x\right] \\ D_{i+1/2,j} &= A_{i+1/2,j}u_{i,j+1} + \bar{B}_{i+1/2,j}u_{i,j} + C_{i+1/2,j}u_{i,j-1} + \left(U_e \frac{dU_e}{dx}\right)_{i+1/2} \end{aligned} \quad (2.7)$$

Although the explicit formulation would be algebraically simpler and computationally faster for the same grid, it suffers from numerical instabilities and a higher error at similar discretization [21]. The explicit formulation error can be resolved by iterating the profiles at each station, but this would at least double the computational time. Iterating the implicit formulation provides negligible gain in accuracy and hence is not required. Also, the implicit formulation is unconditionally stable. The benefits of not having to check the stability criteria and also having a higher precision per computation (important for the stability calculations, which use the second derivatives of the profiles) makes the implicit formulation more attractive.

Equation 2.6 shows that the implicit formulation results in a *tridiagonal* problem. The format of this problem is given in equation 2.8. The coefficients of equation 2.6 given in equation 2.7 are inserted along the three diagonals of the coefficient matrix. The Crank-Nicolson scheme is used to solve the u and w component of the flow, but for w the coefficient D for w has no pressure term (see next section). The v component perpendicular to the wall follows directly from the continuity equation 2.3.

$$\begin{bmatrix} b_1 & c_1 & & & 0 \\ a_2 & b_2 & c_2 & & \\ & a_3 & b_3 & \ddots & \\ & & \ddots & \ddots & c_{n-1} \\ 0 & & & a_n & b_n \end{bmatrix} \begin{bmatrix} u_1 \\ u_2 \\ u_3 \\ \vdots \\ u_n \end{bmatrix} = \begin{bmatrix} d_1 \\ d_2 \\ d_3 \\ \vdots \\ d_n \end{bmatrix} \quad \text{with } a_1 = 0 \text{ and } c_n = 0 \quad (2.8)$$

The tridiagonal matrix algorithm (TDMA) or *Thomas algorithm* is used to solve the tridiagonal system. This procedure is used instead of matrix inversion because the Crank-Nicolson scheme only has three unknowns per node along y . As can be observed from equation 2.8, two coefficients do not fit inside the matrix: A_1 and C_{ny} . These relate to the two boundary conditions of the wall (no-slip condition) and the boundary layer edge (freestream) and are simply zero. That is, there are only two unknowns at the top and bottom grid-points of the system. Forward substitution of the wall condition removes an unknown from all grid-points, while backward substitution of the edge condition eliminates the second unknown, resulting in a solved system [21]. This is equivalent to Gaussian elimination.

2.2.3. Infinite wing assumption

For swept wings, the infinite wing assumption as described in the Introduction (see chapter 1) is used. Substituting $\partial/\partial z = 0$ instead of $W \equiv 0$ into the boundary layer equations results in a third equation for the momentum in span-wise flow; see equation 2.9. Note, this equation is identical to 2.2, but has u substituted for w in its derivatives and does not include an external pressure gradient term. The boundary conditions for this equation at a given station are similar to u , although the edge velocity W is no longer a function of x .

$$u \frac{\partial w}{\partial x} + v \frac{\partial w}{\partial y} = \nu \frac{\partial^2 w}{\partial y^2} \quad (2.9)$$

The continuity equation for u and v is decoupled from w in the infinite wing problem. This makes it possible to solve the chord-wise two-dimensional components independently from the span-wise component. Converting equation 2.9 to the implicit formulation, results in the same coefficient matrix for equation 2.2. This implicit scheme requires no further iteration as equation 2.9 is linear. The right-hand side of the system D has changed, because the forcing term due to the pressure gradient is no longer present, see equation 2.10. As a result, the boundary layer code can produce the velocity profiles for all three velocity components without any iterative procedure.

$$D_{i+1/2,j}^w = A_{i+1/2,j} u_{i,j+1} + \bar{B}_{i+1/2,j} u_{i,j} + C_{i+1/2,j} u_{i,j-1} \quad (2.10)$$

2.2.4. Leading edge singularity

In the vicinity of the stagnation point of most airfoils, the pressure experiences a high gradient (i.e. the external velocity U_e has a high gradient). In extreme cases, it was observed to lead to large errors in boundary layer solver that were originally attributed to the singularity of the leading edge for the flat plate analogy being applied in the solver. At the leading edge, the assumptions that the boundary layer is thin (used to derive the boundary layer equations) is no longer valid. As the velocity profiles in the vicinity of the leading edge are of high importance for CF stability calculations, this error had to be minimized.

The numerical error in the *curvature* of the velocity profiles at the wall was observed to be alternating in sign with equal absolute magnitude from the theoretically expected value. In the absence of a pressure gradient, this error disappeared. An iterative averaging method was devised to match the wall curvature from the boundary layer solution with the curvature predicted by the external pressure gradient by equation 2.11. This relation is obtained from equation 2.2 by substituting the wall conditions $u = 0$ and $v = 0$, which removes the left-hand side.

$$U_e \frac{dU_e}{dx} = -\nu \frac{\partial^2 u}{\partial y^2} \quad (2.11)$$

Averaging is performed on the inlet solution for a predetermined number of iterations. The effectiveness of the averaging method can be observed in the curvature at the wall as calculated by the solver, i.e. the right-hand-side of equation 2.11 evaluated at $y = 0$. For a boundary layer solution of a continuous Falkner-Skan edge velocity distribution corresponding to $\beta = 0.8$, the two terms on the right-hand-side and their relative

error can be computed, see figure 2.3. In figure 2.3a the averaging method is not used, producing large errors in the vicinity of the leading edge. When implementing the averaging, the error reduces at least two orders in magnitude as is seen in figure 2.3b.

A secondary transient (or an oscillation) of the normalized error can be observed in both schemes at $Re_l = 90$ and 77 respectively. The origin of this transient could not be determined, but considering the low order of magnitude it is assumed to cause no further errors in the stability solvers.

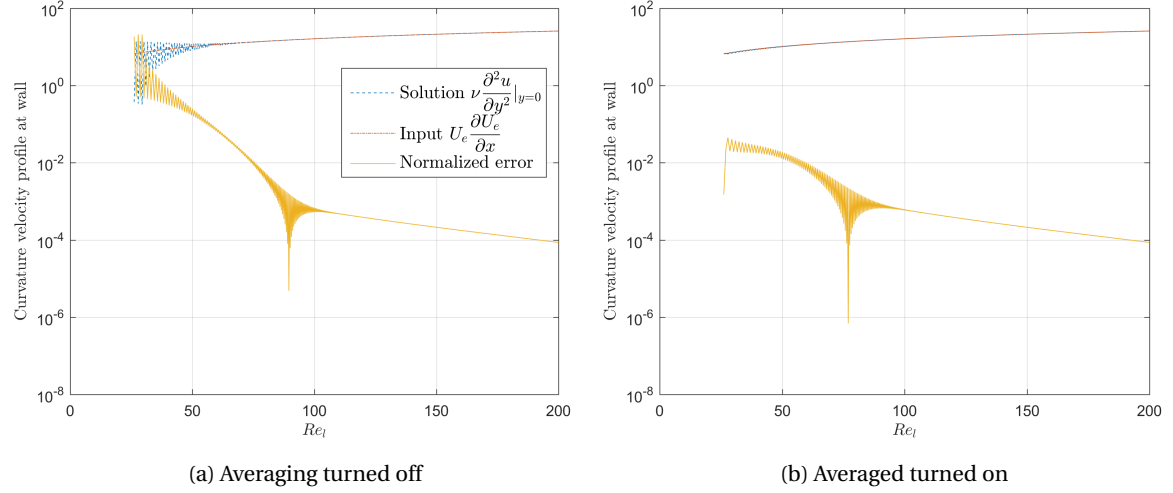


Figure 2.3: Effect of inflow averaging on the velocity profile curvature at the wall.

Notwithstanding the improvements obtained by averaging the solution, there is likely to be a fundamental error within the current implementation of the boundary layer solver. The primary candidate for this error would be the exact formulation of the implicit Crank-Nicolson scheme. More specifically, as the numeral error was seen to be proportional to pressure gradients, the calculation of the forcing term in the D coefficient of equations 2.7 is to be reconsidered. A last resort would be to iterate each station (similar to any explicit scheme) until the error is reduced below a certain margin. Further investigation into this problem is left for future work.

2.3. Orr-Sommerfeld

The core of the laminar flow tool relies on solving the Orr-Sommerfeld (OS) equation. As this part of the tool has been created outside of the scope of this thesis, this discussion will mostly be on the implementation and limitations. The dimensionless OS equation is given by equation 2.13. It is obtained by substituting the equation for a linear disturbance ϕ 2.12 into the three-dimensional linearized Navier-Stokes equations and subtracting the mean-flow from the solution (an example of such a derivation can be found in White [21]). The boundary conditions for the OS equation are given in equation 2.14. The boundary conditions follow from the no-slip condition at the wall and the end condition at the freestream, where the disturbance should be zero. The primes in equation 2.13 indicate the derivatives with respect to the variable y in equation 2.12.

The disturbance can physically be interpreted as a fluctuation of the mean flow velocity. Equation 2.12 illustrates the local nature of a *disturbance wave* (the amplitude $\hat{\phi}$ is a function of y only) and the complex coefficients α , β and ω indicate the frequency (real part) and growth (imaginary part) of such a wave in the x , z and t directions, respectively.

$$\phi(x, y, z, t) = \hat{\phi}(y) e^{i(\alpha x + \beta z - \omega t)} \quad (2.12)$$

$$(U_e - c)(\phi'' - (\alpha^2 + \beta^2)\phi) - u''\phi = \frac{-i}{\sqrt{\alpha^2 + \beta^2} Re} (\phi'''' - 2(\alpha^2 + \beta^2)\phi'' + (\alpha^2 + \beta^2)^2\phi) \quad (2.13)$$

$$\begin{aligned} \phi(0) &= \phi'(0) = 0 \\ \phi(\infty) &= \phi'(\infty) = 0 \end{aligned} \quad (2.14)$$

An important realization is that the OS equation contains the velocity profile and its second derivative. As such, the velocity profile curvature at the wall (easily obtainable from the external pressure gradient) is a good measure of the magnitude of the instability solution, see equation 2.11. This observation will be referred to at several points within this report.

The OS equation and boundary conditions are linear and homogeneous, resulting in an eigenvalue problem. Given the complex parameters α , β and ω , a value for ν (or Reynolds number Re), in combination with a velocity profile, an additional assumption is necessary to resolve the system. By assuming that either $\alpha_i = 0$ or that $\omega_i = 0$, a closed eigenvalue problem is obtained by assuming linear growth in time or in space, separating it in either a temporal or spatial problem, respectively. In the tool used for this thesis, the spatial formulation was used, i.e. $\omega_i = 0$. As such, the growth rate in space α_i is the result of the calculation. A solution is found by applying a spectral collocation mapping of a truncated number of Chebyshev polynomials on the eigenfunction mesh and solving the resulting eigenvalue problem. The mapping and the eigenvalue problem are further explained below. The OS equation is solved for TS waves and CF vortices in turn, by inserting $\beta = 0$ and $\omega = 0$, respectively. Oblique TS waves in compressible flow and traveling CF vortices are resolved by inserting combinations of non-zero β and ω , adding an additional dimension and increasing the size of the problem significantly. As the methods in this work are incompressible and traveling waves are a consequence of high receptivity, this parameter space will not be considered.

An important side-note, the computational time required to solve the eigenvalue calculation is the largest component of the stability tool, approximately 90-95% of the stability code duration. The speed has been increased by utilizing parallel processing of multiple combinations of Reynolds number and frequency. Further improvement can be gained by solving the temporal problem for ω instead of the spatial problem for α , which reduces the size of system by a factor 4 and consequently its computational time by a factor of 16, see equation 2.15 [36].

$$\begin{aligned} t_{spatial} &= (4 \cdot NC)^2 \\ t_{temporal} &= NC^2 \end{aligned} \quad (2.15)$$

However, to obtain the spatial amplification the solution has to be transformed using the Gaster transformation [37], given in equation 2.16. This new value for α_i can be inconsistent with the value selected to solve the temporal problem. Hence, several iterations are required to obtain a consistent result with adequate precision. The iterative temporal scheme will still be faster than the spatial scheme if the number of iterations is less than 16, when considering the size of the system. This scheme was outside the scope of this thesis and is left as a recommendation for future work.

$$\alpha_i = - \left(\frac{\partial \omega_r}{\partial \alpha} \right)^{-1} + O(\omega_i^2) \quad (2.16)$$

2.3.1. Spectrum

The OS solver solves the Orr-Sommerfeld equation using an eigenvalue analysis. The outputs from the boundary layer solver are normalized using scaling factors, most important being the Blasius length given in equation 2.17. As can be seen, the Reynolds number using the Blasius length Re_l is identical to the square root of the linearly spaced Reynolds number Re_x . The variable Re_l is used throughout the stability solver part of the tool as the ordinate, to increase leading edge resolution and simplify the N-curve integration, explained in chapter 3. The normalizations of the Orr-Sommerfeld parameters are given in equation 2.18.

$$l = \sqrt{\frac{x\nu}{U}} \rightarrow Re_l = \frac{lU}{\nu} = \sqrt{\frac{xU}{\nu}} = \sqrt{Re_x} \quad (2.17)$$

$$\bar{\omega} = \omega \frac{l}{U}, \quad \bar{\beta} = \beta l, \quad \bar{u} = \frac{u}{U_e}, \quad \bar{w} = \frac{w}{U_e}, \quad \eta = \frac{y}{l} \quad (2.18)$$

The solver produces a set of eigenvalues and eigenfunctions of equal dimension as the eigenfunction discretization using Chebyshev polynomials. The eigenvalue spectrum can be plotted in the complex plane, as is shown in figure 2.4. This spectrum represents a characteristic cross-flow velocity profile evaluated at Re_l 1500, $\beta l = 0$ and $\omega l/U = 0.05$. The velocity profile used is given in figure 2.5, in which subfigure (a) shows the components in a leading-edge perpendicular reference frame and subfigure (b) has the components rotated to align with the local inviscid streamline, which illustrates the true cross-flow bulge.

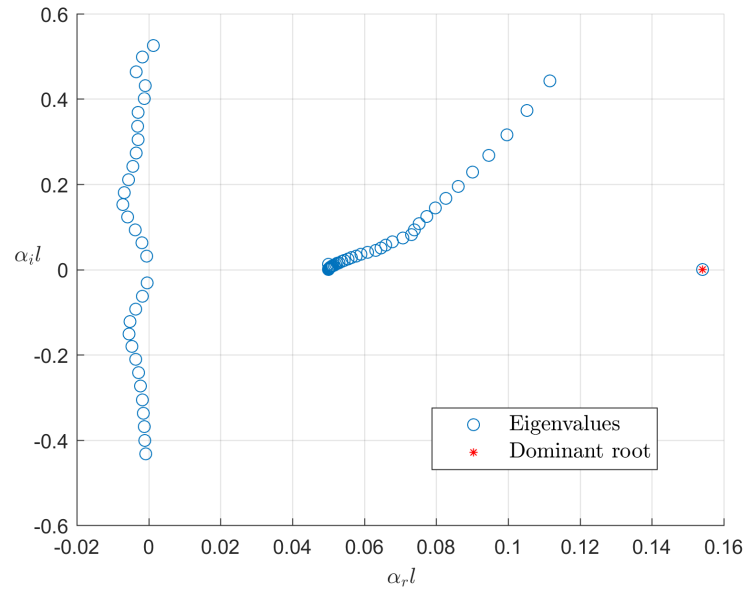


Figure 2.4: Eigenvalue spectrum of the Orr-Sommerfeld equation

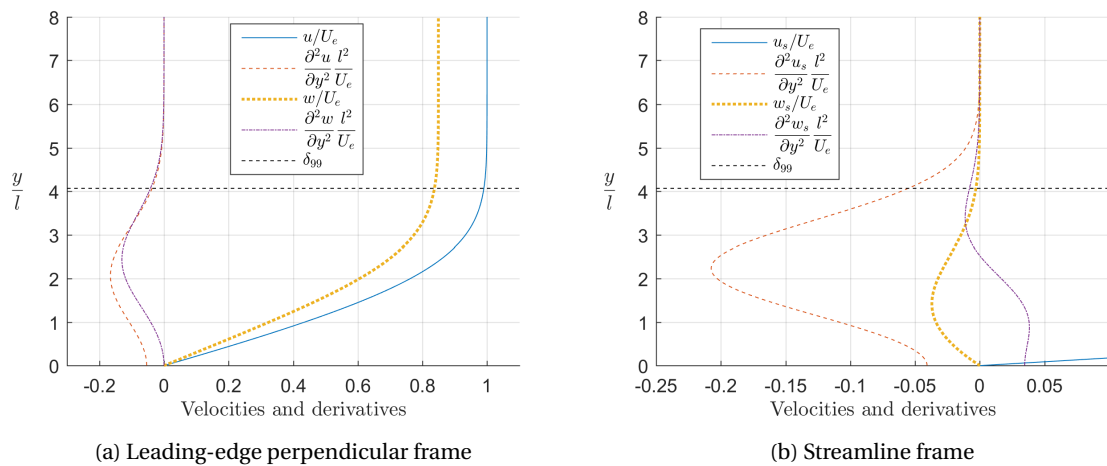


Figure 2.5: Characteristic cross-flow velocity profile

While the dominant root in figure 2.4 can be identified from the other eigenvalues by visual inspection, such an offset is not always present. For most velocity profiles, only one eigenvalue represents the most amplified disturbance. The additional strings, or *branches*, of eigenvalues within the spectrum represent other kinds of solutions. This will be discussed in section 2.4, alongside the method to identify the correct eigenvalue with automated methods.

2.3.2. Mapping of collocation points

The spectral method of using Chebyshev polynomials to discretize the problem is originally described by Malik [38] and implemented by Groot [39] and will therefore only briefly be introduced. The computational space is discretized using Chebyshev polynomials by mapping the polynomials defined on the domain $[1, -1]$ onto the eigenfunction space $[0, y_{max}]$. The eigenfunction is then discretized using a prescribed number of Chebyshev polynomials. The collocation points of the Chebyshev polynomials are placed using a scaled cosine distribution, as to increase resolution in the curved parts of the profile at the wall and decrease resolution in the relatively constant non-shear layer of the boundary layer, see figure 2.6. The vertical axis, $\sin(\theta)$, is used to for illustration purposes only. Using this distribution, half the nodes of the mapping are in the do-

main $[0, y_i]$ and half in $[y_i, y_{max}]$, easily obtained using equation 2.19. As such, in addition to the number of polynomials NC , two parameters are used to define this distribution: the mid-point y_i and maximum point y_{max} . The value of these parameters depend on the type of the disturbance inserted in the OS solver.

$$\eta = \frac{y_{max} y_i (1 + \cos(\theta))}{y_{max} - \cos(\theta) (y_{max} - 2y_i)} \quad \text{with } 0 \leq \theta \leq \pi \quad (2.19)$$

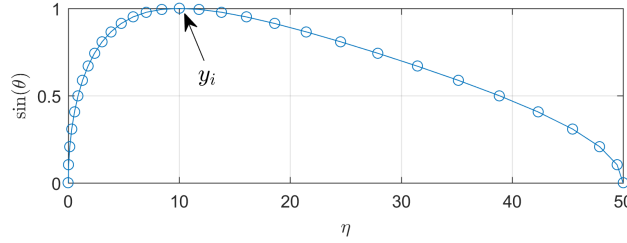


Figure 2.6: Mapping example using $y_{max} = 50$ and $y_i = 10$

The y_{max} variable is located where the top boundary conditions of the solution are applied. Practically, this will be valid as long as the maximum point is distanced sufficiently far from the disturbance itself. The midpoint has to be selected as a compromise between two requirements: It is necessary to accurately resolve the highly non-linear velocity profile of the disturbance that is found in the vicinity of the wall. Meanwhile, the asymptotic trend of the disturbance with increasing y can not be ignored completely.

To obtain a set for all three mapping parameters, a heuristic approach is applied to the drift of the eigenvalue solution. The solution is varied by changing the mapping parameters for a range of Reynolds number and frequency on a given velocity profile. The drift is the absolute distance of the eigenvalue in the complex plane, measured from the preceding calculation with a slightly different parameter set. The profiles given in figure 2.5 are used, as such profiles are common within swept wing boundary layers. The profile includes a strong cross-flow component and the eigenvalue is easily distinguished from the rest of the spectrum. This distinct nature is helpful to analyze a wide range of the mapping parameters.

The methodology of the investigation is to modify one out of three parameters until the drift of the eigenvalue in the complex plane reaches a constant plateau or asymptote. Such a plateau occurs after the order of magnitude of the numerical error becomes larger (smaller) than the increased (decreased) accuracy from the parameter set. Such a trend can be seen in figure 2.7, in which the number of Chebyshev polynomials is increased incrementally. For this first case, the cosine distribution is symmetrical (mid-point is halfway the domain) and the maximum is placed within the boundary layer solution, at $y/l = 22.6$. As can be observed, the drift reaches a plateau for both components after increasing the number of polynomials to approximately 55. This value is therefore selected as a preliminary heuristic.

Definitive values for all three parameters are found by repeating this scheme for the mid-point, maximum point and number of polynomials until their values no longer vary. An example of such a procedure for multiple Reynolds numbers at a single frequency can be found in appendix D. These heuristics are assumed to be independent of the physical parameters of the problem, e.g. ω , Re , etc. This is based on the fact that the perturbation shape varies only to a minor extend for other parameter values. During the creation of the linear stability tool, this procedure was repeated for additional types of velocity profiles as well, indicating the aforementioned invariance when scaling the domain.

It was found that the maximum point of the mapping has to be placed at increased height, beyond the boundary layer thickness that is normally captured from the boundary layer solver. For cross-flow, this comes down to roughly $y_{max} = 50$ while TS waves require even higher values at $y_{max} = 100$. This difference is expected from the slow decaying nature of Tollmien-Schlichting waves in both wall normal and parallel directions, compared to the local nature of the crossflow vortices. The mid-point had to be placed in the vicinity of maximum curvature of the velocity profile, for both types of instability. Therefore, this point is not necessarily at constant y/l but is placed per profile by calculating the location of highest profile curvature intensity (curvature of u for TS, of w_s for CF) so to take into account variations therein. The streamline oriented velocity profiles, denoted with subscript s , are used for the crossflow curvature, because they better relate to the physical disturbance. Finally, the number of polynomials was found to be highly proportional to the solution of the OS solver itself: amplified modes require just a few polynomials (at least 30/60 for TS/CF) to be numerically accurate, while highly damped modes need many. Moreover, the OS solver might fail to identify

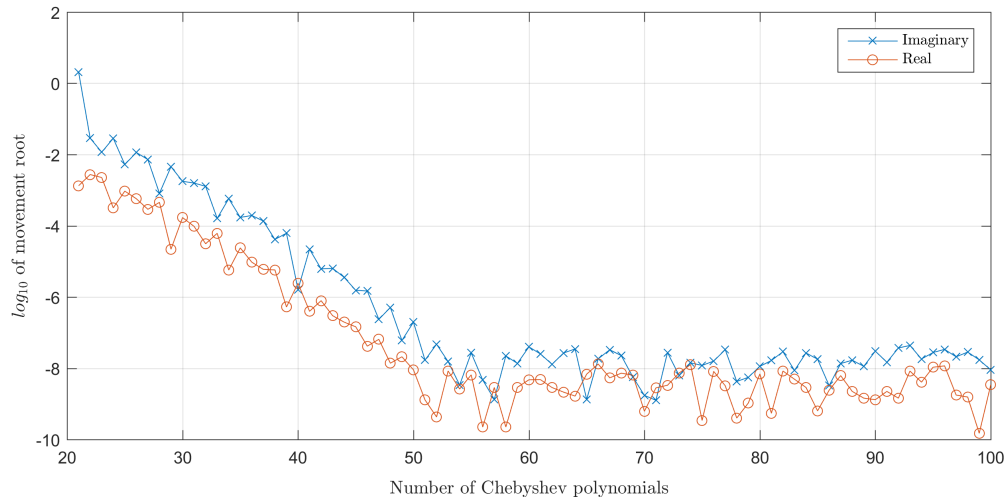


Figure 2.7: Drift of eigenvalue with increasing number of polynomials

an unstable mode (even with extremely detailed discretization using 200 or more polynomials) if the mode is too highly damped. This final point proved to be a significant hurdle during the creation of the linear stability tool, which will be discussed in further detail in section 2.5. The inability to capture stable modes is too complex to consider within the framework of this thesis and will be considered an inevitable occurrence.

The result from the mapping investigation is both robust and highly efficient. Accurate solutions can be found with fewer Chebyshev polynomials as compared to a symmetrical, unscaled grid. This speeds up the stability code significantly, because the computational time of the eigenvalue analysis is proportional to the number of polynomials. This follows the relation given in equation 2.15.

2.4. Eigenfunction filtering

A crucial part of the linear stability tool which requires elaboration is the use of eigenfunction filters to determine the correct eigenvalue from the spectrum produced by the Orr-Sommerfeld solver code. As is explained in section 2.3, we obtain as many eigenvalues as Chebyshev polynomials used to discretize the boundary layer velocity profile. By utilizing characteristics of an eigenfunction it can be determined if the corresponding eigenvalue is the required kind of solution. To do so, the eigenfunctions are passed through several filters until only the correct one remains.

2.4.1. Utility

The largest drawback of filtering is the computational time, as the process uses approximately 1-2% of the total computational time of the stability code. Although some steps are relatively long, it prevents manual interaction with the Orr-Sommerfeld solver. This is the key feature of the linear stability tool and it opens up the possibility of large numbers of analyses without interaction, which is a necessity for optimization routines, for example. Also, using the eigenfunction makes the filtering procedure independent from previous eigenvalue results. This is in contrast to eigenvalue tracking algorithms, which need an initial solution from which is extrapolated by incrementally adjusting the parameters within the solver. Instead, filtering allows for any point within the parameter range to be evaluated on its own, in any order. This has large implications for computational time when making use of parallel processing, where the order of computations is not guaranteed and independence is a necessity. In that regard, using automated filtering of eigenvalues leads to large improvements in computational time.

2.4.2. Eigenfunctions

Within the eigenvalue spectrum, several branches of roots can be identified as similar types of solutions. The spectrum previously shown in figure 2.4 is repeated with these different groups annotated in figure 2.8. Compared to the dominating root, the eigenfunctions of these groups have specific features. These features are used to filter the eigenvalue from the list of unwanted eigenvalues.

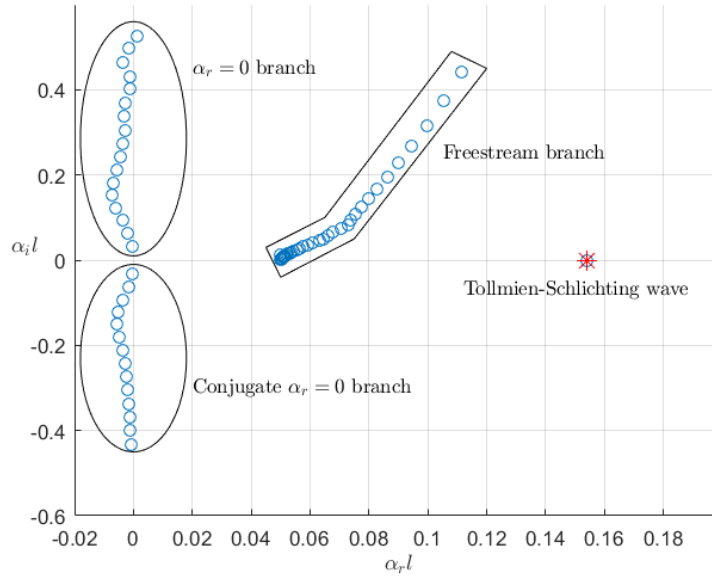


Figure 2.8: Characteristic branches of the eigenvalue spectrum

The expected form of the eigenfunction of the dominating root is shown in figure 2.9, subfigure (a) for TS at $\omega l/U = 0.05$ and $\beta l = 0$ and subfigure (b) for CF at $\omega l/U = 0$ and $\beta l = 0.5$. The eigenfunction consist of a real and imaginary part, with the real part being equal to the disturbance of the velocity profile in the y direction. Note the differences in scale on the vertical axis. The shape changes per case and type of instability, but shows several consistent features compared to the unwanted branches.

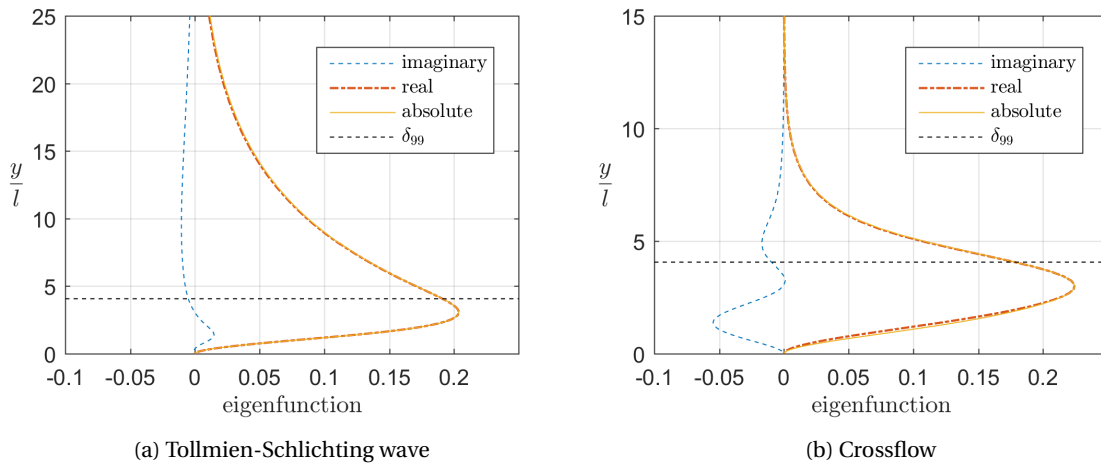


Figure 2.9: Characteristic eigenfunctions shapes

1. The eigenfunction of the dominant mode consists of a single, smooth maximum, or 'bulge'. There are no additional peaks other than the maximum, apart from the rare event of a cross-flow velocity profile with multiple inflection points. Such a profile occurs in boundary layers with alternating sign of the pressure gradient; each such switch starts a new inflection point. The eigenfunctions of the group of modes labeled as the *freestream* branch in figure 2.8 do not show a single maximum. On the contrary, within the bulge several alternating errors in the imaginary and real components are found, which can best be described as a higher order harmonic, see figure 2.10c.
2. The disturbance is located close to the wall, within the majority of the shear layer of the velocity profile. Both real and imaginary components of the eigenfunction decaying towards 0 according to the $e^{-\alpha_r y}$,

although the asymptotic trend of TS reaches far further into the freestream than CF. The eigenfunctions related to the eigenvalue branches in figure 2.8 labeled as the $\alpha_r = 0$ branch do not show this behaviour: The harmonics of the Chebyshev polynomials exist over the entire y/l range, see figure 2.10a. Some of these modes were also found within the *freestream* branch. The eigenfunctions and eigenvalues of this type share a trend in that eigenvalues with increasing imaginary components are higher order harmonics.

3. The imaginary component by definition is zero at the same y/l as the maximum of the real (and thereby absolute) component [40]. In other words, the difference between the real and absolute components within the bulge is always very small.
4. The phase angle, defined by equation 2.20, was used to create a filter to distinguish the dominant root from other correct, but non-dominant roots. For example, cross-flow profiles with multiple inflection points have seen to produce spectra in which the same number of distinct roots with their expected eigenfunctions are present. There was hope that the phase angle would be able to select the most dominant root by virtue of the phase angle sign in the shear layer of the profile [40]. For most simple cases, the phase angle proved to be positive in this region. Unfortunately, no robust correlation was found that could be adequately used as a selection process, but it has been included in this list for completeness.

$$\phi = \tan^{-1} \left(\frac{\Im}{\Re} \right) \quad (2.20)$$

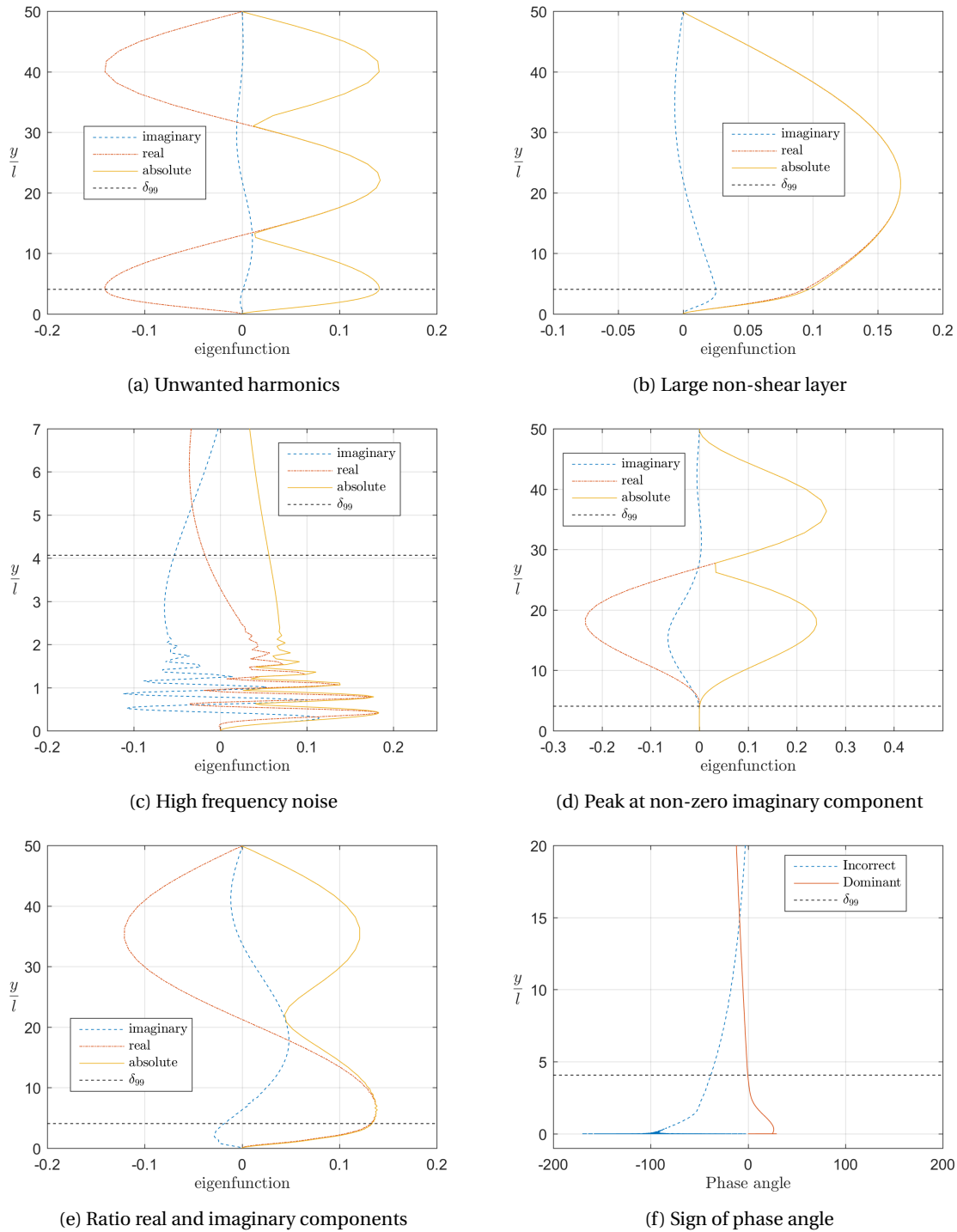


Figure 2.10: Application of the eigenfunction filters

2.4.3. Filters

Several different types of filter have been devised to eliminate erroneous roots, based on the observations made above. These filters are used in succession until a single eigenvalue remains. Some filters start with a strict condition which removes all eigenfunctions. In that case, the condition is incrementally relaxed until at least one eigenfunction is passed on. The filters are sorted by a combination of decreasing robustness and increasing strictness. Each filter description refers to a different subfigure of figure 2.10.

1. **Single maximum close to the wall 2.10a** A consistent characteristic of the disturbance is a maximum close to the wall surface. This is explained by the first point in the previous section. Eigenfunctions with a maximum peak at $\eta > \eta_{max}/2$ are removed. This filter is both fast and robust.
2. **Mean non-shear layer 2.10b** The eigenfunction of the correct root asymptotically reaches an absolute value of 0 when moving further from the wall surface. The filter removes those roots which have a mean absolute non-shear layer of more than 20% of the absolute maximum value. The removal of incorrect peak locations from the previous filter is necessary for this calculation to work.
3. **Noise 2.10c** The eigenvalues in the main branch of roots are similar to the correct root, but their eigenfunctions contain fluctuations. This is explained by the second point in the previous section. The fluctuations can be identified by counting the alternating sign of the gradient of the function. The filter at first removes all eigenfunctions with more than 3 changes in sign of the gradient. This number is increased in increments of 1 until at least one eigenfunction passes the test. Also, this filter is applied in sequence to the absolute, real and imaginary components of the eigenfunction. This is a result of an unpredictable origin of noise in either the imaginary or real component, which might cancel out in the absolute sum. To ensure a robust filtering process, each individual component is checked.
4. **Location of maximum absolute/real and zero of imaginary component 2.10d** The η at the maximum of the absolute component is compared to the η at the minimum value of the imaginary component. It is expected that these points coincide, including a relative margin of 5% to allow for rounding errors. This method is taken from the third point in the previous section.
5. **Ratio of components 2.10e** The eigenfunction of the correct root is generally composed of large real and small imaginary components, also taken from the third point of the previous section. The three components are integrated individually over the eigenfunction height. The difference between the integrals is calculated and inverted, thereby amplifying identical integrals (i.e. $1/0 = \infty$) and attenuating differences. All remaining roots are compared simultaneously, in that those roots which lie above the mean pass the filter. The bulge of each eigenfunction is excluded from the integration process to make this filter more robust. Excluding the bulge is necessary to remove a domain in which the the magnitude between components can be much larger between eigenfunctions, skewing the averaging process. Also, weak cross-flow eigenfunctions do not show a large real component and might not successively pass the filter if the bulge is included. As such, this filter is placed at the later stage of the filtering process.
6. **Sign of the phase angle 2.10f** The integrated value of the phase angle is expected to be a positive value, as explained by the fourth point in the previous section. Therefore, the phase angle of the disturbance is integrated and checked whether it is positive or negative. The fluctuations at the wall and the non-shear layer are removed from this calculation. Although based on a physical interpretation of the eigenfunctions, this filter has not yet been successful. Therefore, this filter is not used at this time.

In the rare case the above filters did not remove all but one eigenvalue from the list, the eigenfunction with the largest imaginary component is selected. This decision is not based on a characteristic of the dominating eigenfunction, but proved to be useful when two or three eigenvalues were remaining after all filters were utilized. Usually, these additional eigenvalues represent multiple inflection points and still have a physical basis. However, the stability tool can only handle a single value as output from this process. Also, selecting an extreme case (instead of an average, for example) prevents a crash of the code when the discretization of the velocity profile was insufficient for any reason. Other parts of the linear stability tool are capable of removing eigenvalues from the complete solution if they are statistical outliers at a given Reynolds number.

2.5. Pre-process

The calculation of several properties of the boundary layer is required as preparation for the stability code. This pre-processing will yield the necessary secondary derivatives of the velocity profiles, plus additional values to guarantee feasible and fast calculations of the Orr-Sommerfeld solver. In this section, the computation of the starting points and the discretization in Reynolds number will be discussed in detail.

2.5.1. Critical Reynolds number

For a given velocity profile, the lowest Reynolds number at which the boundary layer can be unstable is named the critical Reynolds number. It is obtained by calculating the neutral curve of the stability diagram, i.e. the locus of all points of zero amplification in the ω -Reynolds or β -Reynolds space (in our focused perspective of incompressible 2.5D boundary layers). As such, it can be computed using the stability tool. However, it is also possible to estimate this point for the TS type of instability using empirical trends. Such an estimation is useful to limit the domain and focus the computational time on regions which are expected to be unstable and require detailed resolution.

$$\begin{aligned}\theta &= \int_0^\infty \frac{u}{U_e} \left(1 - \frac{u}{U_e}\right) dy \\ \delta^* &= \int_0^\infty \left(1 - \frac{u}{U_e}\right) dy \\ H &= \frac{\delta^*}{\theta}\end{aligned}\tag{2.21}$$

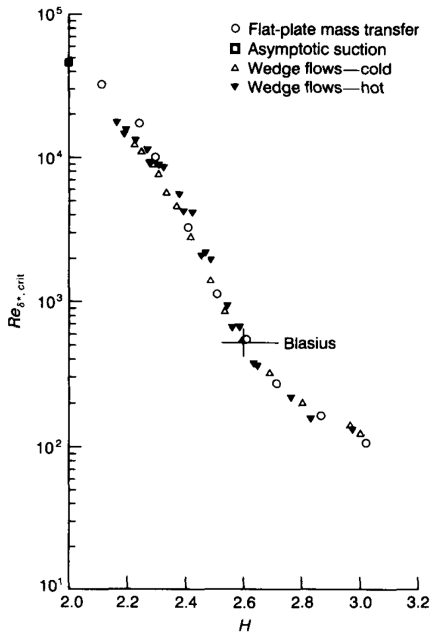


Figure 2.11: Critical Re_{δ^*} versus shape factor [21]

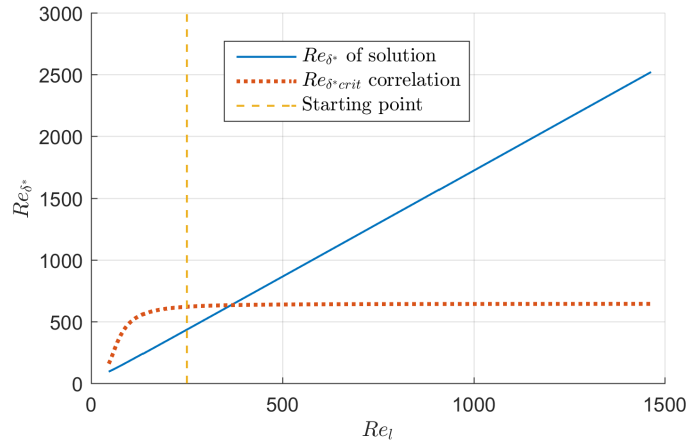


Figure 2.12: Comparison of Re_{δ^*} solution with the critical Re_{δ^*} from the shape factor correlation

The trendline used is a correlation between the boundary layer shape factor, often denoted with H , and the critical Reynolds number with the displacement thickness δ^* as characteristic length. Both properties are easily computed from the boundary layer solution using equations 2.21. The correlation is shown in figure 2.11, taken from White [21]. For each station in the boundary layer solution (denoted by Blasius length Reynolds number Re_l) the shape factor is used to determine the local critical Reynolds number using this figure, i.e. $Re_{\delta^* crit} = f(H)$. This is compared to Re_{δ^*} of the solution to estimate whether the local velocity profile will be unstable, as is visualized for a flat plate boundary layer in figure 2.12. The first point where the critical Reynolds number becomes lower than the Reynolds number of the solution is the expected critical Reynolds number of the boundary layer being analyzed. As can be seen, the leading edge point singularity causes the critical Reynolds number to decrease towards zero, resulting from a large value of the shape factor.

This is expected, as the boundary layer thicknesses δ^* and θ approach zero at the leading edge, making the shape factor ill-defined. A safety factor on the intersection will be used for the starting point of the tool.

2.5.2. Wall curvature error

The boundary layer solver suffers from leading edge singularity at the first iterations. In the unprocessed boundary layer solution, the wall curvature of the velocity profiles was oscillating around the predicted wall curvature. This problem has been reduced significantly with the method described in section 2.2.4. However, a check is performed to see if the numerical wall curvature is identical to the derivative of the external pressure gradient. This will be discussed in further detail in chapter 3.

2.5.3. Reynolds number stepsizes

The N-curves are calculated by trapezoidal integration of the amplifications α_i for one physical frequency or wavelength. To minimize the error of this linear integration, the fine grid has to be placed in regions of high *curvature* of the α_i contours, defined by the equations under 2.22. In the direction of the variable dimension (either ω or β) the α_i contour curvature is observed to be almost constant. The contours follows a quadratic trend for a given Reynolds number, shown in figure 2.13. This figure shows the results of the calculations at nine separate Reynolds numbers, ranging from stagnation up to the separation point and thereby including a range of profile shapes. Therefore, an equidistant spacing along the variable dimension will be sufficient for the fine grid at any fixed Reynolds number.

$$\alpha_{i,\omega\omega} = \frac{\partial^2 \alpha_i}{\partial \omega^2} \left(\frac{l}{U_e} \right)^2 \quad \alpha_{i,\beta\beta} = \frac{\partial^2 \alpha_i}{\partial \beta^2} \frac{l}{l^2} \quad \alpha_{i,xx} = \frac{\partial^2 \alpha_i}{\partial x^2} \left(\propto \frac{\partial^4 u}{\partial x^2 \partial y^2} \right) \quad (2.22)$$

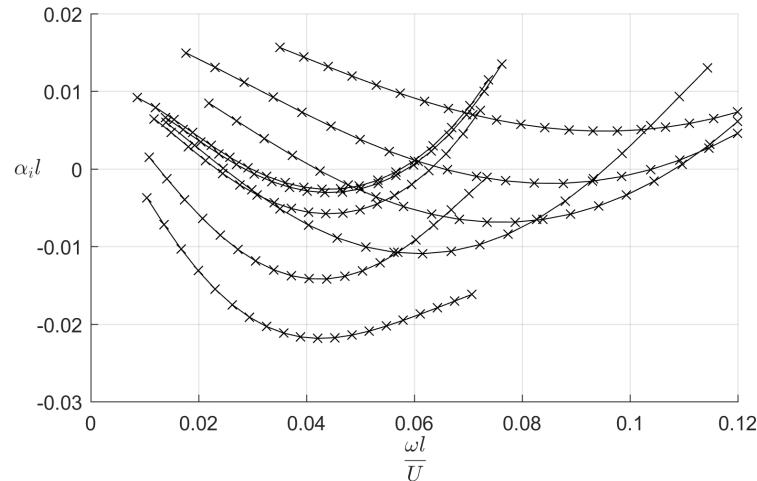


Figure 2.13: Variation of amplification with ω of TS instability at various Reynolds numbers

Curvature of the stability contours along the Reynolds number dimension is not constant, as the solutions vary between with the local boundary layer profiles shape. The α_i magnitude of the solution is proportional to the wall curvature (see equation 2.22). Therefore, the boundary layer is analyzed to find the stations which minimize the linear integration error, using the method visualized in figure 2.14. The error of linear integration is predicted by applying a linear interpolation of a boundary layer parameter known at every station using only several equidistant stations. This is illustrated in figure 2.14a. The number of stations is limited by the maximum size of the fine grid defined by the user. The error between the true solution and the interpolated value is highest at the midpoints between the interpolated values, see figure 2.14b. This error is used as a measure to determine the fineness of the grid, i.e. a larger error indicates that the solver should use a high fineness at that station. The estimated error method has proved to be more robust than taking the second x -derivative of the wall curvature and using the magnitude of the function to refine the grid spacing. Numerical errors became too large to use this derivative as an effective measure.

The last step to convert the interpolation error to a grid spacing is to integrate the absolute error at the mid-points indicated in figure 2.14b. At constant intervals of this cumulative error a grid point is placed. The

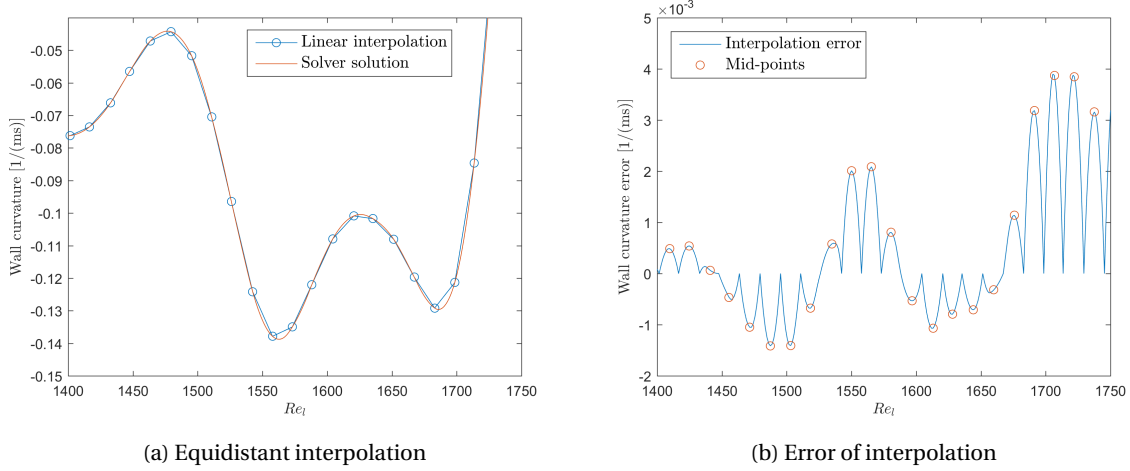


Figure 2.14: Estimate of interpolation error of the N-curves

stepsize of the interval has been manually adjusted until a suitable discretization was obtained, separately for TS and CF instability. The stepsize is linked to the chord-based Reynolds number of each case, as to scale with different operating conditions. The physical quantity that is used depends on the type of instability to be analyzed. For TS calculations this is the wall curvature of the velocity profiles, as was explained in section 2.3. On the other hand, for CF calculations this is the difference between the maximum and minimum cross-flow velocities, measured perpendicular to the inviscid streamline. This is simply a handle on the magnitude of crossflow which causes this type of instability and has proved to be effective.

2.6. Verification

The solution of the boundary layer and the stability solver are tested by verifying the calculated results to known similar flows. The following section explains the similar solutions of Blasius and Falkner-Skan-Cooke, how they are obtained and the comparison of the boundary layer solver and stability solver with these results.

2.6.1. Flat plate

A well known similar flow is the solution to the flat plate, or the Blasius flow. It is obtained by introducing the similarity variable η , given by equation 2.23, with which the stream function ψ in equation 2.24 is normalized to $f(\eta)$, so that it is a function of η alone [21]. Note, this definition is identical to the normalization used throughout the linear stability tool, hence its namesake. Substitution of the velocity components obtained through 2.25 into the momentum equation (2.2) and the condition $dU/dx = 0$ results into the Blasius equation, given by equation 2.26, in which a prime denotes differentiation with respect to η .

$$\eta = y \sqrt{\frac{U}{\nu x}} \quad (2.23)$$

$$\psi = \sqrt{\nu U x} f(\eta) \quad (2.24)$$

$$\begin{aligned} u &= \frac{\partial \psi}{\partial y} \quad (= U f'(\eta)) \\ v &= -\frac{\partial \psi}{\partial x} \quad \left(= \sqrt{\frac{\nu U}{x}} (\eta f' - f) \right) \end{aligned} \quad (2.25)$$

$$f''' + \frac{1}{2} f f'' = 0 \quad \begin{cases} f(0) = 0 \\ f'(0) = 0 \\ f'(\infty) = 1 \end{cases} \quad (2.26)$$

The boundary conditions for this third order differential equation are the no-slip condition at the wall for the stream function f and velocity f' , as well as the velocity approaching unity in the freestream, summarized in 2.26. The solution of this boundary value problem can be found numerically with the shooting method by varying the velocity profile gradient at the wall $f''(0)$ and using the end boundary condition at $\eta = \infty$ as the error function. The obtained solution is given in figure 2.15, which is validated with literature results [21]. The physical velocity profiles can be obtained by the transformations given between brackets in equation 2.25.

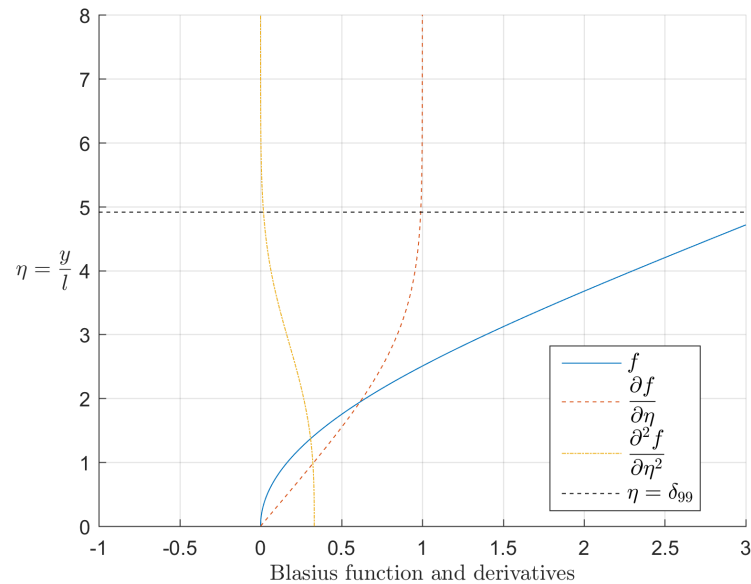


Figure 2.15: Solution to the Blasius equation

Boundary layer solver When executing the boundary layer code with a uniform external velocity we can determine the accuracy for the Blasius case. In figure 2.16 the absolute difference between velocity profiles of the solver and the similar solution are given. Several stations have been plotted, including the first station at $x/c = 0.00$ to indicate the initialization of the boundary layer. The maximum error occurs at the first stations, but is of negligible magnitude. In the freestream the accuracy of the profiles approach machine precision, so it can be said that the velocity profiles for zero pressure gradients are perfectly resolved.

Stability diagram The linear stability tool can easily be configured to solve the Blasius profile for a range of Reynolds numbers and frequencies, reproducing the stability diagram. To compare the results with data from literature, the characteristic length has been changed from l to δ^* . The diagram is shown in figure 2.17, indicating several contours of constant amplification $\alpha_i \delta^*$. The bold line is the neutral contour, separating the unstable from the stable regions of the diagram, with a critical Reynolds number $Re_{\delta^*} = 521$. This value is a good verification case, as it shows that the data corresponds with the literature value of 520 [13].

The stability diagram has been constructed by solving a equi-spaced grid of points in the domain and applying a cubic spline interpolation on surface of $\alpha_i \delta^*$ results. This cubic spline guarantees a smooth solution in between the grid points, but is not extrapolated outside the original domain. This process will be discussed in detail in chapter 3. For now, we see that the tool can predict the Tollmien-Schlichting wave amplifications in a wide range of frequencies and Reynolds number in the absence of a pressure gradient.

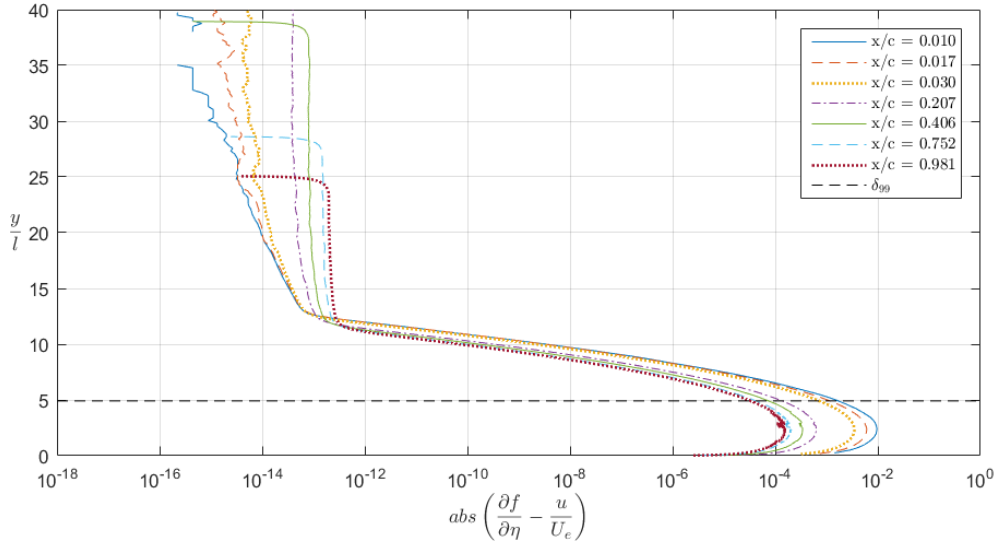


Figure 2.16: Error in solver velocity profiles compared to Blasius similar solution

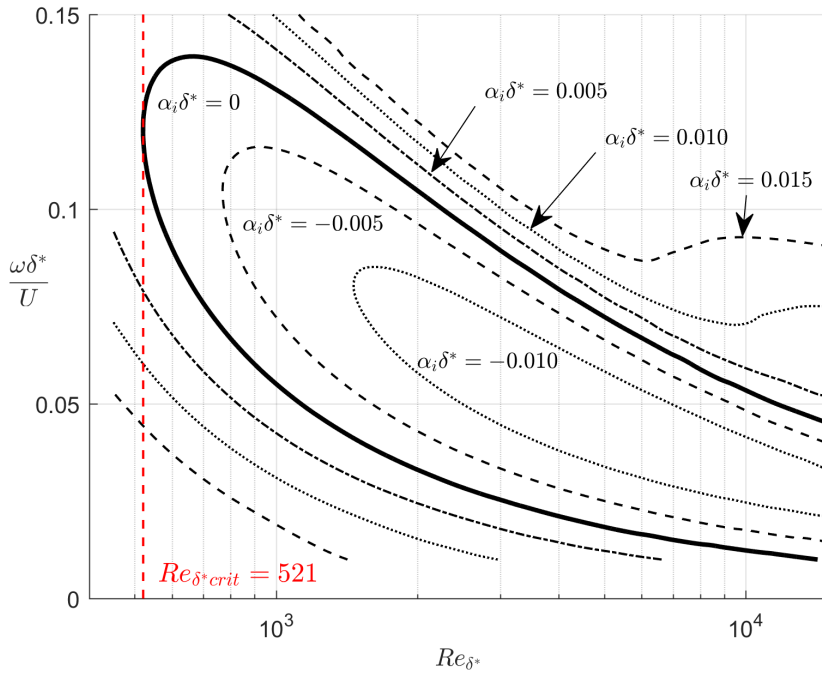


Figure 2.17: Stability diagram of Blasius profile

2.6.2. Falkner-Skan

The generalized formulation of the Blasius equation can be obtained when assuming a power-law external velocity distribution, as given by equation 2.27, and modifying the similarity variable η to include the parameter m , as in equation 2.28. The Falkner-Skan parameter m is written to the Hartree parameter β using equation 2.29, which together with the new similarity variable can be used to find the Falkner-Skan equation, given by equation 2.30. Derivation and further discussion can be found in White [21]. However, some ambiguity exists in the exact definition of the transformation from y to η : White uses a notation using U_e , which can be shown to be equivalent to substituting equation 2.27 into 2.28.

$$U_e = Kx^m \quad \left(= U_\infty \left(\frac{x}{L} \right)^m \right) \quad (2.27)$$

$$\eta_{FSC} = y \sqrt{\frac{m+1}{2} \frac{U_\infty}{\nu L}} \left(\frac{x}{L}\right)^{\left(\frac{m-1}{2}\right)} \quad (2.28)$$

$$\beta = \frac{2m}{m+1} \quad \left(m = \frac{\beta}{2-\beta}\right) \quad (2.29)$$

$$f''' + f f'' + \beta(1 - f'^2) = 0 \quad (2.30)$$

The boundary conditions and numerical solving method for the Falkner-Skan equation are identical to the Blasius case, but a choice has to be made regarding β . The physical interpretation of this parameter is the external pressure gradient associated with the flow over a wedge of half angle $\beta \cdot \pi/2$, which will give unique results in the range $-0.19884 < \beta < \infty$. Some typical solutions are the Blasius solution for $\beta = 0$, stagnation point flow for $\beta = 1$ and separation at $\beta = -0.19884$ [21]. The first derivative of the solution of the Falkner-Skan equation is plotted in figure 2.18a, for a nonlinear range of β values.

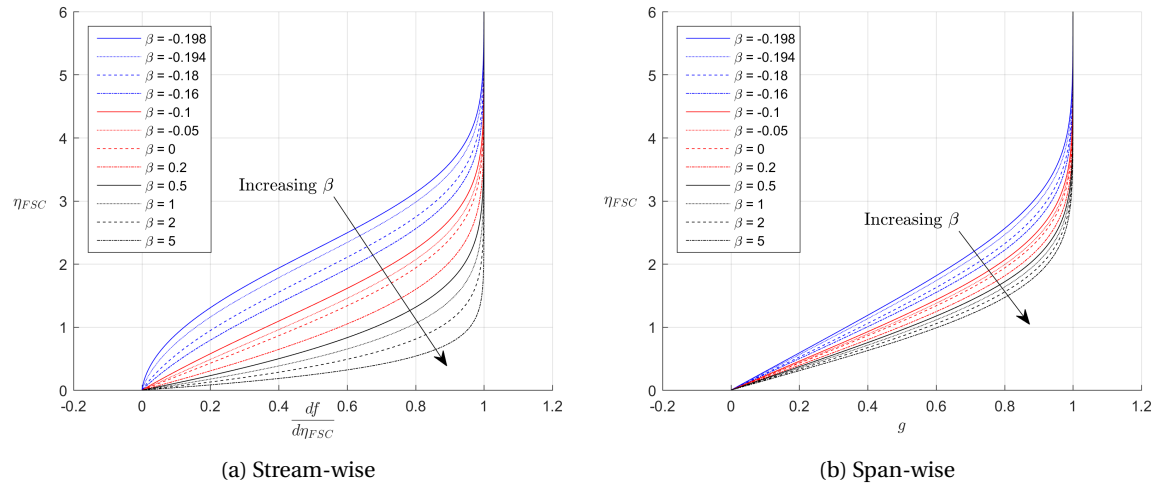


Figure 2.18: Solutions to the Falkner-Skan(-Cooke) equations

The Falkner-Skan equation can be expanded to include three dimensional flow by including a perpendicular component with no external pressure gradient. This formulation is also known as the Falkner-Skan-Cooke equation (2.32) and is obtained by substituting equation 2.31 into w momentum equation 2.9.

$$w = W_e g(\eta_{FSC}) \quad (2.31)$$

$$g'' + f g' = 0 \quad \begin{cases} g(0) = 0 \\ g(\infty) = 1 \end{cases} \quad (2.32)$$

The velocity profile g is the span-wise equivalent of f' . The absence of a pressure gradient (or the forcing term in the momentum equation) reduces the third-order non-linear differential equation to a second-order linear one. The solution is given in figure 2.18b. Note, since transforming to physical crossflow profiles now depends on both the parameter β and the 'sweep angle' inherent in W_e , the similar solution for one β can be used to obtain a family of solutions as a function W_e .

Boundary layer solver The boundary layer solver was evaluated using an external velocity distribution equivalent to a Falkner-Skan edge velocity with $m = 0.5$ according to equation 2.27. Several velocity profiles of the solution were selected and compared to the similar solution. The error to the reference is shown in figure 2.19. A number of interesting features are visible in this graph. First, there is an initial error that quickly decays, expected from the issues relating to an accelerating inflow, discussed in section 2.2.4. It is visible that the boundary layer of the profiles approaches the limiting accuracy of both the solver and the similar solution at $x/c = 0.2$, where oscillations in the error start growing. Finally, the top of the solver mesh can be observed

by a decrease in error where the freestream boundary condition is being met. Logically, this kink in the error occurs at decreasing η_{FSC} as the boundary layer grows, because the solver has a mesh of constant height. It also illustrates the remaining error in the formulation that was postulated in section 2.2.4: It is observed that the velocity profiles have a freestream which consistently over-/undershoots the boundary condition in ac-/decelerating flow. Luckily, this error is small in the majority of the solution.

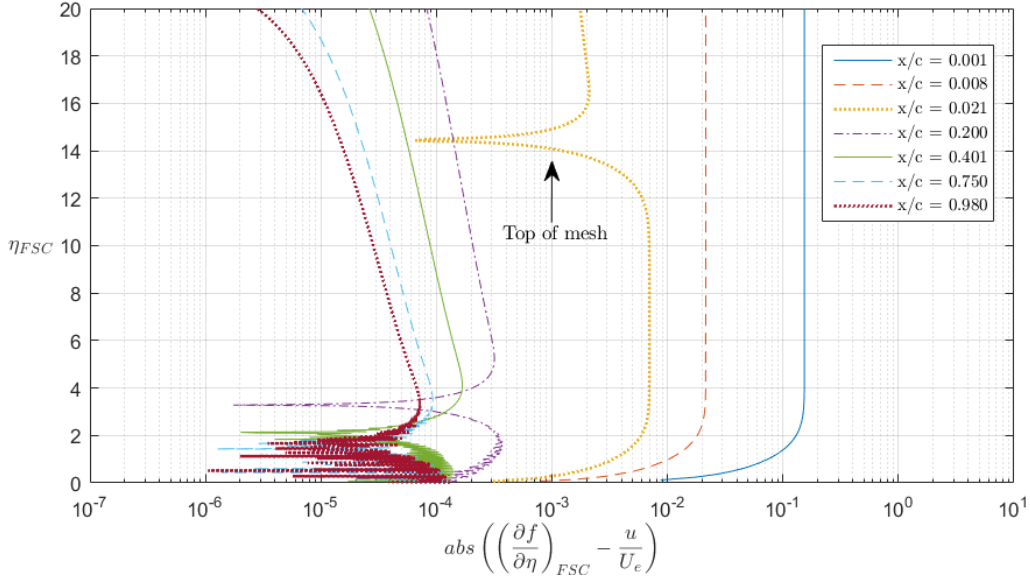


Figure 2.19: Error in solver velocity profiles compared to Falkner-Skan similar solution

Stability diagram The stability diagrams for a range of Hartree parameter (β) values have been calculated using the tool, see figure 2.20. It shows the neutral curves for a range of Hartree parameters. Like the Blasius stability diagram, the characteristic length is δ^* . The stability surfaces were all resolved, but not always as accurate: The separation profile at $\beta = -0.19884$ has an unstable domain that spans a large part of the diagram and did not resolve properly everywhere, see the dotted end of its neutral curve. Also, the automated discretization was not able to resolve all values at $Re_{\delta^*} > 10^4$. Both these cases have not been observed to occur when analyzing airfoil pressure distributions in a large range of freestream Reynolds numbers. Therefore, it is safe to assume the tool resolves velocity profiles corresponding to large gradients accurately in all plausible subsonic conditions.

2.6.3. Similarity

The Falkner-Skan-Cooke solution in the inviscid streamline reference frame is given in figure 2.21. Both the true streamwise and true crossflow components are plotted in the same figure, normalized to U_e/W_e . This figure illustrates the capability of this similar solution to reproduce the crossflow bulges in either direction for pressure gradients of different sign. However, the similar solution is not suited for boundary layers with alternating pressure gradients, which are inherently not self-similar. As was discussed in chapter 1, an alternating pressure gradient will produce a secondary cross-flow bulge, see figure 1.6a.

As will be shown in chapter 3, there is an inherent difference between intricate numerical three-dimensional boundary layer solutions and these similar flow solutions. The cross-flow component of three-dimensional boundary layers only follows similar solutions in theoretical cases. As such, stability of general boundary layers requires detailed numerical evaluations to reach sufficient accuracy to obtain a practical transition prediction. Therefore, the linear stability tool is required when considering arbitrary cases with reasonable accuracy, because no simple correlation method is available.

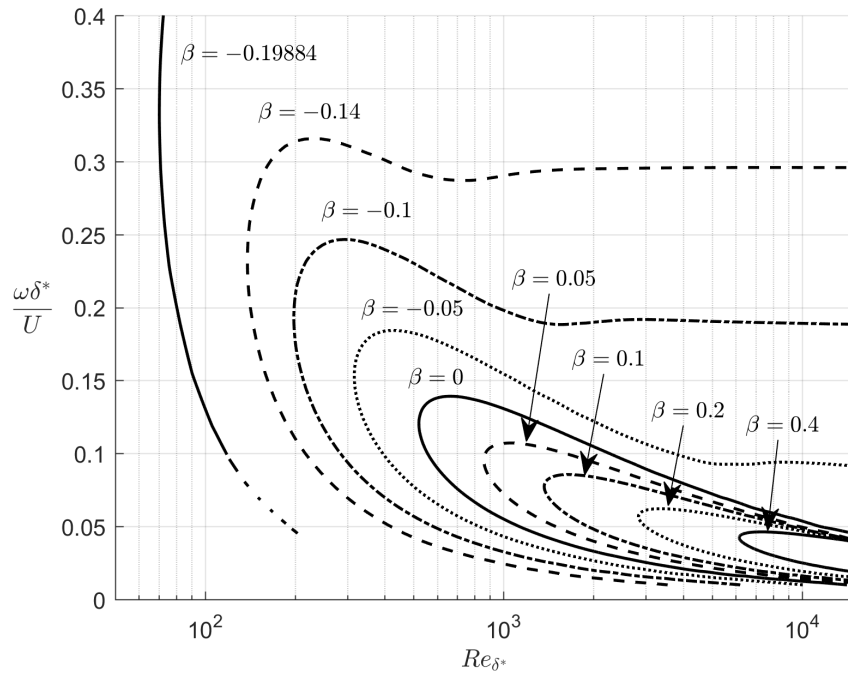


Figure 2.20: Falkner-Skan stability diagram neutral curves

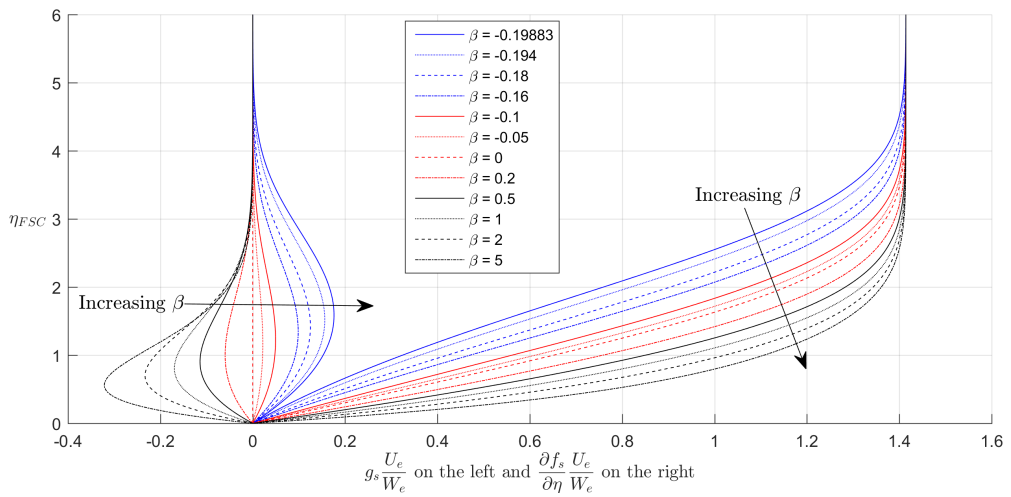


Figure 2.21: Falkner-Skan-Cooke similar solution in the inviscid streamline reference frame

3

Case study

In addition to validation of the linear stability tool with respect to similar velocity profiles, it is of interest to do a case study and thereby analyze an airfoil from start to finish. The theory of chapter 2 is molded into a computational framework responsible for automatically resolving all computations. A dedicated chapter on the steps taken throughout one calculation cycle will illustrate this framework, as it is critical in the utilization of the tool. Therefore, the intermediate solutions within the stability tool will be reviewed. First, the case is described and the inputs are shown. Then the solving procedure for the upper side of the airfoil is described, starting with the laminar boundary layer solution. This is then analyzed to prepare the stability code and the Orr-Sommerfeld solutions are obtained. The N-curves that are used to estimate transition for a given critical N-factor are generated. Finally, the creation of a surrogate model for an airfoil is discussed.

3.1. HSNLF(1)-0213 airfoil

The airfoil to be reviewed is the HSNLF(1)-0213 airfoil, which can be obtained from online sources¹. The acronym stands for *high speed natural laminar flow* and the airfoil was designed at Langley Research Center for application on a one engine, unswept business jet [41]. The data points are shown in figure 3.1. This airfoil will in the future be used to calibrate the stability code in this work by comparing the N-curve envelopes with transition points in a windtunnel. Its asymmetrical design was found to be suitable to control the amplifications from both TS and CF instabilities.

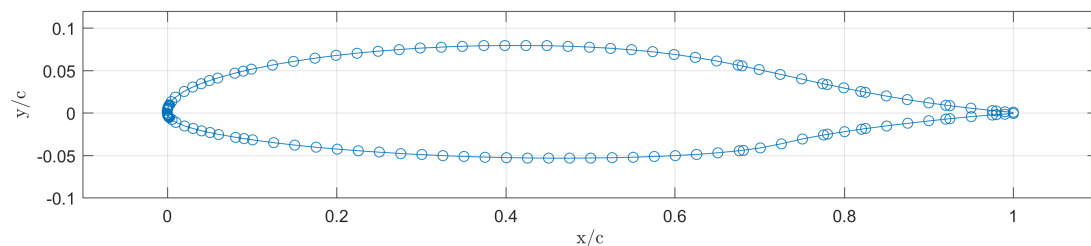


Figure 3.1: HSNLF(1)-0213 airfoil definition

3.1.1. Pressure distribution

The pressure distribution on either side of the airfoil is shown in figure 3.2. These results are generated using MSES for one unique set of parameters [42]. These will be used throughout the case study, so they are listed in table 3.1 below. The free transition critical N-factor in MSES was set to 15 to prevent an early transition with an overestimated (turbulent) boundary layer thickness influencing the pressure distribution. Note, when used in optimization schemes, it is useful to force transition to the leading edge. This prevents laminar separation and can always be updated with improved values when the tool has run once.

¹www.airfoiltools.com

Table 3.1: Case study parameters

Symbol	Parameter	Value	Unit
h	Altitude	0	m
ν	Kinematic viscosity	$1.461 \cdot 10^{-5}$	m^2/s
c	leading edge orthogonal chord	0.7	m
α	Angle of attack	2	degrees
C_l	Lift coefficient	0.32	-
Λ	Sweep angle	30	degrees
U_∞	Chord-wise freestream velocity	62.60	m/s
Re	Chord-wise Reynolds number	$3.00 \cdot 10^6$	-
Re_∞	Freestream Reynolds number	$4.00 \cdot 10^6$	-
Q	Freestream velocity	72.28	m/s
W_∞	Span-wise freestream velocity	36.14	m/s

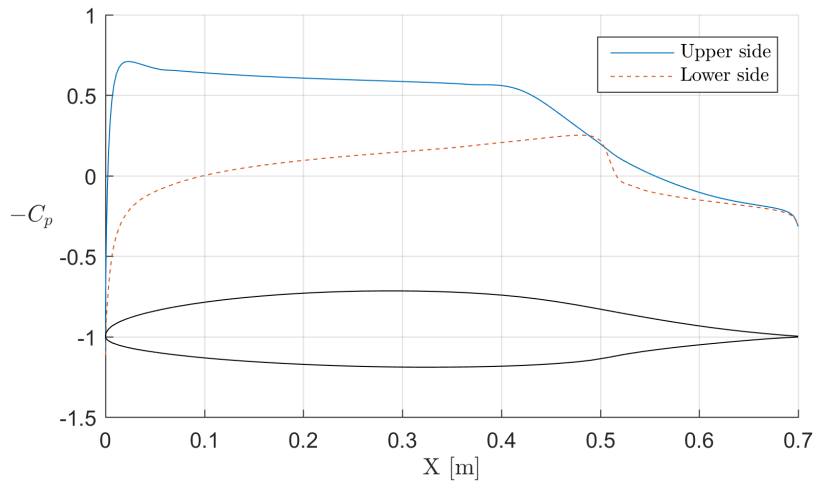


Figure 3.2: HSNLF(1)-0213 airfoil with pressure coefficient distributions

3.2. Boundary layer solution

The pressure distribution or the external velocity distribution of MSES is the input to the boundary layer solver. In case of cross-flow calculations, the span-wise velocity component W_e is used to generate the velocity field in Z as well, denoted with w . The tool can integrate the boundary layer until backflow is detected at the wall, indicating separation of the boundary layer. At this point, precision of the solution can no longer be guaranteed and the external pressure gradient is no longer accurate. As a consequence, all figures that follow are cut off at a given chord-wise station and do not reach from $x = 0$ to $x = c$.

The marching method is started with a small iterative procedure to produce the wall-normal velocity component v that is consistent with the inflow u according to continuity. Then, the wall curvature precision is guaranteed by averaging the solution 10 times. The result can be seen in figure 3.3. In general, the solution overlaps the theoretically predicted value. The error, normalized to the input values, increases at the point of minimum pressure, where the wall curvature should theoretically be zero. At the start of pressure recovery a second peak in the error can be observed. However, the relative error is close to, or below 1% for the majority of the boundary layer length.

Another test of the overall numerical precision is the evaluation of the boundary layer thicknesses shown against the left vertical axis in figure 3.4. The momentum and displacement thicknesses can be obtained by a per-station integration of the solution according to equations 2.21. The ratio of both thicknesses, the shape factor H , is indicated versus the right vertical axis. The shape factor follows the expected trend: A relative constant pressure equals the flat plate (Blasius) shape factor of 2.59. However, a numerical problem is seen to arise at the leading edge, in the area of a large negative pressure gradient. The boundary layer thicknesses are negative, which can be explained by observing the velocity profiles of the solution themselves.

The velocity profiles are the actual output of the boundary layer solver. The profiles plotted in figure 3.4

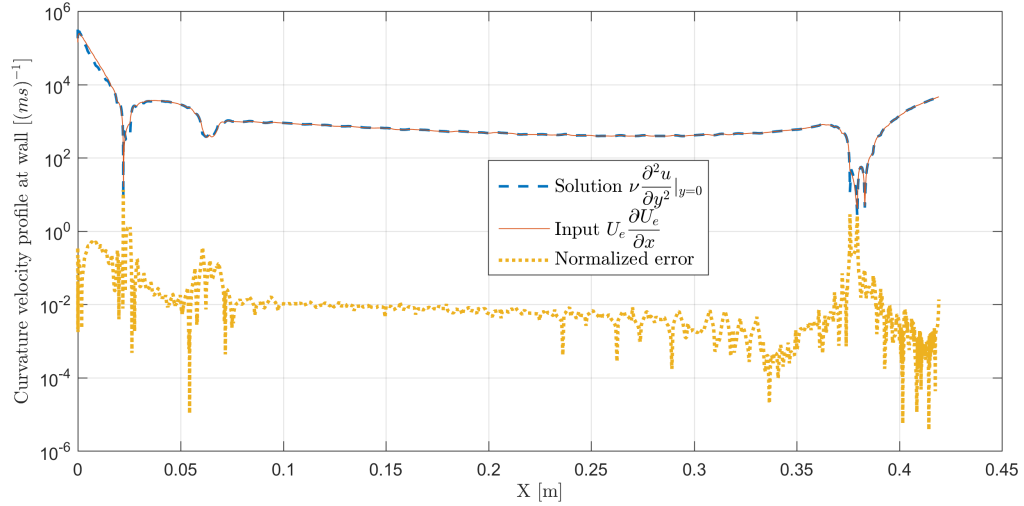


Figure 3.3: Wall force imbalance by comparison of wall curvature of input and solution

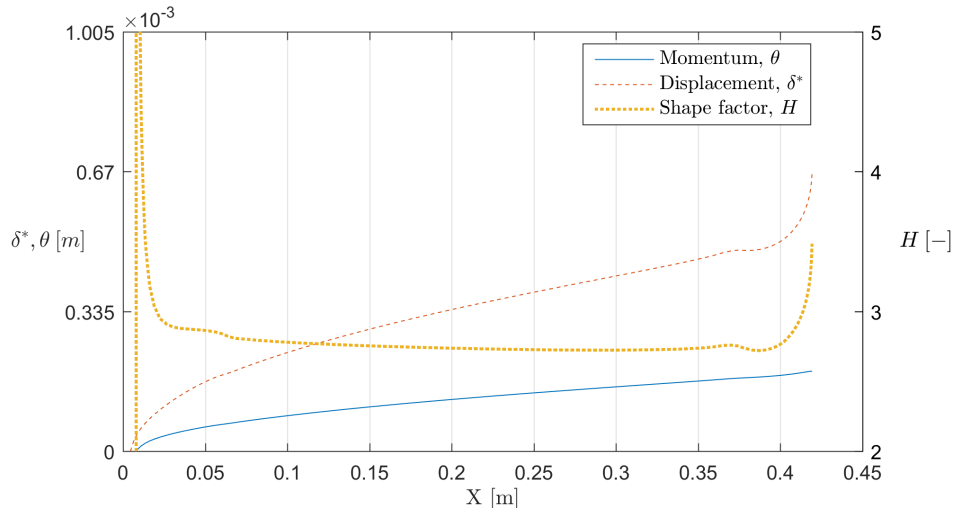


Figure 3.4: Boundary layer characteristic thicknesses

were selected in a non-linear distribution, including the first and last stations. While the marching method solves in physical units, for plotting purposes the profiles have been normalized in both dimensions. This is done with the Blasius length l in the wall-normal direction (see section 2.2) and the edge velocity U_e for the velocity. Therefore, the profiles close to the stagnation point are extremely coarse, with only a handful of grid nodes in the boundary layer itself.

The stream-wise profiles are shown in subfigure 3.5a. The first station of the solution is included and is clearly seen to be overshooting the freestream velocity, explaining the negative boundary layer thicknesses. Fortunately, this error is absent in the second profile, only 3 mm aft of the leading edge. The cross-flow component is shown in subfigure 3.5b, normalized to the same edge velocity U_e . The *true* cross-flow w_s , perpendicular to the external streamline, is far more illustrative of the state of the boundary layer than the span-wise component w . The error in the first station is amplified by normalization due to the low freestream velocity at the start of the boundary layer. Also, w_s can be seen to not be self-similar: the cross-flow reversed in direction in the vicinity of a pressure minimum. The initial negative pressure gradients cause negative cross-flow, or directed inboard (for positive sweep angles) while the positive (adverse) pressure gradient causes positive cross-flow towards the tip. This is a common problem on swept, tapered wings and will always occur if the pressure minimum is close to the leading edge.

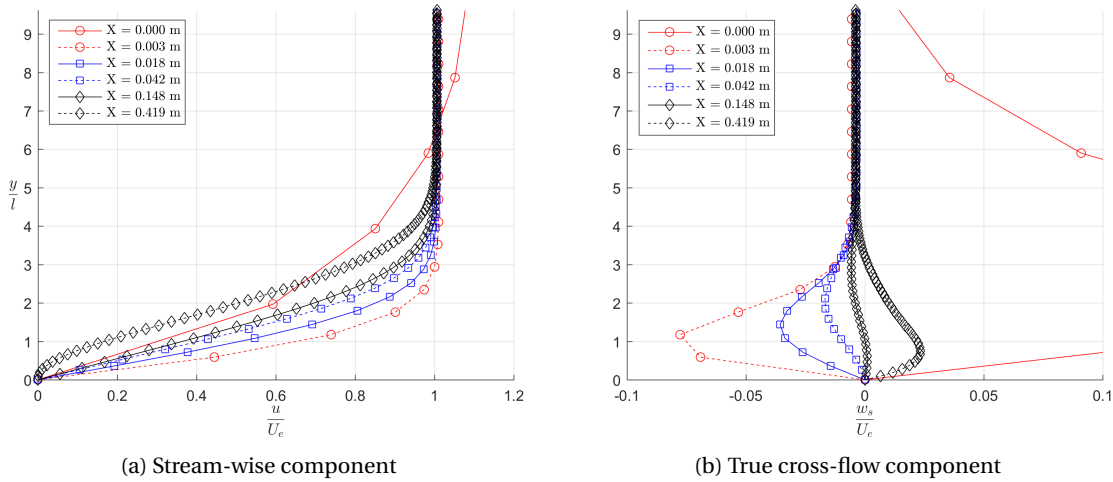


Figure 3.5: Boundary layer profiles at six separate stations

3.3. Stability solver preparation

After solving the laminar boundary layer it is necessary to process the result to prepare the stability solver. As was discussed in chapter 2, not all combinations of input variables are possible or necessary to calculate with the OS solver. The steps performed within the preparation code are discussed below.

Several boundary layer properties are computed separately from the boundary layer solver. Some of these were presented in preceding section 3.2, such as the boundary layer thicknesses. Also, the velocity fields are normalized and also computed in terms of the streamline reference frame instead of the leading edge orthogonal reference frame. The multiplication of the solution meshes with the rotation matrices uses most of the computational time within this process (i.e. 3 seconds).

3.3.1. Wall curvature

The numerical precision of the wall curvature was discussed in the previous section. Considering that the boundary layer code only corrected for a constant number of stations to minimize numerical error, the error has to be checked. Using the error curve seen in figure 3.3, the boundary layer is cropped up to the first station where the error is less than a certain threshold. For robustness, a multiple of the mean of this error over the boundary layer is used as threshold. So far, this verification of the curvature has been observed to not remove more than tenths of a percent from the solution in extreme case conditions.

3.3.2. Critical Reynolds number

The empirical correlation between shape factor H and critical Reynolds number Re_{δ^*} discussed in section 2.5 is computed next. As was explained, the point where the empirical critical Reynolds number from the correlation crosses the solution Reynolds number is close to the actual critical Reynolds number. In figure 3.6 it is clearly visible that the adverse pressure gradient on the upper surface, corresponding with a high shape factor, is expected to be unstable immediately after the pressure minimum. This can be seen when comparing the pressure coefficient distributions in figure 3.2 with predicted instability. Also, the numerical error in shape factor is visible in the jump of the correlated Re_{δ^*} . The onset of instability is used for the starting point of the OS solver grids for TS instability.

3.3.3. Grids

The starting points are used to remove part of the Reynolds range that will be evaluated by the OS solver. For TS the critical Reynolds number prediction and the wall curvature precision are used to determine the starting points, while for CF only wall curvature is relevant. The end point in Reynolds number is the end of the boundary layer solution, located at the point of laminar separation. What remains to be determined before starting the OS solver is the grid *spacing* along the Reynolds number. The coarse grids use an equidistant spacing to cover the total parameter space but the fine grid spacing is computed.

Regions of increased refinement are calculated using the interpolation error method discussed in section

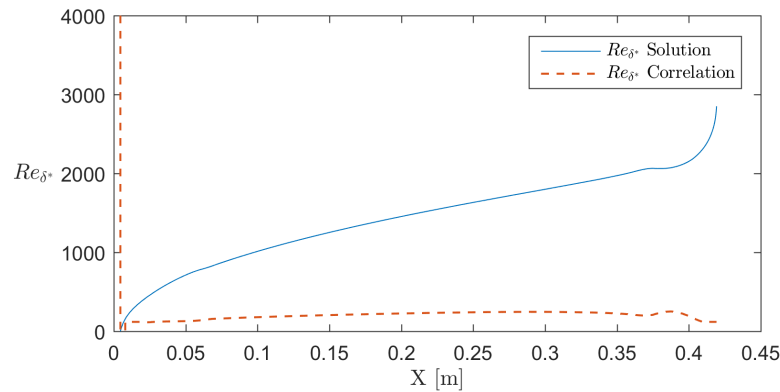
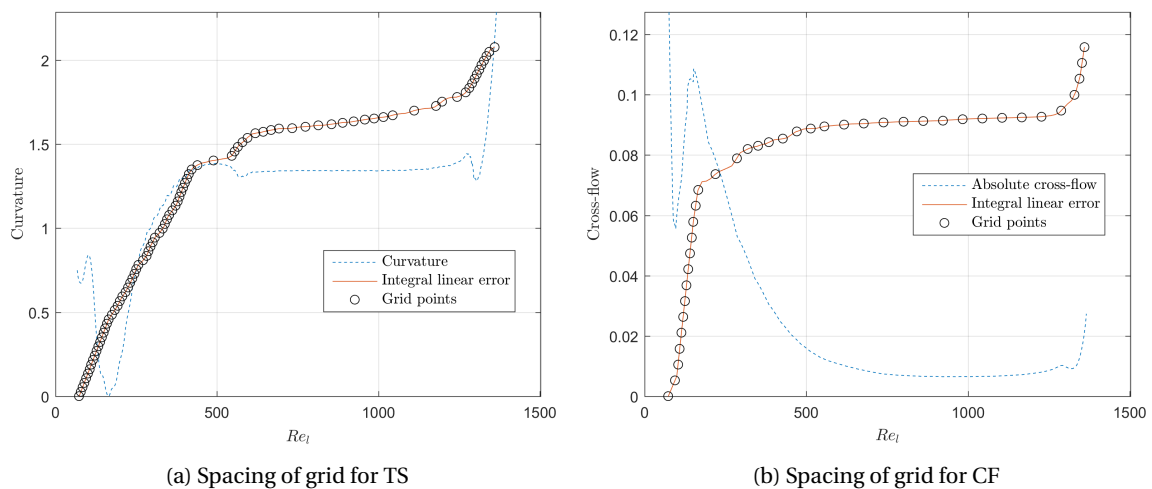


Figure 3.6: Critical Reynolds number comparison

2.5. For TS instability, the wall curvature in the chord-wise direction is used to compute the expected error, while for CF the true cross-flow component w_s is used. The cross-flow component with respect to the inviscid streamline has been computed for this purpose, and the difference between the maximum and minimum velocities is used as the parameter for this method.

As can be seen in figure 3.7, the integral of the linear error increases in areas with high curvature of the parameter. Additional points have been added in regions of zero to low curvature (a plateau in the error), to make sure there is a minimum discretization in the solver. One remaining issue is the high increase in discretization close to separation. The rapid change in external pressure gradient and velocity profile shape is properly captured by the method, but such detail is not necessary when the boundary layer solver already predicts separation. Currently, these regions claim a large portion of the solver time while the accuracy of the boundary layer solution in this region is not as precise.



(a) Spacing of grid for TS

(b) Spacing of grid for CF

Figure 3.7: Stability tool preparation grid spacing

3.4. Stability solver solution

The OS solver is executed using a pre-allocated grid of points, seen in figure 3.8. This allows for parallel processing of the OS solver, significantly reducing the computational time. To ensure adequate coverage of the parameter space, the solution is computed using a coarse grid at first and a fine grid afterwards for parameter ranges that will produce unstable solutions. The coarse grid evaluates points that require high discretization, up to 150 Chebyshev polynomials per point. Therefore, each point takes relatively long, but the high discretization makes it possible for all areas of the parameter space to be evaluated, see the black circles in figure 3.8.

After the solution of the coarse grid is known, a good estimate can be made into the level of instability across the parameter space. Using this information, the fine grid is applied at unstable locations only and can therefore be executed with low, but adequate, Chebyshev discretization at each point, see the blue stars in figure 3.8. At the most unstable points, the number of Chebyshev polynomials can be scaled to reach values as low as 40. The unstable domain is limited by a contour line slightly above $\alpha_i = 0$ as these areas will improve the detail of the N-curve envelope. The contours are shown by black dashed lines, which are linearly interpolated between the α_i values at the coarse grid points.

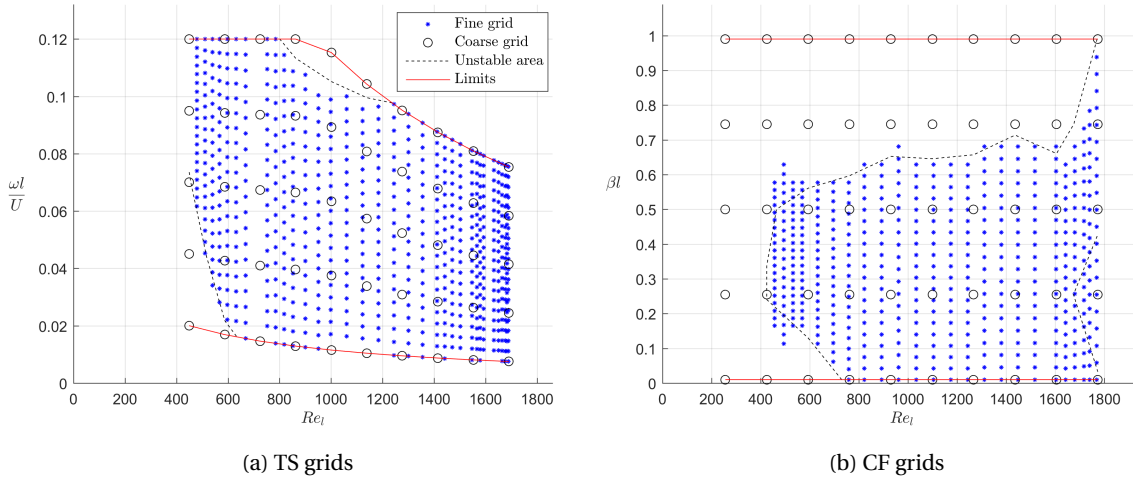


Figure 3.8: Stability solver grid structure to discretize the parameter space

The grid is limited along ω and β using two lines, illustrated by the red continuous lines in figure 3.8. The variation of β is constrained between 0.01 and 1 by setting constant bounds, while the limits in ω are refined by using curves proportional to $1/Re_l$. A correlation with a physical limitation of the disturbance waves was postulated. In principle, the wavelength of disturbances at low frequencies would be too large to be present within a small shear layer. As such, the boundary layer thickness at each Re_l should be larger than a certain threshold in ω . This correlation was found to not be robust enough to encapsulate all unstable areas of the ω domain. The current limits are based on trends of the stability diagrams of several Falkner-Skan solutions, see section 2.6. The exact magnitudes were obtained by manual iteration over a wide range of conditions as seen in the creation of the surrogate model creation in section 3.7, for example.

3.5. N-factor

Integrating the amplifications according to equation 2.1 (repeated below for convenience) results into an N-curve. One matter of ambiguity is the direction of integration: Although all amplifications α_i are defined to be along the x-coordinate, it is possible to integrate along other paths [43]. Several alternatives are mean flow streamlines such as the inviscid streamline or the surface streamline, or along a direction defined by the stability solution. For example, integration along constant β , constant wave number $k = \sqrt{\alpha_r^2 + \beta^2}$, or maximum growth rate with respect to β : $\partial\alpha_i/\partial\beta$. Literature suggests different strategies per type of instability, which will produce different N-curves for the same local amplifications. Although such considerations are of interest for practical accuracy, it was decided to leave such matters outside the scope of this work. However, if the calculations of this tool are to be calibrated with experimental N-factors at some point in the future, it is critical to reconsider the integration method.

$$N(x) = - \int_{x_0}^x \alpha_i dx \quad (2.1)$$

3.5.1. N-curves

After evaluating the grids over the unstable range it is possible to evaluate the N-curves that will make up the N-factor envelope. To do so, the grid points are fitted with a third-order continuous surface to properly capture the curvature between grid points. However, this surface can not be extrapolated. The integration is

performed for constant physical frequency ω and β , which are mapped as straight lines through the origin on the normalized solver grids, see figure 3.9. The slopes of these lines are proportional to a physical frequency or wavelength for both TS and CF diagrams, as is derived in equations 3.1 and 3.2 by assuming a constant factor F or B and implementing the definitions from equation 2.18 [44].

$$\bar{\omega} = F \cdot Re_l \rightarrow \omega \frac{l}{U_e} = F \cdot \frac{lU}{\nu} \rightarrow F = \omega \frac{\nu}{U^2} \quad (3.1)$$

$$\bar{\beta} = B \cdot Re_l \rightarrow \beta l = B \cdot \frac{lU}{\nu} \rightarrow B = \beta \frac{\nu}{U} \quad (3.2)$$

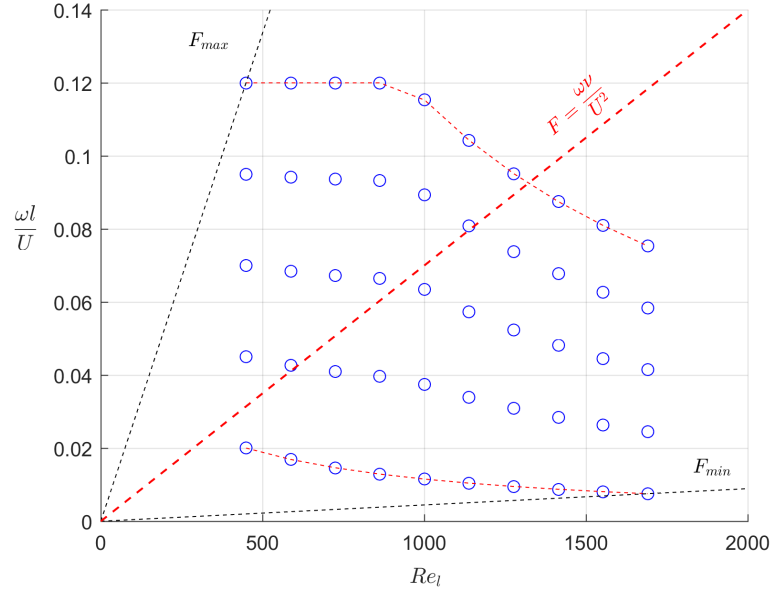


Figure 3.9: Example of an integration path of a physical frequency ω for TS instability N-curves

Under the assumption that the solver captured all unstable regions, a minimum and maximum frequency can be computed using the two lines passing through the borders points of the solution domain, indicated with F_{min} and F_{max} , respectively. Then, a large number of frequencies in between these limits are integrated using the fitted surface to properly capture every part of their envelope, resulting in figure 3.10. Interpolation of a grid is much faster than solving the stability problems per individual N-curve. It also allows for an arbitrary number of N-curves to be computed, creating a continuous *envelope* of the curves.

3.5.2. Envelope

The maximum N-factor per x -coordinate can be computed after integrating a sufficient number of N-curves. This N-factor envelope is the final result of the linear stability tool, given in figure 3.11. From this diagram, it is possible to estimate the point of transition for a given critical N-factor. For example, the upper surface boundary layer will experience TS induced transition around $x = 0.29$ at a critical N-factor of 7, as is indicated by the black dashed line. For the lower surface, transition due to CF instability can be expected around $x = 0.40$ if a critical N-factor of 3 is chosen. Although these critical N-factors have been chosen arbitrarily, CF instability induced transition in general occurs at lower N-factors than transition from TS instability [43].

The critical N-factor is dependent on several conditions of the airfoil that has been analyzed. For example, it is necessary to include effects of turbulence, sound, surface roughness and surface waviness. Receptivity of these sources of disturbance is another research topic on its own. For conceptual sizing, it is common to either refer to the freestream turbulence correlation of Mack [34], given by equation 4.4, or use results from literature. An N-factor is needed per type of instability, sometimes providing two points of transition, where the most upstream point will be the only physically relevant point for transition purposes.

Although the tool does not include interference effects between different types of instabilities, the N-factor envelopes can be combined and related to a $N_{TS} - N_{CF}$ chart, providing a single point of transition. An

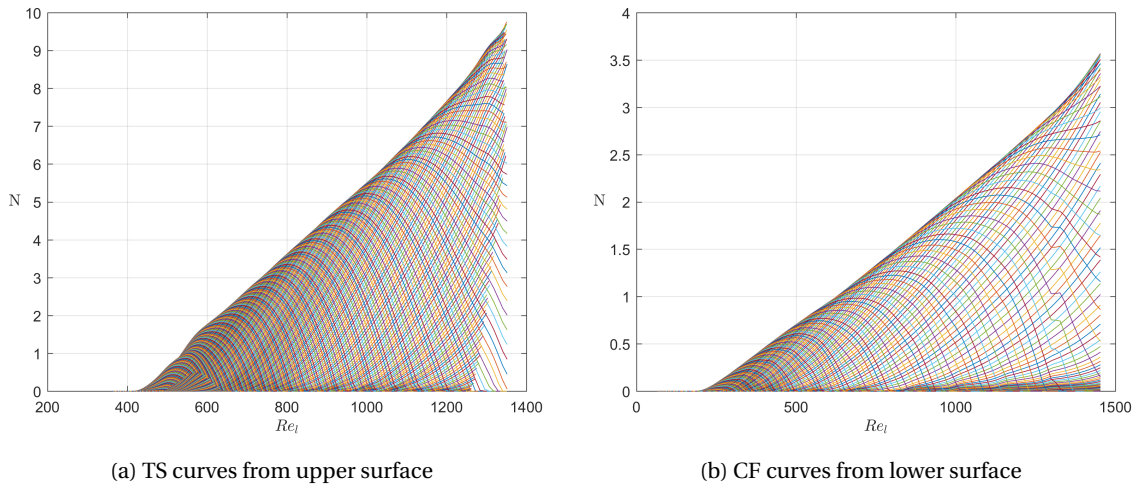


Figure 3.10: Collection of N-curves per type of stability

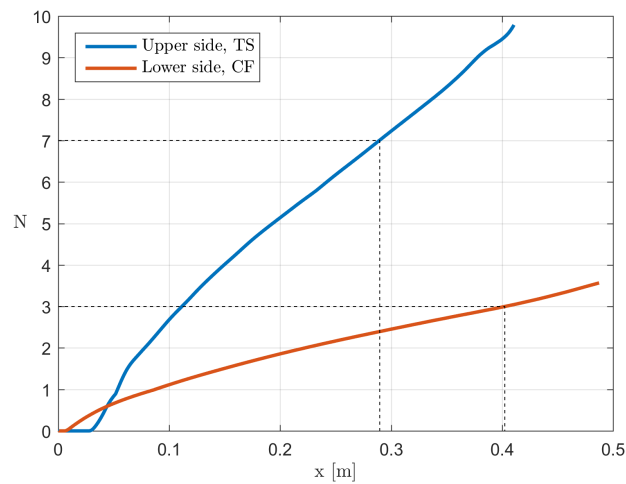


Figure 3.11: N-factor envelopes over the airfoil chord length for both surfaces

example of such a chart can be seen in figure 3.12. If the two N-factors obtained through the linear stability tool were to be combined, they define a curve in the $N_{TS}-N_{CF}$ space which is a function of x . Then a chart like this can be used to determine the transition point as the curve intersects the boundary between the laminar and turbulent regions of the $N_{TS}-N_{CF}$ space.

The combinations of N-factor values in figure 3.12 were obtained in the ELFIN I and II projects from both windtunnel (the lower N-factors in red) and flight experiments (outer points in blue) [43]. These calibration data were created by combining the measured transition points from experiments with computed N-curve envelopes to determine the critical N-factor. For several measurements, the uncertainty of the calibration data has been included as square regions instead of points. These results show that the assumption of non-interaction between the two types of instability is not always true. Scatter of the data makes design unreliable if calculations cannot be properly calibrated.

3.6. Transition

The process described in this chapter can be repeated for identical conditions, but at different angles of attack. Changing the angle of attack produces a new pressure distribution and will significantly alter the transition point. To illustrate this effect, the tool is executed for a range of angles of attack, while all other conditions as were given in table 3.1 are kept constant.

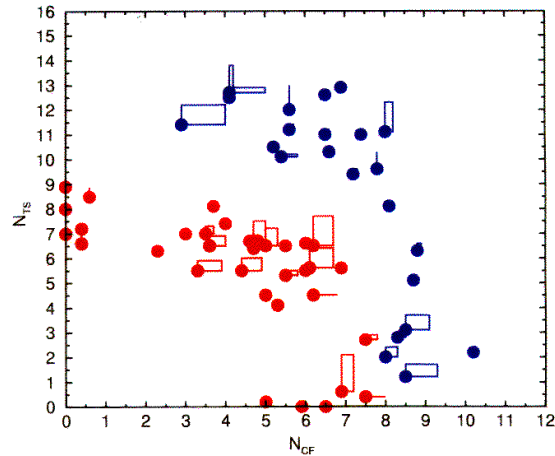


Figure 3.12: $N_{TS} - N_{CF}$ diagram constructed from the ELFIN projects [43]

3.6.1. Setup

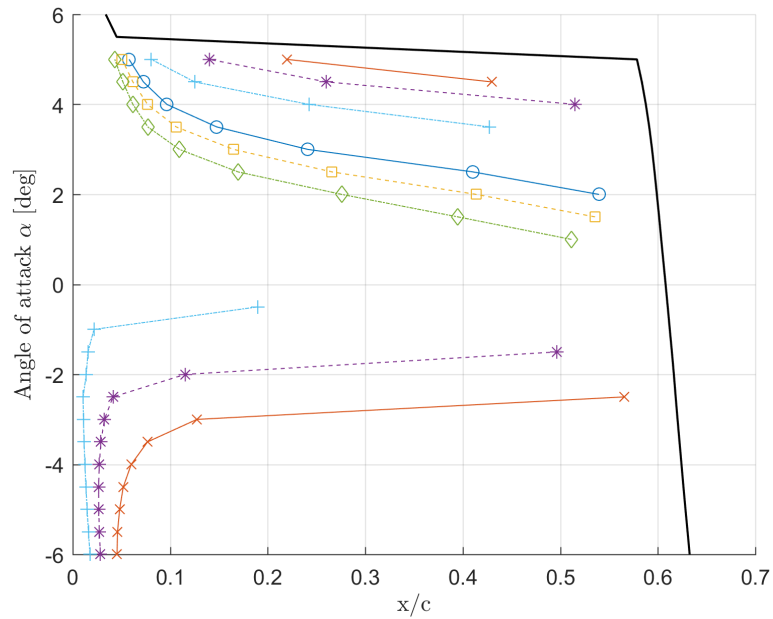
In figure 3.13 a *polar* of transition points is shown for both sides of the HSNLF airfoil. The N-curve envelopes per angle of attack have been intercepted with three different critical N-factors per type of instability, namely $N_{crit} = 9, 7$ and 5 for TS and $N_{crit} = 5, 3$ and 1 for CF. As such, there are three different transition *fronts* that moves upstream with decreasing critical N-factor. The legend in subfigure 3.13b indicates the type of instability and their respective critical N-factors in both figures.

The tool predicts early laminar separation at angles of attack of $\alpha \geq 5.5$ on the upper and $\alpha \leq 3$ on the lower surface. This is shown by the bold black line in both figures. The tool is not capable of solving a laminar boundary layer after separation. If no transition is predicted before laminar separation, these points are not drawn in the figures. For example, on both sides at $\alpha = 0$ it can be observed that transition does not occur before laminar separation.

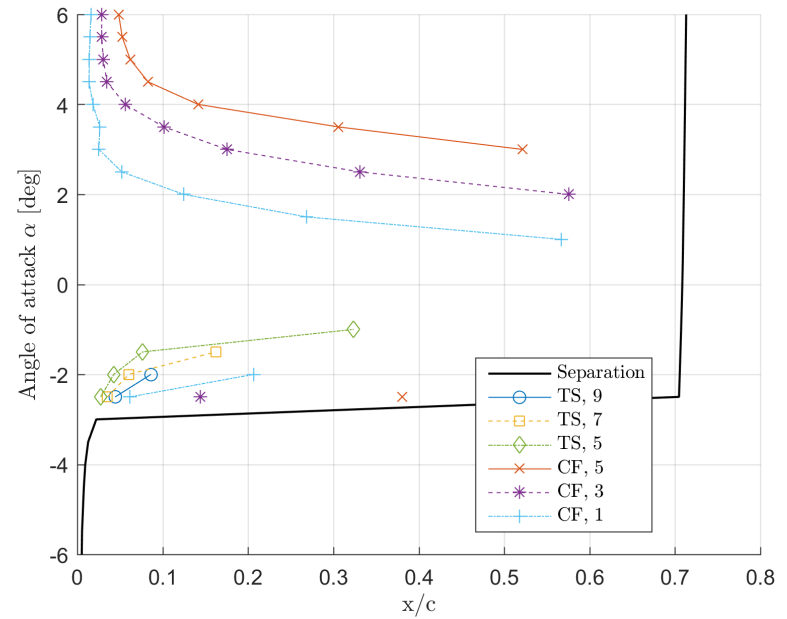
3.6.2. Observations

It is noteworthy that transition from TS instability only occurs at high α on the upper surface and at low α on the lower surface. This is a result of the negative (favorable) pressure gradient that stabilizes the TS waves if a surface of the airfoil is directed towards the flow. However, the pressure gradient will cause crossflow instability in the boundary layer of swept wings, which is visible on both surfaces. On the upper surface, CF becomes the dominant source of transition at $\alpha < 0$. Similarly on the lower surface, at roughly $\alpha > 0$. Small hints of crossflow due to positive (adverse) pressure gradients are also possible if the critical N-factor is lowered sufficiently, but this type of transition only seems to occur aft of the TS type of transition at all observed cases.

For the conditions of this case, these results show the feasibility of the HSNLF airfoil on swept wings at a low Reynolds number. Such a conclusion is of high importance for the feasible aircraft design space in which this airfoil could successfully be applied. This information, if properly extrapolated or even expanded with more relevant parameters, can be utilized to estimate transition on all lifting surfaces of an aircraft that are build with this airfoil. Moreover, the high fidelity transition prediction calculations are then used as fast design methods that would be ideally suited for preliminary aircraft design.



(a) Upper surface



(b) Lower surface

Figure 3.13: Transition locations on both surfaces of both types of instability for three different critical N-factors

3.7. Surrogate model

As was suggested in the structure of the thesis in chapter 1, a connection between the linear stability tool and modeling of aircraft has to be created. A balance between fidelity and computational speed has to be found, for which a surrogate modeling approach is the most likely candidate. The process described in this chapter, used to create four N-curves (i.e. two surfaces with two types of instabilities) can be performed over a range of geometric and flow properties. A result from the tool would be stored per combination of variables, forming a database or surrogate model. Interpolating this database for an arbitrary set of variables will approximate the result of the actual tool almost instantaneously. One surrogate model of the HSNLF airfoil has been constructed and will be detailed below.

3.7.1. Variables

To create the surrogate model, a choice has to be made regarding the input variables and their domain, plus the output variable of the tool to be stored. For the output it was decided to use the N-curves themselves and not rely on the amplification rates. This reduced the amount of data to be stored and removed interpolation problems in the arbitrary parameter domain (the Reynolds versus β/ω space of the solver). The input variables which influence the N-curves are numerous and a selection has to be made. It was decided to create a surrogate model for one airfoil shape, but with varying freestream Reynolds number, thickness-to-chord ratio, sweep angle, and angle of attack, see figure 3.14.

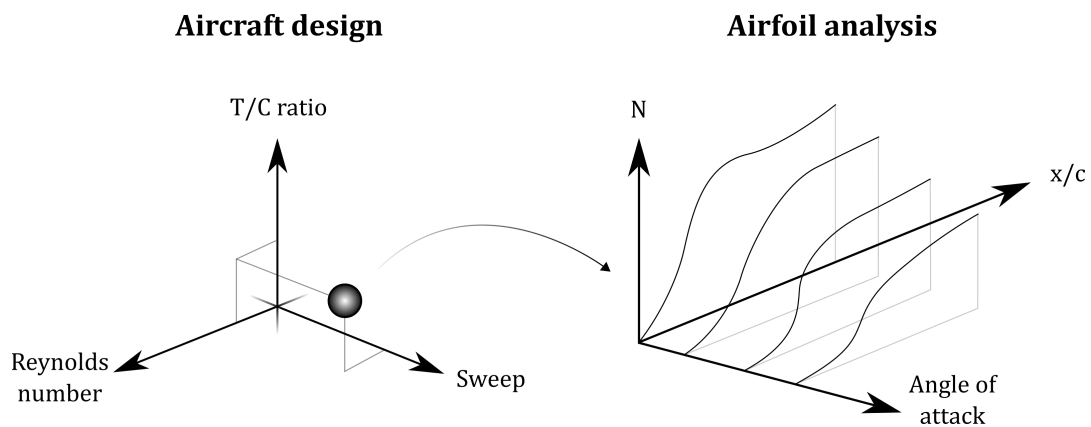


Figure 3.14: Surrogate model parameters

These four variables make it possible to model a wing in different freestream conditions, with a planform build from arbitrary chord lengths and sweep angles, composed of a single airfoil section with a different twist and thickness-to-chord value per span-wise station. Therefore, this surrogate model can be used for *any* lifting surface as long as it uses the same airfoil as basis.

3.7.2. Discretization

The surrogate model is composed of four databases for the upper or lower side and either TS or CF instability. Each of these is a five-dimensional matrix of data with the respective dimensions being the Reynolds number, thickness-to-chord ratio, sweep angle, angle of attack and chord-wise coordinate x/c . The data per matrix element are the N-curve envelope magnitude. As interpolation is a fast process, the computations involving this five-dimensional surrogate model are ideal for conceptual design. The complication lays in the time required to create the database itself. The number of dimensions causes the computational time to grow exponentially with each additional discretization. Considering the known performance of the HSNLF airfoil, it was decided to define the domains of the four operational parameters as the following:

1. **Reynolds:** 2, 5, 10 and 20 million.
2. **Thickness-to-chord:** 0.08, 0.11, 0.13 and 0.16 (original is 0.136)
3. **Sweep:** 15, 25, 30 and 40 degrees
4. **Angle of attack:** -2 to 4 degrees, in steps of 1 degree, hence 7 points.

The surrogate method has only been functional while the interpolation method is linear. Also, for sake of robustness, the model is not extrapolated outside the domain of these variables. Therefore, it is important to

both select values in the vicinity of the most nominal operational value but also cover the plausible parameter range. The number of linear stability tool evaluations can be found by multiplying the length of each dimension, summing to in 448 evaluations in total. On a local computer, this equated to approximately 18 hours of computational time utilizing parallel processing of the stability calculations. The pressure distributions have been generated by Xfoil, which might influence the accuracy of the calculations. Therefore, the results are stored as a set of 64 figures that were checked for a feasible solution.

3.7.3. Results

To illustrate the surrogate model, an arbitrary wing planform can be inserted to see the extend of laminar flow. The surrogate model of the HSNLF airfoil is used on the Embraer Phenom 300 business jet created by the Initiator, which will be discussed in further detail in chapter 4, see figure 3.15. The N-factors have been interpolated from the surrogate model per spanwise station to obtain a contour of N-factors in cruise conditions. The quarter-chord sweep line is used as input, while the wing is untwisted and under an incidence angle of 1 degree. The thickness-to-chord ratios were chosen to be 0.14, 0.12 and 0.10 at the root, kink and tip, respectively. The color scale of these contours have been chosen to become white above the critical Reynolds number of TS and CF instabilities, set to 9 and 5 respectively. Laminar separation is shown as black, similar to an N-factor of zero. In addition, the fuselage outline has been included to only show the exposed wing, while the winglets of the Phenom 300 are excluded from this test case.

The example illustrates the presence of strong crossflow instabilities as a consequence of the sweep angle, causing the entire wing to be turbulent. It is obvious that proper laminar design would require a different planform or operating conditions if the HSNLF airfoil were to be used. Considering that the HSNLF airfoil was designed for an unswept business jet, optimizing the airfoil for increased laminar flow is in this case a worthwhile investigation. The limitation of the 2.5 dimensional model becomes apparent in the vicinity of the kink of the wing: The kink imposes a jump in the quarter-chord sweep angle and thereby a jump in the N-factors. A solution would be to use the leading edge sweep angle, which is continuous, or to define a function to smoothly transfer between the sweep angles.

If we apply the HSNLF airfoil to the Learjet 45 wing using the same methodology, we obtain quite a different result, see figure 3.16. The model is also evaluated at the quarter-chord sweep angle and the wing is untwisted, incidence of 1 degree with thickness-to-chord ratios of 0.12 and 0.10 at the root and tip, respectively. The lower sweep angle reduces the CF instabilities significantly, making TS instability the primary cause of transition. A significant laminar region can be obtained under these conditions on both the upper surface and the outboard part of the lower surface.

3.7.4. Utility

Considering the speed with which a wing can be evaluated for the extend of laminar flow, the surrogate model is very promising for conceptual design. The downside of being constrained to a single airfoil is acceptable in this design phase, but does require the creation of additional surrogate models of airfoils that are more resistant to CF instability at higher sweep angles.

The linear stability tool is computationally expensive but highly accurate and the surrogate model sacrifices its accuracy slightly to practically remove the computational time. As such, the linear stability tool is applicable for detailed analysis and optimizations, while the surrogate model is suited for aircraft design. Using the surrogate model of a single airfoil, it is likely that a conceptual wing can be designed by optimization in a relatively short period of time that would well approximate the final result of a detailed analysis.

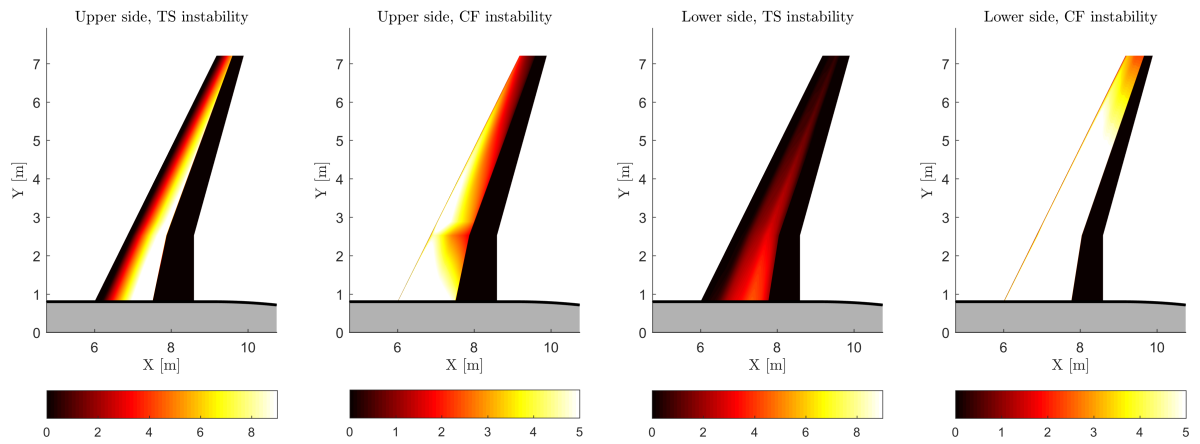


Figure 3.15: N-factor contours of the Embraer Phenom 300 wing in cruise flight using the HSNLF airfoil

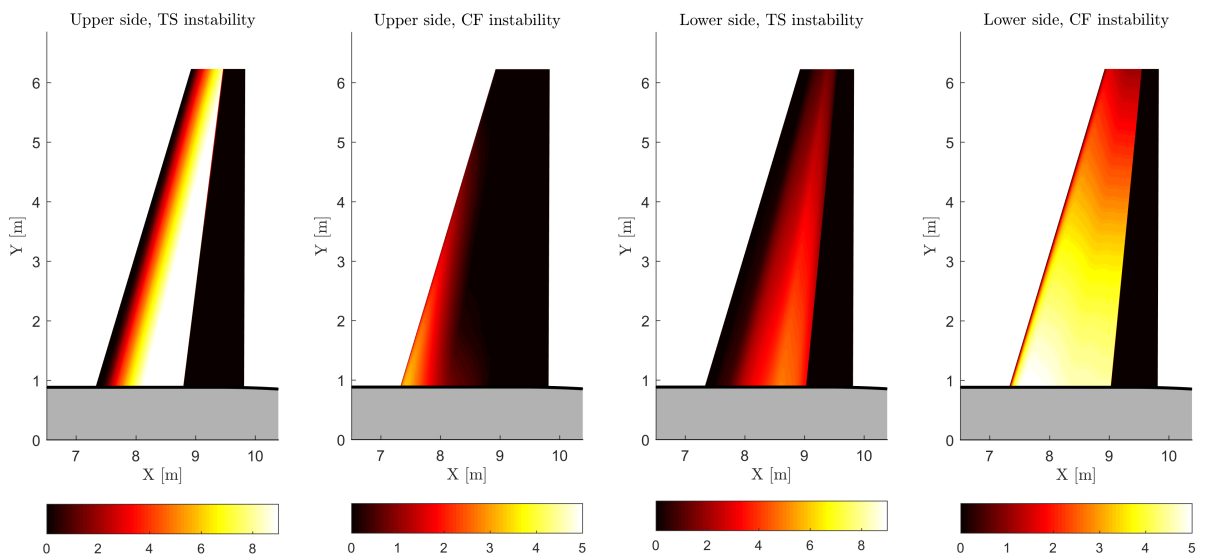


Figure 3.16: N-factor contours of the Learjet 45 wing in cruise flight using the HSNLF airfoil

4

Aircraft design

Drag reduction by application of laminar flow technology on the aircraft design has been thoroughly proven in literature. To quantify the influence of this reduction on the complete aircraft, the conceptual design tool *Initiator* is used to compare differences in aircraft performance and sizing in comparison to 'turbulent' benchmarks. This chapter will describe the modifications made to the program to allow for business jet design, plus the creation of several baseline aircraft. Also, the impact of laminar flow and the snowball effect of its drag reduction on several key performance indicators are discussed.

Besides the activities related to business jet design, the Initiator was overhauled to increase robustness, accuracy and feasibility of all aircraft. As it is a tool in continuous development by the faculty staff and the graduate students, the modifications described in this section were included from one version onward¹. An overview of the modifications not directly related to the thesis topic can be found in Appendix B. The principle of design convergence that is used in the Initiator is explained in this Appendix as well.

4.1. Fuselage design

As the primary component of the aircraft in terms of aircraft weight and size, the fuselage is crucial for the overall accuracy of the model within Initiator. Many empirical sizing methods include its dimensions and the internal distribution of mass is obviously critical to most analyses and design routines. Also, feasibility of the fuselage design to meet its requirements includes a match between external and internal dimensions of the fuselage. The original design methods within the Initiator used database predictions and constants to size the fuselage and distribute its weight. This coarse *outside-in* design approach suffered from two major drawbacks: No design knowledge was applied in sizing the fuselage to fit the aircraft requirements and the internal seating layout was unknown, heavily influencing the accuracy of center-of-gravity locations and shifts.

To remedy these large shortcomings, it was decided to implement an *inside-out* design approach, in which the cabin is defined by the class seating distribution, seat dimensions, passenger requirements, etc. The cabin dimensions are then used to determine the external fuselage dimensions. This approach also makes it possible to include new design criteria, increasing the fidelity of the fuselage model within the Initiator. The parametrization of the fuselage and the process of calculating the external dimensions from internal dimensions will be discussed below. To minimize the changes required throughout the Initiator, the output structure of the *modules*, the subdivisions of the Initiator, were kept the same as the original structure, which was last modified by Kristian Schmidt [45].

4.1.1. Cabin design

The main element of the inside-out design approach is a design method to determine the layout of the passenger cabin. Seats, galleys, lavatories and emergency exits will need to be placed according to regulations and requirements. Within the Initiator, two versions of such a design method have been build so far [46, 47]. These either suffered from lack of accuracy or non-converged results. With only few seats, business jets are more sensitive to these problems and therefore a new methodology was required. The current implementation uses an iterative scheme to converge on a feasible design regarding seat- and exit placement,

¹The Initiator version that includes this thesis work is v2.9.

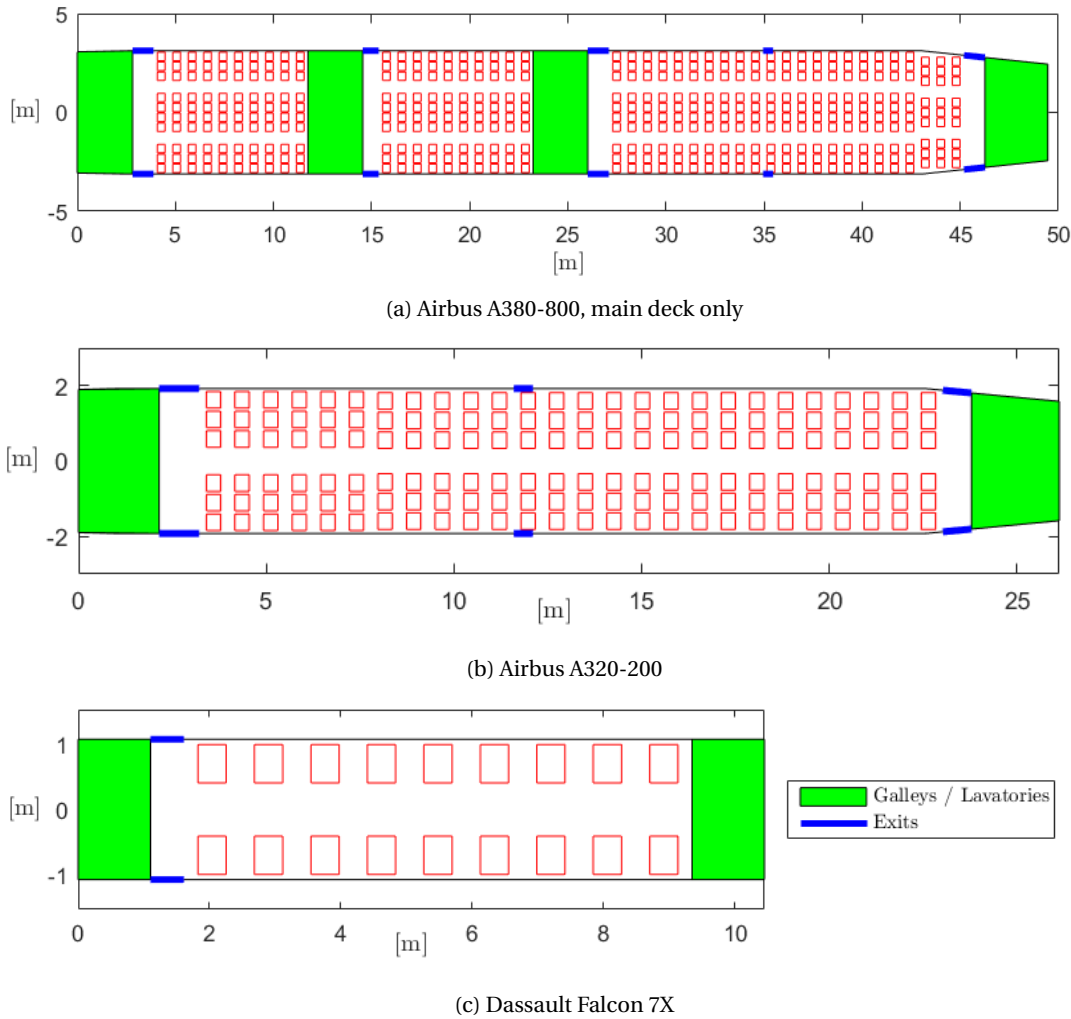


Figure 4.1: Cabin layouts generated for several reference aircraft

and a consistent design regarding cabin length and front and rear cabin tapering. These last elements define the outer planform of the cabin. Tapering is by definition an outside-in requirement and is determined in a second iterative loop that includes the nose and tail definitions. Without tapering, the fuselage length was often underestimated when reproducing highly tapered cabins such as the Airbus A340 and the Boeing 747 main decks. As such, this addition has proved to be crucial in accurate aircraft length (and thereby weight) predictions. The output of the cabin design calculation for some reference aircraft can be seen in figure 4.1. The cabin layout for multi-deck aircraft is obtained by solving different cabins separately and stacking the geometry at the correct longitudinal station.

The cabin layout is dependent on aisle requirements (the seating arrangement along a row of seats), emergency exit placing and the external tapering of the two ends of the cabin. It is build up by selecting the longitudinal stations of all emergency exits a priori, followed by the front-to-back placement of individual seats and galley and lavatory blocks. If insufficient length is available, the program predicts a feasible lengths and iterates. If the cabin was assumed too long, the length is similarly shortened until the design converges. An important consideration in this process is the discontinuous influence of seat placement on the cabin length, as adding or removing a row of seats causes a jump in length. This is especially troublesome if seats are removed because of tapering. Surprisingly, it was found that the shortest feasible cabin length for fixed tapering angles most likely includes some unused space: Further decreasing the cabin length to remove this unused space would shift the tapering forwards and remove an additional seat, hence making the design unfeasible.

4.1.2. Inside-out optimization

To allow for an inside-out process, the internal cabin geometry of one or more cabins has to be enveloped by an external hull. Therefore, a method was needed to fit two-dimensional sections around the cabins and any cargo containers. The sections are created at every unique longitudinal station, using three circular arcs with different radii for pressurization loads and with tangent (first-order) continuity at their connecting points. This definition was already used in the Initiator and reusing it would reduce the workload of revising other code [45]. The design of these sections depends on many considerations, such as structural loading, pressurization, aerodynamic drag, etc. A simple but effective solution was found by creating an *inside-out optimization* (IOO) scheme to vary the design parameters of a section to minimize the sectional area while encircling all internal components. The three parameters were chosen to be the two hull points at the symmetry plane of the aircraft, plus the width of the (main) cabin.

Formally, the objective function of the newly created optimization is the cross-sectional area with the constraints being the cross-sectional cabin and cargo outlines. An example of the optimization input can be seen in figure 4.2. The parameters to specify the internal dimensions of the cabin and cargo containers are shown on the right. On the left, several fixed margins for the spacing between cabins or cargo bays are included. Also, all constraint points for the IOO are shown by a set of dots connected by a bold line. The figure illustrates the flexibility of this method to incorporate multiple cabins or other components. Adding additional components only requires extra points in the constraint function, which can include an arbitrary number of points.

Some aircraft have non-circular or eccentric fuselage cross-sections, such as the Airbus A380 and Boeing 747. Also, the Initiator is intended to model both conventional and unconventional aircraft, such as BWBs and has to be flexible to deal with varying fuselage concepts. Therefore, the inside-out optimization allows for an eccentricity of the sections by constraining the ratio between the radii of all arcs. That is, a circular section would have a constraint to force all radii to be identical, or have a ratio equal to 1, while BWB sections can have ratios lower than 1. The exact value is dependent on the type of aircraft or can be enforced by the user through the input file, if necessary.

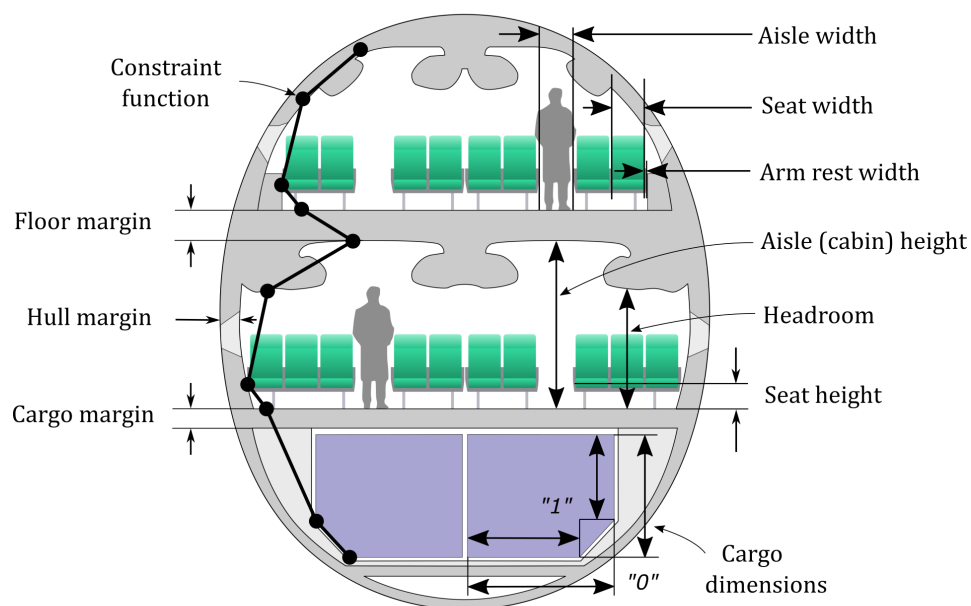


Figure 4.2: Inside-out optimization parameters and constraints applied to an Airbus A380 [48]

4.1.3. External geometry

The sections created by the optimization are concatenated to form the fuselage external geometry around the cabin and cargo containers. However, the geometry in front and behind the cabins and cargo holds has no internal constraint and can not be created with the inside-out optimization. The nose and tail geometries are defined separately from the center by drawing the side-view profiles of the fuselage. The full three-

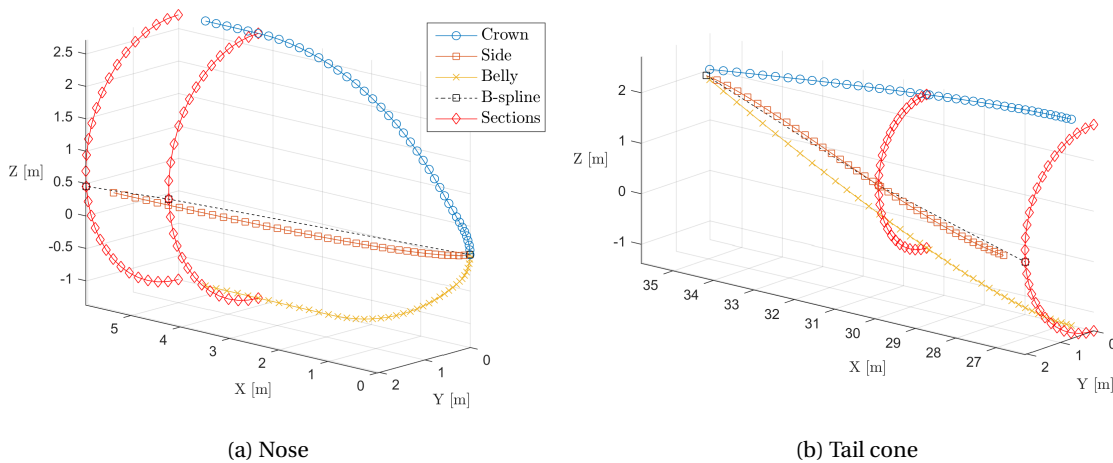


Figure 4.3: External geometry creation of the Airbus A320-200

dimensional geometry is then created by scaling the ends of the center geometry with the outline of the nose and tail, see figure 4.3. Several functions have been created within the Initiator to interpolate and manipulate geometry in three-dimensional space for this purpose. For example, the absence of a dedicated geometry handling back-end of Matlab required the manual calculation of a B-spline to fit the hull shape and internal cabin sections. Also, the mesh or grid of the hull itself had to be build using the vector arrays in figure 4.3, for which a curve-to-curve surface generation code was created, in a manner similar to most lofting functions in computer-aided design programs.

4.1.4. Cargo

The cargo containers have to be selected to meet the top-level payload requirements. Using a list of known container types and the payload requirements of the aircraft, a group of solutions exist to carry the required volume or mass. To decide on an optimal solution, the fuselage configurator cycles through all container options and checks whether the container type can carry all required cargo. If so, that container is labeled as feasible. The dimensions of the cargo bay are constrained by the the top-down planform of the cabin above the cargo bay, as shown in figure 4.1. That is, the layout of the containers can not be wider or longer than the cabin on top of it. Currently, only one stack of containers is allowed. From all feasible container types, the fuselage sections are created using the inside-out optimization. The container option with the least cross-sectional area (or cumulative volume) is chosen as the final design of the fuselage.

In the absence of containers, as is the case for business jets, any payload not carried within the cabin is stored in a freight bay behind the cabin. In that case, it is not necessary to perform the cargo selection described in this paragraph. Instead, the freight bay is sized based on a bulk cargo packing density and a calculated internal tail volume. The internal volume includes a margin with respect to the hull and a packaging efficiency fraction also used for normal bulk calculations. The space reserved for a freight bay is illustrated within the Initiator by a blue planform as shown in figure 4.4 for an Embraer Phenom 300.

4.1.5. Fuel tank

A final addition to the fuselage is to increase the fuel volume within the aircraft by placing a fuel tank in the fuselage. Such a fuel tank is placed if the volume of the wing fuel tanks is not sufficient for the mission range, and the user has chosen to implement a fuselage fuel tank. Similar to the freight bay, the tail volume is calculated to determine the length of the fuel tank. The tank is currently placed behind the freight bay, although it might be more beneficial to interchange the longitudinal position when considering the center of gravity location and shift during flight. The geometric implementation of the fuel tank can be seen in figure 4.4 as well. The yellow mesh shows the fuselage fuel tank, designed to obtain the required additional volume. Similar to the freight bay, the internal volume calculation is performed with a hull margin and a usable fuel volume fraction. As was discussed in chapter 1, the fuel tank of business jets is regularly placed in the wing-body fairing. Considering the absence of the fairing in the current Initiator version and the complexities of implementing it, this option was not considered for implementation.

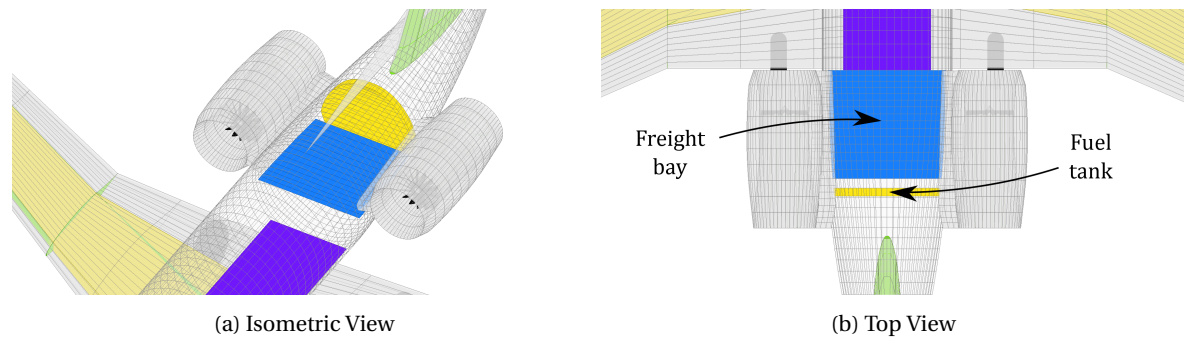


Figure 4.4: Geometry of freight bay and fuselage tank in an Embraer Phenom 300

4.2. Airfoil definition

Aerodynamic profiles or airfoils are used extensively for both the Initiator itself and the stability analyses discussed in chapters 2 and 3. Many airfoils are easily available from multiple sources on the internet. The conventional format in which airfoil profiles are defined is as a list of coordinates, sorted per side in a *dat* or *txt* file. The *Lednicer*² formatting includes the name of the airfoil, two integers to indicate the number of points per side, followed by the actual coordinates sorted in leading-to-trailing edge order (LE-TE). The upper surface is given separate from the lower surface. The *Selig*³ format includes the name and a list of coordinates sorted in a trailing-leading-trailing edge order (TE-LE-TE), with the inverted upper surface given first.

The Initiator has been programmed to operate in the structure used by Selig's formatting. Unfortunately, the format between data files is not consistent and in rare occasions there are not enough points to accurately model the profile. It was decided to implement a generic parsing routine within the Initiator to handle different file formats, plus a fitting and sampling routine to increase the number of points used for the airfoil definition. This increased the fidelity of any calculation involving the airfoil coordinates, those mostly being Xfoil and AVL, two aerodynamic solvers which are both used abundantly within the Initiator. The updated class definition is described in the UML diagram in figure 4.5. Properties (attributes) and methods (operations) are given separately. Originally, the class only included a routine to load the coordinates of an airfoil from the database. As such, only a name tag was used to indicate the sectional properties of a wing. This limitation required individual developers to produce their own code to manipulate and obtain airfoil properties. Therefore, the routines described below are included into the class along with precalculated values of camber, thickness (including thickness-to-chord ratio) and separate upper and lower surface distributions.

Airfoil::HSNLF_0213 (Geometry)

```

Name: 'HSNLF_0213'
Chord: 3.21 m
Twist: 0.15 deg
TcRatio: 0.14 [-]
Upper: real upper surface coordinates
Lower: real lower surface coordinates
Data: real TE-LE-TE coordinates
Shared: normalized distributions of
ordinate, upper, lower, camber, thickness
SourceData: normalized TE-LE-TE
coordinates
-----
area = area()
Data = loadAirfoil(Name)
Data = parseAirfoil(Data)
[Upper,Lower] = separateAirfoil(Data)
Shared = formatAirfoil(Upper,Lower)
[Upper,Lower,Shared,Data] =
resampleAirfoil(noPoints)
[CSTu,CSTl,zeta_u,zeta_l] =
airfoil2CST(noCST,Upper,Lower)
y = CST2side(CST,Xin,zeta)
figureHandle = plot()

```

Figure 4.5: Initiator airfoil class UML definition

4.2.1. Parsing

After loading a data file into Matlab, which is automated using the `importdata` command, a number of checks have to be performed on the numbers present in the file. At this point, the order of the data or the identity of the upper and lower surface are not known yet, which makes the following steps rather cumbersome. First, any remaining headers to indicate the number of points have to be removed. Second, the data is rotated and scaled to make sure the leading edge and trailing edge are located at the coordinates $(X, Y) = (0, 0)$ and $(1, 0)$, respectively.

²Named after Daniel Lednicer, Aeromechanical Solutions LLC

³Named after Michael Selig, Princeton University

An important exception has to be made for open (or blunt) trailing edges, in which the last points on the upper and lower surface are placed symmetrically around $(1,0)$. This is done by identifying the data point at the furthest X coordinate (i.e. the trailing edge) and temporarily excluding it from the data set. Then, the new trailing edge is tested whether it is at the same location or is offset in Y , see figure 4.6. This check indicates either a closed or open data set, because a closed data set would have an additional point at the same Y location. Open airfoils are modified at a later stage.

The index of the data point that separates the two sides of the airfoil is identified and labeled as the *split* index. This data point is commonly found close to the middle of the data set. The data is separated into an upper and lower surface using the split index and is reordered into Selig's continuous format (TE-LE-TE). Again, the inverted upper surface is given first, followed by the lower surface. The leading edge point at $(0,0)$ is included only once. Also, the X coordinates of both sides do not necessarily coincide, a result of the normalizing process described earlier. To have an airfoil definition in which these points coincide, the *Shared* property was created, which includes the thickness and camber distribution of the airfoil.

If the airfoil has an open or blunt trailing edge, the airfoil is closed by placing an additional data point at $(X, Y) = (1 + 10^{-6}, 0)$ on both sides. The incremental offset is necessary to have a monotonic increasing X coordinate, a requirement for the interpolation methods within Matlab. The change in chord length is considered small enough to be ignored. A closed format is needed for several operations of the Initiator relating to surface creation routines and geometry analyses. However, vortex methods such as Xfoil do *not* operate properly if this point is still present. Fortunately, the closing data point can be found easily by calculating the slopes of the upper (or lower) surface of the airfoils. Then, the first and last points of the data can be omitted from the panel code inputs. Another option is to add an additional property to the Airfoil class dedicated to write suitable inputs for programs such as Xfoil and AVL. This addition is left as future work.

4.2.2. Sampling

Sampling of the parsed airfoil is done by applying a cubic spline fit to the coordinates of either side of the airfoil, after they have been transformed to radial coordinates and the mean camber line has been subtracted. The mean camber line has to be subtracted to remove any cusps from the profile. This is a common feature on rear-loaded airfoils such as most supercritical airfoils. Removing the camber line converts the profile into a symmetric shape, indicating the thickness distribution. Transforming the thickness distribution from Cartesian to radial coordinates is guaranteed to have a monotonically increasing angle coordinate, suitable for a cubic spline fit.

Camber Two methods of sampling can be used: 1) fitting the camber and thickness distributions, or 2) fitting the two sides of the thickness distribution by simply subtracting an *approximation* of the camber line. As the camber line is not well defined before sampling, the first option is not suitable. Therefore, the approximated camber line is subtracted from both sides and later added to the fitted surfaces. This nullifies any errors in the lack of resolution of the camber line. Unfortunately, the camber line in the vicinity of the leading edge is prone to a numerical fluctuation. This is a result of the limited number of data points at the vertical asymptote of the leading edge, see the outline of the NACA 23012 airfoil as obtained from an online database in figure 4.7. Note, the axis are not of equal scale.

When sampling airfoils with multiple points in the vicinity of the leading edge, the camber line might alternate in sign. If such a camber line were to be subtracted from the sides, a smooth fit would not be possible. To prevent these problems, the camber line is scaled to not influence the sides close to the leading edge: It is scaled from 0% to 50% chord with a linearly increasing factor of 0 to 1, at these respective locations. The scaled camber line will remove any trailing edge cusps (as was the intention) but does not corrupt the leading edge. The two sides of the airfoil can now be confidently fitted with a cubic spline.

Radial fit Using a fit with radial coordinates is a common sampling method, as it has an increased point density at the leading and trailing edges. Moreover, the transformation is needed to cope with the leading edge singularity of infinite slope, but also has the advantage of being smoother than Cartesian coordinates, as can be seen in figure 4.8. The transformation from Cartesian to radial coordinates is done with equations

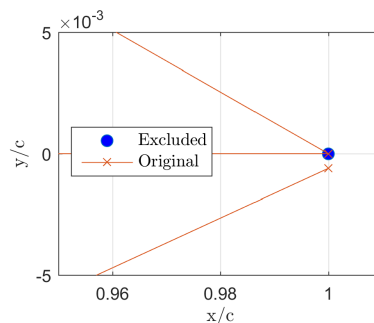


Figure 4.6: Closed airfoil check by excluding trailing edge from original airfoil data set

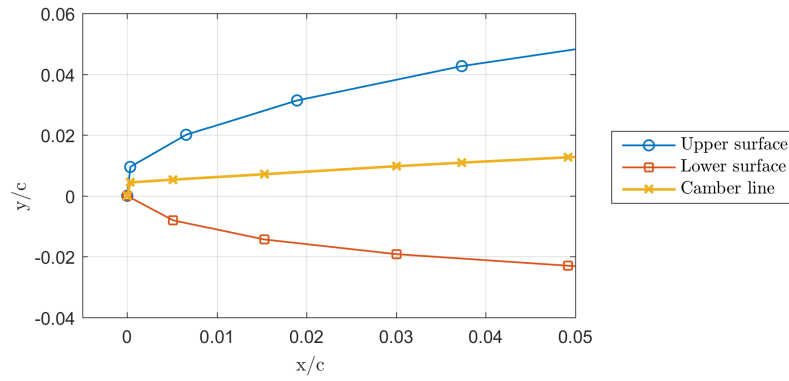


Figure 4.7: NACA 23012 airfoil camber line from linear interpolation

4.1 given below. From subfigure 4.8b, it is clear that the changes in the radius are more pronounced at the trailing edge, which is expected for the constant slope of a pointed end, see subfigure 4.8a. Shifting the origin of the radial transformation closer to the trailing edge will reduce this effect. The origin of the reference frame is placed by calculating the horizontal centroid of the area of the airfoil side. The x coordinate of the centroid is reversed (i.e. $1-x$) to move the origin closer to the trailing edge, while $y = 0$.

$$\text{shift} = 1 - \frac{\int_0^c yx dx}{\int_0^c y dx} \quad \text{scale} = 2 \cdot y_{max} \quad (4.1)$$

$$\text{radius} = \sqrt{\left(\frac{x}{c} - \text{shift}\right)^2 + \left(\frac{y}{c} \frac{1}{\text{scale}}\right)^2} \quad \theta = \tan^{-1}\left(\frac{x}{c} - \text{shift} / \frac{y}{c} \frac{1}{\text{scale}}\right)$$

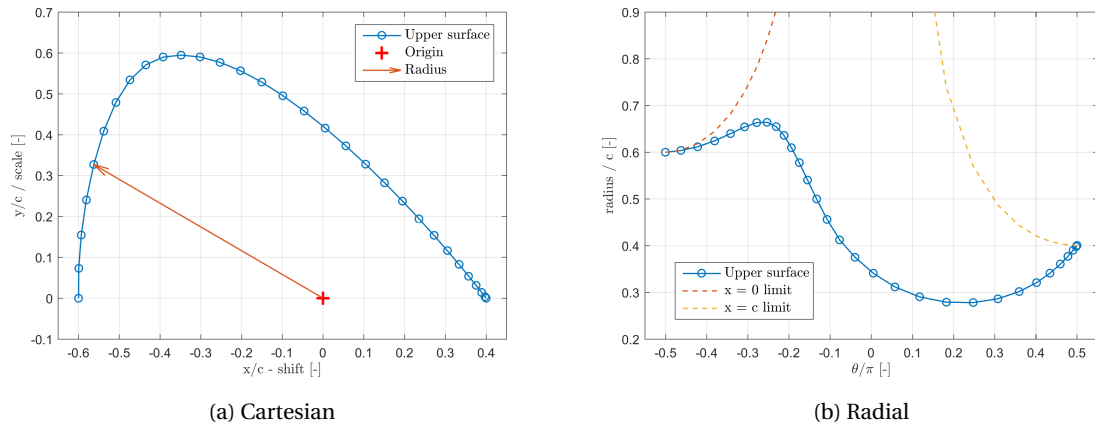


Figure 4.8: NACA 23012 airfoil coordinate transformation

Fitting the original points causes no error in the sampling process, as the fitted curve is forced to pass through all original points. The end conditions of the curve are important for the fitting accuracy. The leading edge gradient at $\theta = -\pi/2$ of the fit is set to zero. Zero gradient prevents a common problem of overestimating the radius close to the leading edge, possibly resulting into Cartesian coordinates beyond $x < 0$. There are limits of the radius at the leading and trailing edge when substituting $x = 0$ and $x = c$ into the radial transformation. These limits are shown in figure 4.8b by the dashed lines. Overshooting of these limits still occurs when sampling poorly defined airfoils such as the NACA 23012, see figure 4.9.

In such cases, a decision has to be made regarding the accuracy of the original data. The dilemma is between changing the original data points which originally caused the radii to extend beyond the leading edge, or selecting a new leading edge point. It was decided to keep the original points intact and change the

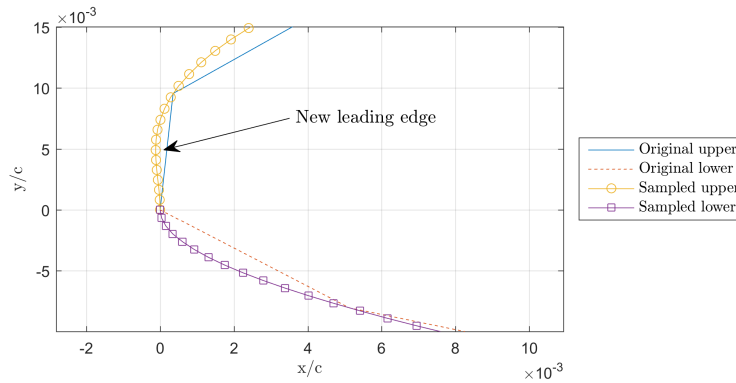


Figure 4.9: NACA 23012 airfoil detailed sampling result

definition of the leading edge. As such, the chord line of the original airfoil will be redefined, shifting any results related to literature given with respect to the angle of attack. Within the Initiator, the user is notified by this modification anytime it occurs.

Finally, the resampled data points are loaded back into the entire scheme described in this section. This is needed to normalize the airfoil and align the chord to the horizontal axis. The sampling is performed with a high number of points at first (300 per side) to resolve the leading edge, but is ultimately performed with a reasonable number of points (60 per side, defined by a setting). The last samples are the data points found throughout the Initiator.

4.2.3. Parametrization

In addition to the sampling process of the previous section, optimization schemes often require a reduction of variables. A commonly used method is the Class-function Shape-function Transformation (CST) [49]. It is ideal to significantly reduce the number of design variables of an airfoil, but is limited in its accuracy: Such airfoils were observed to often exhibit a some degree of waviness, detrimental to the accuracy of viscid aerodynamic calculations, but suitable for fast inviscid optimization schemes. This is an expected result from a reduction of variables, but can be easily overlooked when manually inspecting the reproduced profile shape. Fitting the aforementioned HSNLF airfoil with a curve defined by five CST parameters results in the errors shown in figure 4.10. As can be seen, the error fluctuates in a periodic fashion.

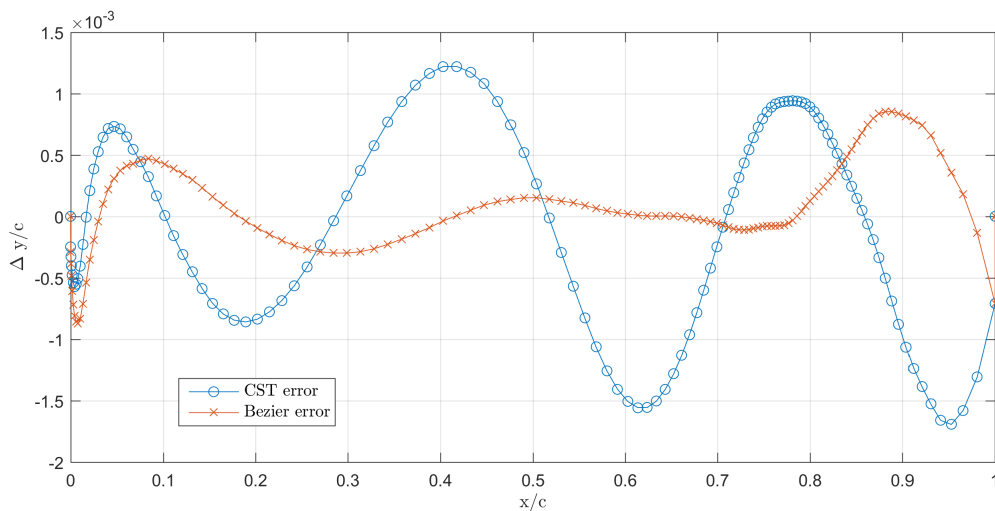


Figure 4.10: Errors when fitting an airfoil using CST or Bezier splines using 5 degrees of freedom

Obtaining CST coefficients to represent an arbitrary profile is not a straightforward procedure, as it involves an optimization procedure to fit the required number of coefficients to the profile⁴. Fortunately, transforming a profile defined with CST coefficients into Cartesian coordinates is a simple process of reversing the used transformation. To generalize the use of CST parametrization within the Initiator, both these processes have been implemented in two routines accessible from any point within the program.

In addition to the CST parametrization method, an airfoil fitting procedure using Bezier splines has been constructed. The control points of the Bezier spline are allowed to move throughout the Cartesian space which means that each point has two degrees of freedom. The exceptions are the horizontal movement of the control point defining the leading edge radius, plus the points at the leading edge and trailing edge themselves. It was found that this method reproduced the airfoils with a smaller mean error for the same number of variables, as can be seen in figure 4.10.

4.3. Wing definition

Simultaneously with the airfoil revisions described in the previous section, the wing class definition of the Initiator had to be modified. The object-oriented framework of the Initiator was used to make the wing class properties dependent on these sectional properties, with a feedback mechanism in case the wing is modified (change in chord leads to a differently scaled airfoil, for example). As such, the wing and airfoils are always consistent and can be queried and modified (known as `get` and `set` in Matlab) on both classes without conflicts. This is illustrated in figure 4.11, where allocation of Wing variables changes the local Airfoil sections whenever a dependent property is modified. These dependent properties are the *root chord length* and distributions of *taper*, *thickness-to-chord ratio* and *twist*. If such a dependent property is queried, the associated values are obtained from the Airfoil objects, as they are no longer stored in the Wing object itself.

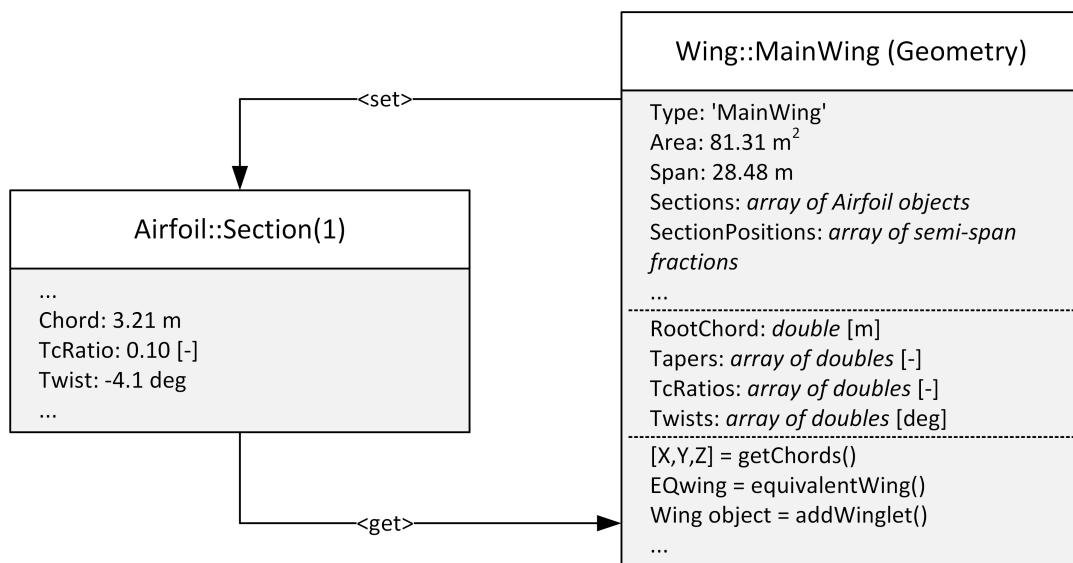


Figure 4.11: Wing class definition, including `get` and `set` relations with Airfoil class

The wing class is used to generate the main wings, vertical tails, horizontal tails, canards and *winglets*. Winglets were only implemented within Initiator for plotting purposes. However, the aerodynamic influence of the winglets is not negligible and has to be included when calculating the induced drag components of the drag polar within the Initiator. It was decided to not focus on detailed geometric design routines and simply insert usable parametrization of a winglet and increase functionality of the already existing geometric implementation by reusing the wing class definition of the Initiator. Computational implementation within AVL was not performed by the author and will not be discussed in further detail. The winglets are also assumed to be massless, which might cause a significant underprediction in the aircraft (roll) inertia determination. It is also unknown whether the aerodynamic loads are considered in the wing weight estimation.

⁴It should be noted that minimizing the error of a fit is sensitive to the weighting of each node. In general, high weighting on the leading edge is favorable if the error is computed by comparing the *y*-coordinates, to compensate for the vertical asymptote.

4.4. Drag polar

A large modification to the Initiator is the revision of the drag polar. The original drag polar used to determine the fuel burn was not capable of incorporating laminar flow and had to be revised. Below, the build-up of the drag polar is explained, followed by the modifications to determine the reduction of the zero-lift drag from laminar flow.

4.4.1. Drag breakdown

The drag within the Initiator is divided into three groups: Zero-lift drag, induced drag and wave drag:

$$C_D = C_{D_0} + C_{D_i} + C_{D_w} \quad (4.2)$$

The *Parasite Drag Estimation* (PDE) or the *Empirical Drag Estimation* (EDE) modules of the Initiator are used to compute the zero-lift drag coefficient. This was originally defined as a constant but needed to be expanded to be lift-coefficient dependent, mostly to also include fuselage lifting drag as it is not analytically calculated in the Initiator. The EDE is based on the work from Torenbeek [31] and was originally implemented by Warmenhoven [50]. It has been revised to use already computed Initiator data wherever they were available, instead of empirical values and approximations from the original work, such as fuselage side-view planform areas. In addition, the results have been separated into *vortex-induced* and *profile, interference* and *excrescence* contributions, so that only 'zero-lift' contributions are used, see figure 4.12 for an example related to the Gulfstream G650. Subfigure (a) illustrates the difference between the types of drag, while subfigure (b) shows the profile drag contributions of individual aircraft parts.

The PDE is based on Roskam's method, but only computes skin friction drag and fuselage lifting drag, thereby excluding excrescence and interference drag [27]. This will be discussed in detail in section 4.5.

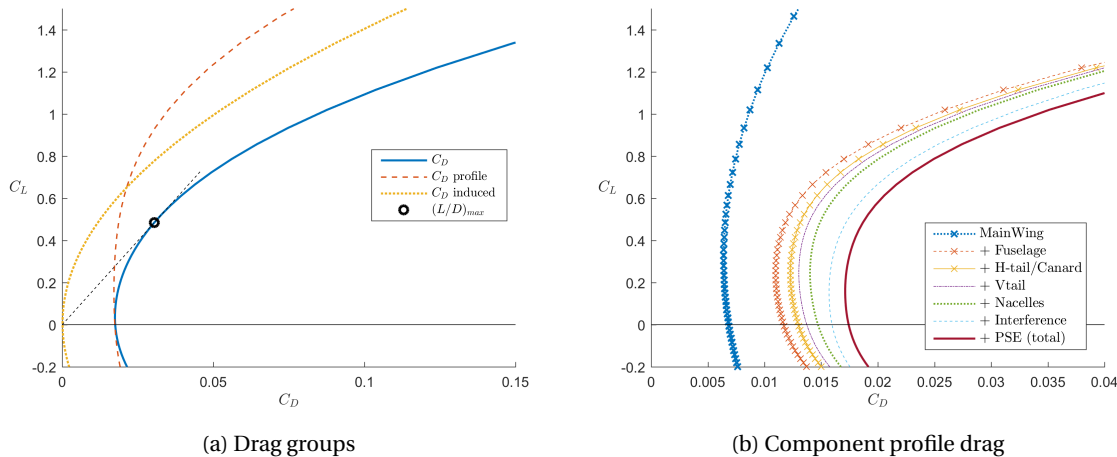


Figure 4.12: Empirical Drag Estimation drag polars of a G650

The lifting surface induced drag contributions are computed using AVL, including the trim drag over the center-of-gravity range expected during flight. The induced drag is computed for a limited number of lift coefficients and center of gravity locations. This reduces the computational time but the solution can still be expanded over the entire operating space. To do so, a quadratic fit is assumed for the induced plus trim drag distribution with respect to the lift coefficient, in accordance with equation 4.3. Within AVL, the induced drag is always calculated for trimmed conditions. While planar lifting surfaces would experience a purely quadratic trend, the total aircraft has linear and constant contributions related to the trim drag and non-planar design aspects, like wing twist. As such, for an aircraft lift coefficient of zero, there is still a positive induced drag component that is included using this analysis.

$$C_{D_i} = \frac{C_L^2}{\pi A e} + k_{trim} C_L + C_{D_i, C_L=0} \quad (4.3)$$

Finally, wave drag is computed using the longitudinal cross-sectional area distribution and is assumed to be constant with the lift coefficient. Unfortunately, the calculation could not properly resolve several geometry intersections to compute the cross-sectional area and therefore was not used. Instead, the C_{D_w} is set to a

Mach number and lift coefficient independent increment of 5 drag counts. It is expected that keeping this coefficient constant will alter the fuel burn during out-of-cruise flight phases, in which different lift coefficients and Mach numbers from the cruise condition are common. However, this is assumed to be negligible.

4.4.2. Drag module

The sum of all drag contributions is stored within the *Drag Module* of the Initiator. The drag polars are predominantly used within the *Mission Analysis Module*, where the fuel burn is calculated using a time-integration of all sizing missions. There, the Drag Module returns a total drag coefficient when queried with a lift coefficient. Also, the center of gravity location at each point in time is provided to include trim drag variations. The drag polar shown in figure 4.13 is of a trimmed aircraft with the mean center of gravity location during the harmonic mission.

The conditions that are evaluated using AVL are indicated on the polar as purple circles. They correspond to the lift coefficients given to AVL as input. Drag from the deflection of flaps and extending the landing gear are incorporated as constant increments. No empirical or analytic method is included in the Initiator to compute these contributions. Fortunately, they only have a minor influence on the total fuel burn computed during the Mission Analysis, because the take-off and landing phase are relatively short when compared to the cruise phase.

To increase the speed of the Mission Analysis but keep the accuracy of the computations intact, the numerical data are stored in the Drag Module and interpolated on demand using a cubic spline fit. This fit is allowed to extrapolate beyond the pre-calculated range of lift coefficients to improve robustness, but is obviously no longer valid beyond the linear regime. Also, the polars for landing and take-off are not valid at low lift coefficients, although they are drawn to seemingly cover the entire lift coefficient envelope.

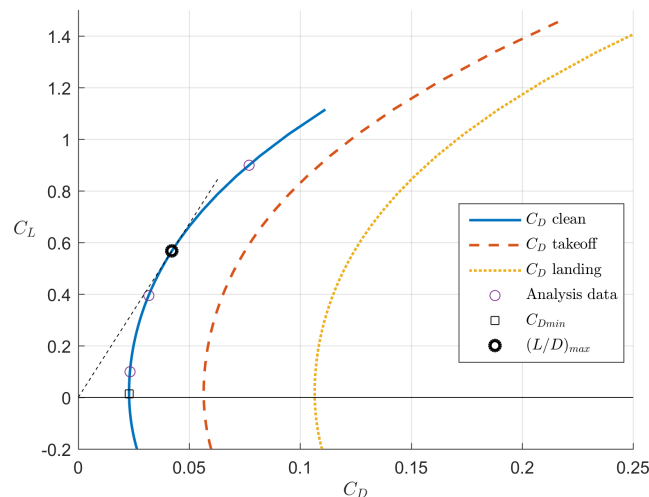


Figure 4.13: Drag Module drag polars of a G650

4.5. Parasite Drag Estimation

As mentioned before, the Parasite Drag Estimation produces the zero-lift drag coefficients by computing the skin friction drag on several components. Pylons, winglets and dorsal fins are excluded, but the main wing, fuselage, tail surfaces and nacelles are included in this calculation. In the original code it was assumed that the coefficients were not dependent on a change in lift coefficient (or angle of attack). On lifting surfaces, the laminar flow drag reduction only occurs at a small range in C_L , commonly known as a *drag bucket*. To incorporate this dependency on the lift coefficient, the PDE has been rewritten to produce skin friction predictions as a function of C_L , which will be explained below.

The new, *enhanced* implementation in the Initiator allows for both a detailed laminar flow analysis but also the assumption of lift independent zero-lift drag. This is toggled with the `PDEdetail` setting. The decision to modify the PDE module instead of the EDE module was made on the basis that the PDE is a physical method, albeit with empirical skin friction drag coefficient calculations. Laminar flow analyses with a de-

tailed transition point estimation will only modify the transition Reynolds number. This was originally set to a constant, so using a numerical computation for a more accurate value will not change the original method.

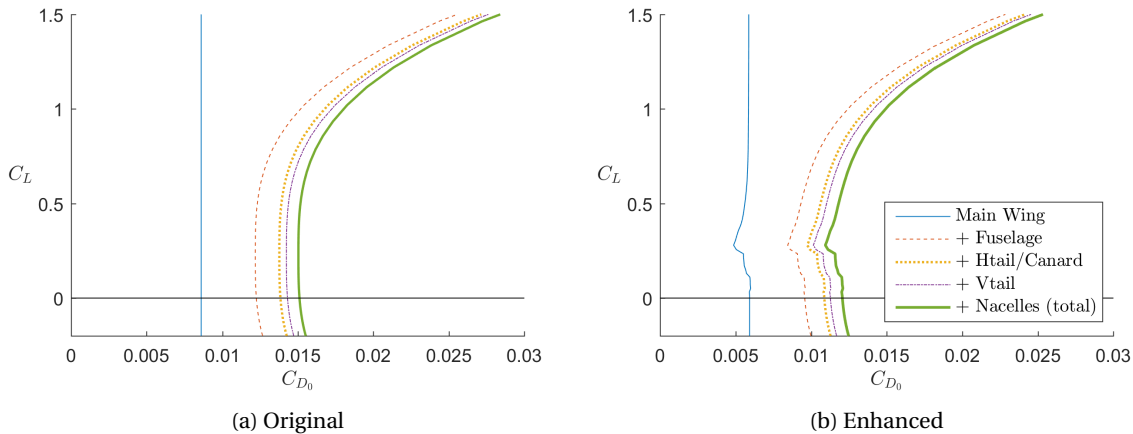


Figure 4.14: Parasite Drag Estimation drag polars of a G650

In figure 4.14a the zero-lift drag polar is given for the lift-independent (original) implementation. It is easy to observe that the drag is independent of the lift coefficient, with exception of the fuselage. The PDE includes the fuselage lifting drag because the induced drag obtained from AVL does not include fuselage lift, hence this contribution is computed here and is always angle-of-attack (or C_L) dependent. Different from the EDE, the PDE does not include interference and excrescence drag and also has a lower C_{D_0} for higher lift coefficients when compared to figure 4.12b, mostly due to the differences in computing the fuselage contribution. However, the zero-lift drag coefficient at $C_L = 0$ is almost identical when neglecting interference and excrescence drag, at approximately $C_{D_0} = 0.0155$.

4.5.1. Considerations

As input to the skin-friction drag estimation of the PDE module, an estimate for the position of transition is required. Different levels of fidelity or complexity are available to obtain this value.

The most simple method is a fixed Reynolds number for transition, as is used in the original code. It can be modified by changing the `ReTransition` setting. Another option to estimate the point of transition is by analyzing the airfoil geometry using fast tools such as Xfoil. This solver can be utilized as transition estimation by analyzing a profile representing the entire lifting surface, such as the outboard airfoil scaled to the mean aerodynamic chord (MAC). For more detail, evaluating transition at several span-wise locations a distribution will include spanwise variations in parameters such as Reynolds number, incidence angle (twist) and airfoil shape. However, Xfoil only computes transition based on two-dimensional flow. Therefore, it is limited to low sweep angles. In that case, the surrogate modeling approach discussed in section 3.7 can be used. The low computational time of the surrogate model is suitable for *in-the-loop* computations.

Considering the above, it was decided to implement the Xfoil routine for future use and determine sensitivity of laminar flow by modifying the `ReTransition` setting. The surrogate modeling approach was the preferred option for the evaluation of laminar flow, but the HSNLF airfoil was not found to be suited for highly swept wings (see section 3.7). To include surrogate modeling without having fully turbulent flow, first an airfoil has to be designed for laminar flow at higher sweep angles. Generating a surrogate model of this new airfoil will improve the accuracy of the Initiator results.

4.5.2. Xfoil implementation

The PDE has been extended by running a viscid analysis of Xfoil of the airfoil in the quarter chord sweep line orthogonal reference frame, based on the mean aerodynamic chord of the lifting surface. This process is performed for each wing part separately, producing results as shown in figure 4.15. From left to right, the subfigures show the drag polar, lift curve and transition point. In this analysis only the last figure is used. The results shown are for the HSNLF airfoil applied to the main wing of the G650 at a quarter chord sweep angle of 35.5° , with freestream conditions found at 12,500m altitude in ISA⁵ at a Mach number of 0.85. Transition

⁵International Standard Atmosphere

is assumed to occur at a critical N-factor of 9. The method to produce this graph is explained below.

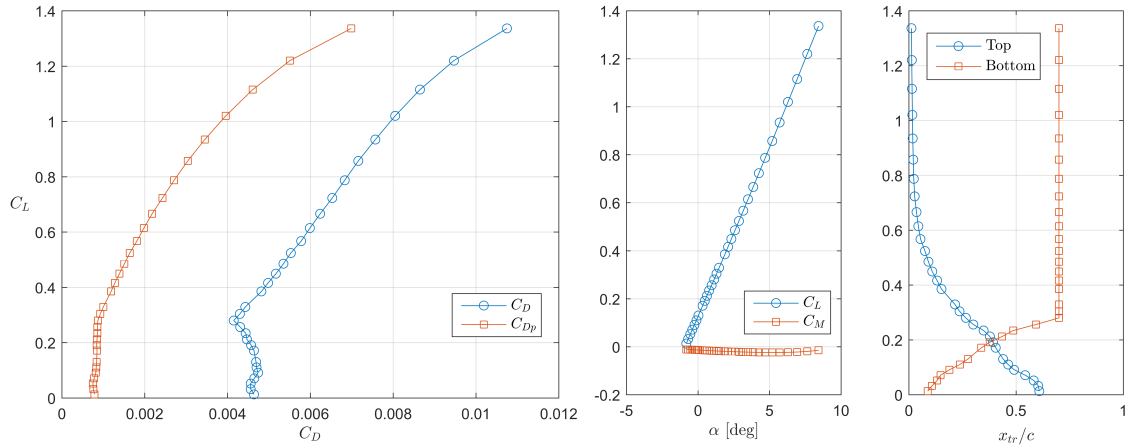


Figure 4.15: Xfoil analysis of HSNLF airfoil on the main wing of a G650

The Xfoil method is reasonably accurate for wings at moderate sweep angles, when Tollmien-Schlichting waves are the dominant cause for transition, see chapter 1. Above a certain sweep angle the transition is caused almost immediately due to cross-flow instability or attachment line contamination or transition if the airfoil is not specifically designed to compensate for these effects [6]. Therefore, a check is performed whether the wing quarter chord sweep angle exceeds (by default) 18° and will not perform the Xfoil analysis if so. The angle can be modified by changing the setting `CrossFlowSweepAngle`. In the example above, this setting was increased to 40° . In addition, transition is enforced at the hinge lines of any deployable or movable, i.e. flaps, slats, elevators, etc. The minimum point of forced transition is included in the Xfoil analysis, as can be seen by the constant transition point $x/c = 0.7$ on the bottom surface in figure 4.15 for $C_L > 0.3$.

After parsing and resampling the airfoil as discussed in section 4.2 the input files to Xfoil are written with an automated script. Such a script has been implemented in several sections of the Initiator, such as the Wing Refinement module, see appendix B. The inputs are separated into airfoil coordinates in the first file, while the commands and flow conditions are written to the second file. Then, Xfoil is executed using Matlab's System command for the lift coefficients occurring for this lifting surface.

For the vertical tail the lift coefficient is always set to $C_L = 0$ as symmetric cruise flight is being considered. The lift coefficients for the horizontal tail or canard are obtained from the trim calculation of the AVL. It is assumed these trimmed coefficients are obtained by adjusting the incidence angle of the horizontal tail, not by elevator deflection. Cruise C_{L_h} values are always significantly smaller than the maximum coefficients reached during maneuvers in which the elevators are deflected. The lift coefficients of the aircraft are predefined in the Drag Module to discretize the drag polars of each module, because this module directs the activities of the other aerodynamics modules. The main wing lift coefficient is assumed to be equal to the aircraft lift coefficient. The aircraft lift coefficient array is constructed to range from $C_L = 0$ (steady flight only) up to the clean wing $C_{L_{max}}$, with denser spacing using a sine distribution around the expected cruise lift coefficient.

The transition point for a constant critical N-factor is listed per lift coefficient. The critical N-factor is linked to the freestream turbulence setting `FreestreamTurbulence`, set to $Tu = 7 \cdot 10^{-4}$ by default, which corresponds to roughly $N_{crit} = 9$ according to Mack's turbulence correlation given by equation 4.4 [34].

$$N_{crit} = -8.43 - 2.4 \cdot \ln(Tu) \quad (4.4)$$

4.5.3. Zero-lift drag coefficient

The x/c chord-wise fraction of the transition point as obtained from Xfoil is used as weighting factor for the laminar and turbulent skin friction coefficients of the equivalent lifting surface, performed per side. This scaling is detailed in equation 4.5. As such, span-wise variation in transition point is neglected. This assumption reduces the accuracy of the analysis but reduces the computational time.

$$C_{D_f} = C_{D_{f,laminar}} \cdot \left(\frac{x}{c}\right)_{transition} + C_{D_{f,turbulent}} \cdot \left(1 - \left(\frac{x}{c}\right)_{transition}\right) \quad (4.5)$$

The laminar and turbulent skin friction coefficients are obtained by empirical relations. The laminar flat plate friction coefficient is used up to the point of transition, see equation 4.6. The turbulent coefficient is found by interpolation of empirical trendlines dependent on Mach number and Reynolds number [27]. A fixed equivalent sand grain roughness of 0.0254 mm is used to determine the cutoff Reynolds number for $C_{Df,turbulent}$ with increasing Reynolds number.

$$C_{Df,laminar} = \frac{1.328}{\sqrt{Re}} \quad (4.6)$$

The skin friction coefficient C_{Df} is related to the zero-lift drag coefficient C_{D0} using equation 4.7 [27, 30]. A relation of this form can be obtained from the conceptual design books of both Roskam and Raymer. Both sources use the same method (it is based on a DATCOM method), linked to the thickness-to-chord ratio at the mean geometric chord (MGC). The differences can be found in the three undefined parameters in the equation, namely the airfoil thickness location correction L , the wing-body interference R_{wb} and the lifting surface correction factor R_{ls} .

$$C_{D0} = C_{Df} \cdot R_{wb} \cdot R_{ls} \left(1 + L \cdot \left(\frac{t}{c} \right)_{MGC} + 100 \cdot \left(\frac{t}{c} \right)_{MGC}^4 \right) \cdot \frac{S_{wet}}{S} \quad (4.7)$$

Raymer uses a continuous function to determine L as a function of $(x/c)_m$, the point of maximum thickness, while Roskam uses a switch at $(x/c)_m = 0.3$. These relations are seen in equations 4.8 and are illustrated in figure 4.16. It was decided to use the definition of Raymer because of its continuous nature, preventing any discontinuities in the drag coefficient if airfoils are modified at any point, a crucial element in automated tools, see Appendix B.

$$\text{Raymer: } L = \frac{0.6}{(x/c)_m}$$

$$\text{Roskam: } L = 1.2 \in (x/c)_m \geq 0.3$$

$$L = 2.0 \in (x/c)_m < 0.3$$

(4.8)

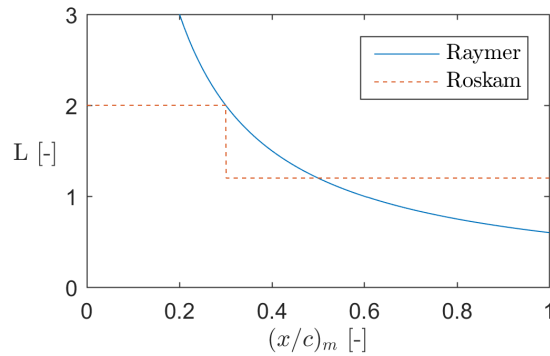


Figure 4.16: Airfoil thickness location correction factor

The lifting surface correction factor R_{ls} is obtained from a correlation with the Mach number and the sweep angle of the maximum thickness line of the wing. Raymer uses an equation to obtain the correction factor (see equation 4.9), while Roskam provides a figure that can be interpolated. The comparison between both methods is seen in figure 4.17, in which Raymer's lines are continuous and Roskam's curves are dashed. The differences cannot be explained, so the original Roskam method is used as R_{ls} remains rather constant at low sweep angles ($\cos(0) = 1$), as is expected from the nature of transition with increasing sweep.

The wing-body interference factor R_{wb} is a function of the fuselage Reynolds number in Roskam, but according to Raymer, this factor can be neglected. The intricate figure of Roskam is interpolated between the freestream Mach number curves to obtain the interference factor, labeled as R_{wf} in figure 4.18. However, almost all aircraft modeled in the Initiator operate at Reynolds number above 10^8 and Mach numbers above 0.6. This results in the same factor, roughly $R_{wb} = 1.015$, corresponding to the plateau in the figure. Being almost 1, the two methods are considered to be identical. Roskam's figure is used in the Initiator so that the higher fidelity data can be used in case of low speed conditions.

4.5.4. Enhanced drag polar

After analyzing all aerodynamic components with Xfoil the enhanced drag polar of the PDE module can be produced, referring back to figure 4.14b. The reduction in drag from the lifting surfaces is apparent when compared with figure 4.14a. As was visible in figure 4.15, the main wing has a large reduction in drag at approximately $C_L = 0.3$. Obviously, this reduction is mostly due to the biased choice in airfoil because this

$$R_{ls} = 1.34M^{0.18}(\cos \Lambda_m)^{0.28} \quad (4.9)$$

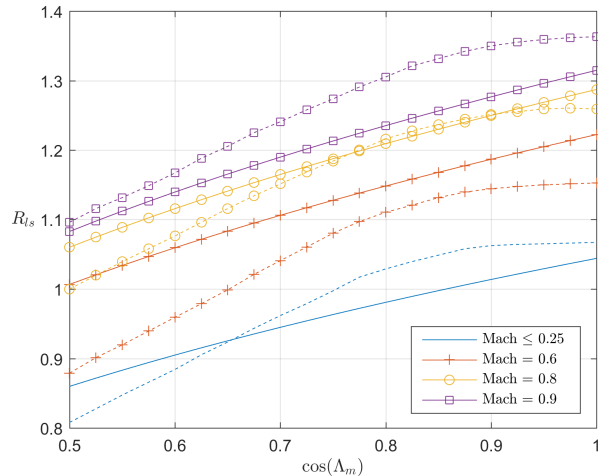


Figure 4.17: Lifting surface correction factor

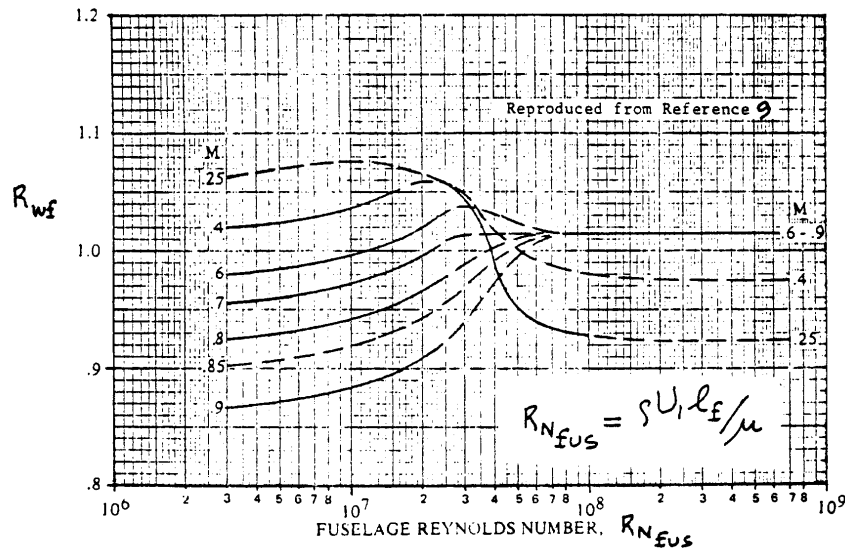


Figure 4.18: Wing-body interference factor, figure 4.1 from Roskam Part VI [27]

ignores several important practical considerations, such as maximum lift, structural efficiency, etc. As such, the feasibility of the drag reduction should be taken with a grain of salt, but the principle benefit is clear.

The extended laminar flow on both surfaces of the airfoil has been incorporated in the zero-lift drag calculation and reduced the main wing drag contribution from approximately 80 to 60 drag counts at $C_L = 0$ and as low as 50 counts at $C_L = 0.3$. This corresponds to a zero-lift drag reduction of 25-37% for the main wing. Similarly, the horizontal tail contribution has decreased by the same relative amount, but was smaller in absolute magnitude. The nacelle and highly swept vertical tail were not modified at this point.

Again, one aspect that is not taken into account is the increase of boundary layer instability from crossflow due to the increased pressure gradients of a wing at higher lift coefficients: Although highly stable in Xfoil, this would cause immediate cross-flow transition and disrupt the constant zero-lift drag coefficient distribution as is assumed in figure 4.14b. Fortunately, this component is relatively small for fuel burn calculations at higher lift coefficients because the induced drag contribution becomes larger than skin friction drag, as can be seen in the original (turbulent) case of figure 4.13: At $C_L = 1.05$ we can read $C_D = 0.1$ from figure 4.13, while the zero-lift drag coefficients are still $C_{D_0} = 0.02$ and $C_{D_0} = 0.015$ for the original and enhanced cases in figure 4.14. This equates to an error of approximately 5% compared to the turbulent drag coefficient if evaluated at the same lift coefficient.

4.6. Initiator results

This section presents the results of the modifications made to the Initiator program between versions 2.8 and 2.9 [51, 47, 52]. Verification of results has been performed thoroughly on multiple conventional aircraft, showing a maximum MTOM error of several percent, see figure 4.19. However, this will not be further discussed in this report as the focus will be on five business jets of varying size and top level requirements (TLR). These aircraft will illustrate both the new capability of modeling business jets and also the impact of applying laminar flow design when compared to a turbulent baseline produced by the same program.

An important remark to make at this point is the level of accuracy from the Initiator's calculations. The general trend of modules within the Initiator is that they are build to be as accurate as possible for all aircraft. As such, they are thoroughly linked with the continuously changing geometry, weights, etc. However, to reproduce specific aircraft, specific factors and offsets are needed to manipulate the calculations so that the results represent the actual aircraft. After all, generic methods such as empirical weight estimation methods are never flexible enough to reproduce all aircraft to high precision.

Therefore, it is deemed sufficient for the methods themselves to be reasonably accurate in an *absolute* sense, as long as they are highly accurate in a *relative* sense: Changes in drag from extended laminar flow should trickle down to the other computations of the Initiator. Only if these sensitivities are observed to be proportional to reality can the Initiator be confidently used to investigate new aircraft designs and concepts on the conceptual and preliminary design level. This condition is assumed to be met when the absolute results of the modules deviate within a reasonable margin for a large range of reference aircraft. As such, the separate modules have been individually tested to prove the accuracy of their relative results.

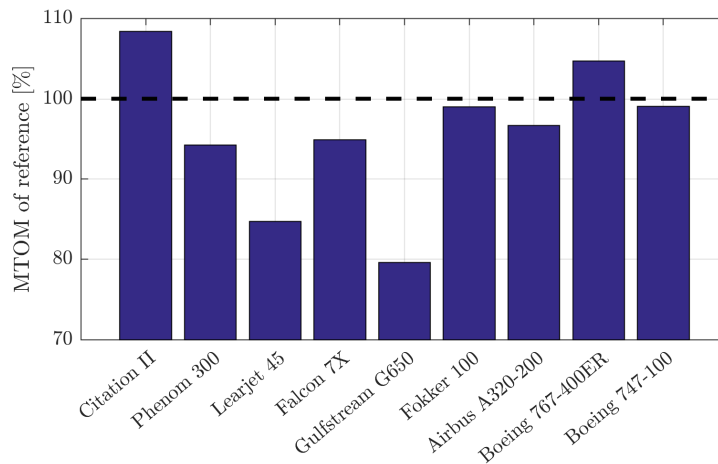


Figure 4.19: Comparison of maximum take-off mass results of the Initiator

4.6.1. Baseline aircraft

Although verification of all modules is largely omitted, some intermediate results of the Initiator are important to discuss. They will provide a qualitative picture of the fidelity of the Initiator, in addition to the quantitative build-up of the converged design. The Embraer Phenom 300 will be the example to discuss in detail. Results of several other business jets were attempted and are summarized in appendix C. These aircraft are described below and shown in figure 4.20 and they were selected to represent both average jets as well as some statistical outliers, both in size and in operational conditions.

- (a) Cessna Citation II: Low speed, small capacity jet with a large amount of reference data available. However, it is one of the few business jets with unswept wings because of its low Mach number. This is common for turboprop aircraft, so this case can be seen as a test of an outlier among jet aircraft.
- (b) Dassault Falcon 7X: Recent, large capacity, long range tri-jet, used as middle ground between business jets and small conventional jets. Due to the additional fuel tank in the fuselage and an additional engine, it has both a further aft center of gravity and a larger shift during cruise, leading to an extreme design case for business jets.

- (c) Learjet 45: Medium capacity, with moderate Mach number, range and payload requirements to illustrate an average business jet. The sizing is not expected to be problematic for this case.
- (d) Embraer Phenom 300: Recent, small capacity jet of similar design to larger jets as it is one of the few business jets with a kink in its main wing. The requirements are similar to the Citation-II but at higher cruise Mach number.
- (e) Gulfstream G650: Long range, large capacity jet. Known to have the highest cruise Mach number among business jets, pushing the limits of empirical sizing methods.
- (f) Fokker 100: A conventional type aircraft of identical configuration to most business jets, even slightly lighter than the G650 due to its shorter range.
- (g) Airbus A320-200: Generic conventional aircraft that is a classic benchmark for the Initiator considering its accuracy in regards to the empirical sizing methods.
- (h) Boeing 767-400ER: Long range version of larger conventional aircraft with a high payload capacity to mimic the long range of business jets.
- (i) Boeing 747-100: This variation of the first jumbojet is the largest aircraft of the baseline aircraft. This version is selected because of the available reference data to validate the result of the Initiator.



Figure 4.20: Baseline aircraft [48]

Originally, the Dassault Falcon 20 was included in the results, but the Initiator is not yet successful in resolving the uncommon top level requirements of this aircraft. The Falcon 20 has two mission definitions that define the design: A short range, high speed, low altitude mission with little payload and a longer range mission at lower speed and higher altitude but carrying more payload. The conventional mission variations in payload and range are easily combined into one design point that performs predictably and without error. However, when more parameters are modified the recombination results in large variations in fuel burn that do not seem to converge. Investigating the Initiator's robustness to analyze such spurious TLRs requires more effort and is left for future endeavors.

4.6.2. Embraer Phenom 300

Considering all data that the Initiator generates by converging a design (see appendix B for details), it is worthwhile to highlight some of the output of the reference aircraft being recreated. Some results of the Embraer Phenom 300 jet will therefore be discussed and visualized. The convergence was run with margin of 0.1% in consistency on the MTOM between iterations. The reference data known for the Phenom 300 from the business jet database is given in table 4.1. These data and more detailed cabin and planform dimensions were used to create the input and settings files for the Initiator. The turbulence reference, or baseline aircraft is created by assuming transition to occur on any surface at a Reynolds number of 100,000. Even on this relatively small aircraft this practically corresponds to fully turbulent, as it operates at $Re_c = 9.13 \cdot 10^6$, almost two orders of magnitude higher than the point of transition.

Table 4.1: Phenom 300 reference data. [32]

Passengers	10+2
Mach number	0.78
Altitude	12,500 m
Range	3,650 km
Payload	1,096 kg
MTOM	8,150 kg
OEM	5,204 kg
Fuel fraction	0.227
Thrust loading	0.355
Wing loading	2,806 N/m ²

Final result The geometry produced within the Initiator can be seen in figure 4.21. Some important characteristics that are chosen by the user and were not sized automatically are the main wing location and aspect ratio, engine locations, vertical tail planform, winglet and cabin location. Numerous minor values are required to define the spar, main wing kink, dorsal fin, etc. All of these values were selected to represent the reference aircraft geometry wherever no automated methods were available.

As can be seen, there is no wing-body fairing to smoothly connect the wing to the fuselage. This could have significant impact on wave drag computations if the Wave Drag Estimation module would be used in future versions of the Initiator. Currently, the lack of a fairing produces no error because of the constant wave drag increment on the drag coefficients, see section 4.4.

The MTOM has converged to a value of 7,682 kg. The OEM is predicted to be 4,848 kg, which leads to a harmonic mission fuel fraction of 0.226. Considering the 0.1% convergence margin on MTOM, this equates to a relatively large MTOM error of 5.8%. The fuel fraction is identical to the reference, so the low masses should originate from the OEM. More detailed results will be explained in the paragraphs below.

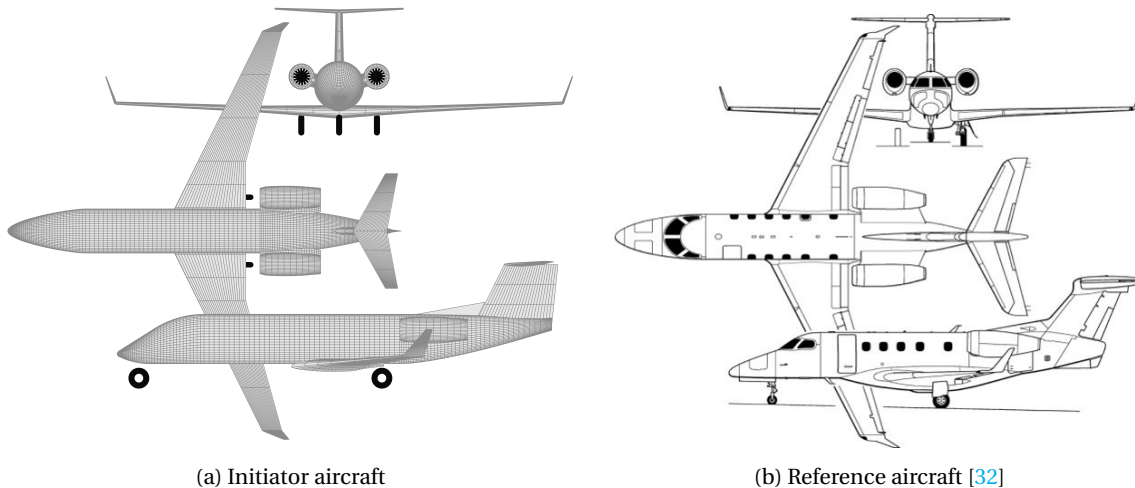


Figure 4.21: Reconstruction of the Embraer Phenom 300 geometry by the Initiator

Design point The reference aircraft is designed according to the design point in figure 4.22. In this *wing-thrust loading* diagram, several constraints are computed to determine a feasible design space. The constraints are explained in the legend of the figure, including the feasible design space illustrated by the filled green area. For jet aircraft, the design point is at first chosen to be at the highest wing loading and secondly at the lowest thrust loading. It can be seen that for the Phenom 300, the landing distance of 900 m and the take-off distance of 1128 m are sizing constraints.

The input variables that remain constant during the design convergence have been chosen as to reproduce a design point close to the known reference point. However, several parameters in the convergence, mostly the performance parameters such as the specific fuel consumption and the drag polar, will modify the design point. The final iteration has converged to the point $(W/S, T/W) = (2904, 0.353)$, which is deemed acceptable when compared to the reference values in table 4.1. This reference design point in the figure is shown by a black cross. In the results, the slightly under-predicted wing loading will produce a smaller reference area for an identical MTOM.

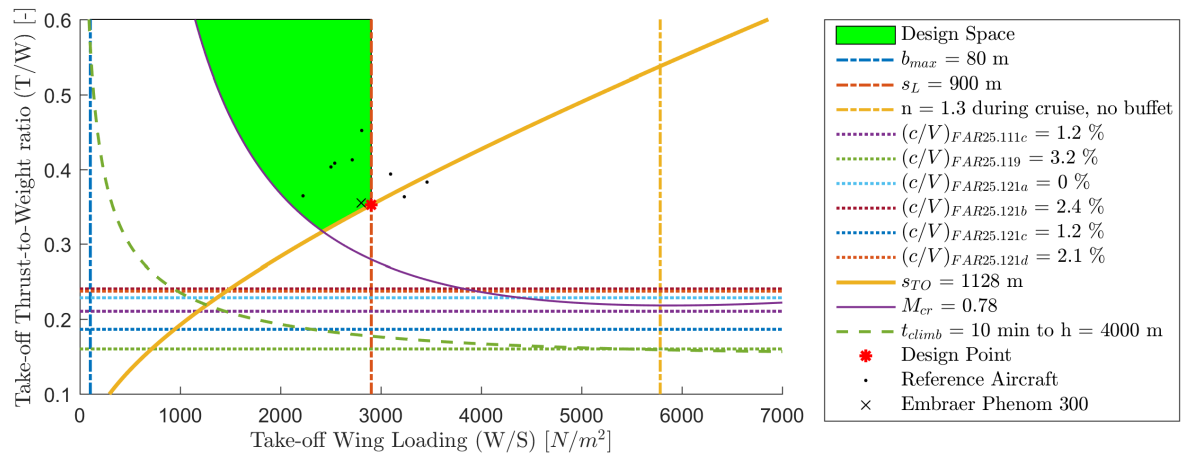


Figure 4.22: Design point for the Phenom 300 in the wing-thrust loading diagram

Payload-Range diagram The primary mission description of the the Phenom 300 will enforce the harmonic (design) mission, as no secondary mission is known. As such, the payload-range diagram given in figure 4.23 has a first maximum take-off mass mission at the range given in table 4.1, namely 3,650 km. The figure also illustrates the converged OEM and MTOM values, at 4,848 kg and 7,682 kg. The ferry mission, shown as the mission with maximum fuel and maximum range, is analytically computed by integrating a mission with zero payload mass until fuel has run out. The intermediate mission using maximum fuel, but partial payload to meet the MTOM, is extrapolated from the ferry mission using the lost-range method. With no secondary mission given as input to the Initiator, this intermediate mission should ideally converge to coincide with the harmonic mission if the total fuel volume in the aircraft is perfectly sized to meet the requirements of the primary mission. Surprisingly, the Phenom 300 model uses a fuselage fuel tank specifically sized to this primary mission, contradicting the result of the intermediate mission. A refined convergence margin on MTOM did not influence the outcome, hence it can be considered a methodological error within the Initiator.

Class 2 Weight Estimation Using the component weight estimation method of Torenbeek the breakdown of part masses is achieved [31, 51]. The pie charts in figure 4.24 provide the converged results of the individual mass subgroups. The charts start on the left (*nine o'clock*) to prevent overlapping labels. The groups are sorted by magnitude in clockwise direction and annotated in kilograms. The wing mass is been computed using EMWET, a semi-empirical analytic program specifically for wing structures [53]. The subfigure on the left shows the breakdown of the OEM, while the Systems subgroup is broken down once further in the chart on the right. Like many business jets, the Systems subgroup is relatively large.

The overall OEM of 4,848 kg is under-predicted when compared to the 5,204 kg from reference data, see table 4.1. Although there is no validation available for the exact masses of these subgroups, it can be seen that there is a feasible division. However, compared to most conventional aircraft results, the Systems group is far larger than usual. One item that might be underpredicted is the furnishing weight, which would be proportionally higher in well-furnished business jets. The major groups are expected to be the structural fuselage and main wing, followed by the two engines. The landing gear is lighter than normal due to the low wing configuration and the engine placement on the rear fuselage, making the main gears relatively short. The empennage has been computed using a composite scaling factor 0.75, reducing the masses of the horizontal and vertical tail to better compare with the carbon epoxy parts used in these groups [32].

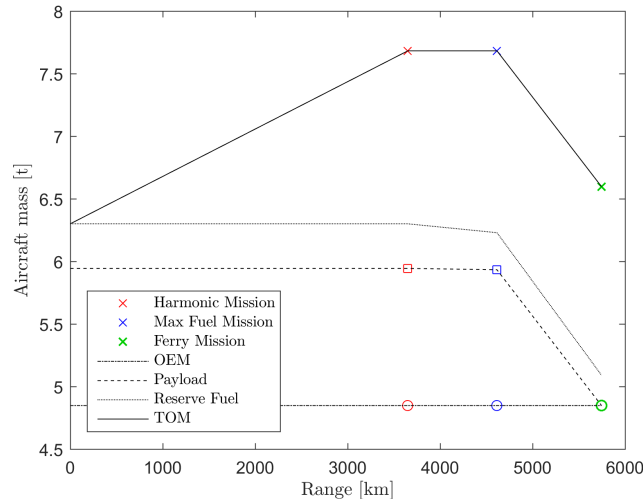


Figure 4.23: Payload-range diagram for the Phenom 300

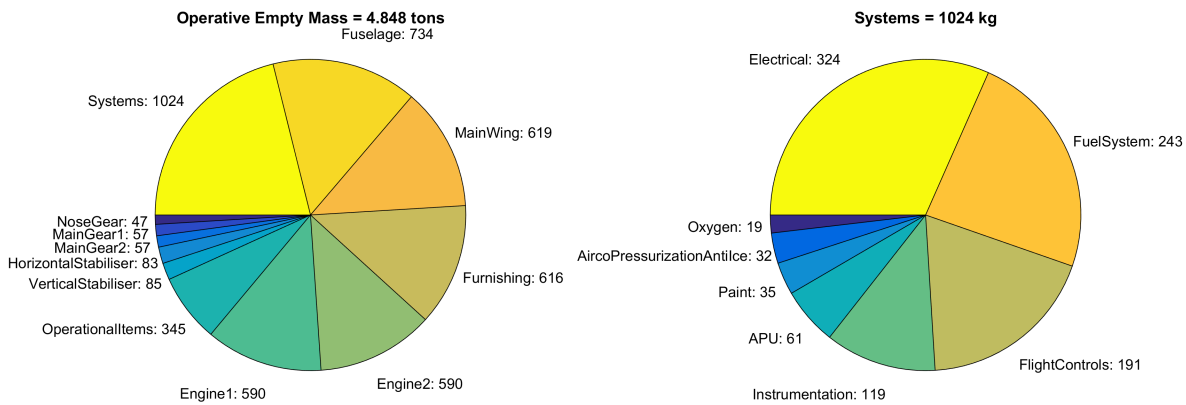


Figure 4.24: Class 2 weight estimation breakdown for the Phenom 300 using Torenbeek and EMWET

Drag polars The drag polars are an important category in the results considering the nature of this work. The 'turbulent' benchmark of the Phenom 300 can be seen in figure 4.25. The PDE module is used to create skin friction drag coefficients, plus the fuselage lifting drag, resulting in a $C_{D0} = 0.0155$. Again, all components are set to transition at a Reynolds number of 100,000. Individual contributions of the main parts at zero angle-of-attack (no fuselage lift) are given in table 4.2. The contributions of wave drag and induced drag are added to the PDE results to obtain the complete, clean drag polar of figure 4.25b. The optimal operating point has a value of $(L/D)_{max} = 19.88$ at $C_L = 0.72$. This lift coefficient is quite large but could be improved by additional laminar flow, at which point the drag polar will translate to smaller C_D values. Similar results were obtained for the other business jets, while the conventional aircraft had optimal L/D points at lower C_L values. However, this can also be adequately explained by an overestimation of the Oswald (span efficiency) factor, reducing the induced drag component. If this component (quadratic in C_L) would increase, the $(L/D)_{max}$ would decrease but move to a lower C_L . As most business jets use winglets, this warrants further investigation in the AVL implementation.

4.6.3. Business jet convergence

An interesting observation was made during the design convergence of several business jets: Reductions in fuel burn initially lead to an increase in trim drag. This occurs when the CG location of the aircraft moves forward because the aft fuselage tank is reduced in size. To maintain stability with a new CG location, the horizontal stabiliser will produce additional trim drag.

Table 4.2: Phenom 300 component friction drag.

Component	C_{D_0}	Percentage
Wing	0.0075	48%
Fuselage	0.0047	30%
Horizontal Tail	0.0018	12%
Vertical Tail	0.0008	5%
Nacelles	0.0007	4%
Total	0.0155	

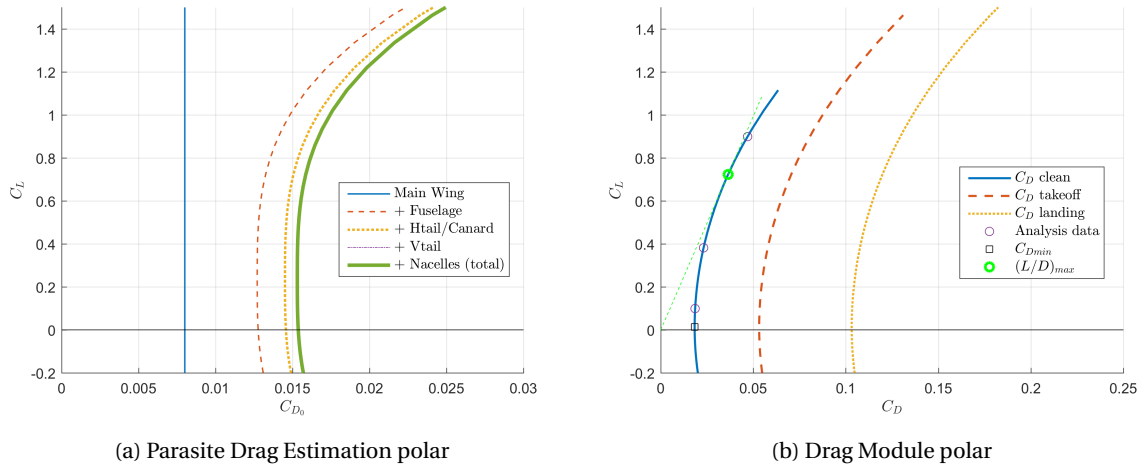


Figure 4.25: Drag polars for Phenom 300

While this can be adequately explained by the idea of solving for a feasible rather than optimal design, it also exposes another shortcoming within the program: To ensure a feasible design for both the landing gear and horizontal stabiliser, the main wing location has been fixed during convergence. It is therefore not relocated with shifts in CG to minimize the horizontal tail area. Shifts in CG by a reduction in fuelburn are therefore not properly taken into account during the optimization for longitudinal stability. This modification was required because the sizing of the landing gear, placed at the wing spars, has not yet been linked to the longitudinal stability and controllability calculations of the Initiator, often resulting in unfeasible designs. To remove this limitation, the horizontal tail size has to be combined with the landing gear size as the objective function for horizontal stability optimizations.

The final results of the convergence of the business jets were disappointing considering the accuracy of the Initiator for conventional aircraft. As was visible in figure 4.19, the business jet results fluctuated far more than the conventional jets and their MTOM are largely underestimated. When we compare the fuel fractions and OEM in figure 4.26, we see that these results are mostly influenced by the incorrect OEM estimations.

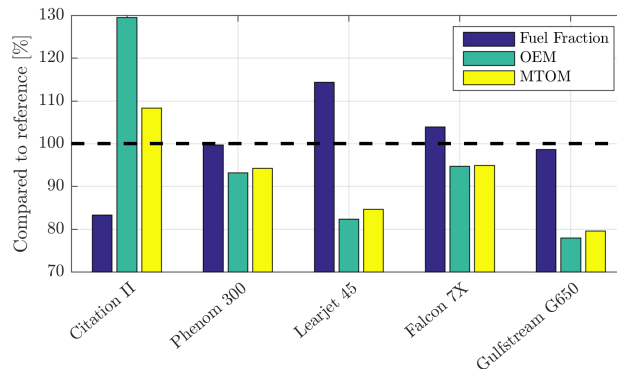


Figure 4.26: Comparison of business jet results of the Initiator with reference aircraft

4.7. Laminar Results

In this section, the influence of laminar flow on the business jets will be reviewed. Also, several conventional aircraft have been analyzed in similar fashion to identify trends related to aircraft size.

4.7.1. Embraer Phenom 300

The turbulent reference design of the previous section can be modified to have laminar flow on the components indicated in figure 4.27. The snow-ball effect on the aircraft is computed as a result of the convergence: Drag reduction leads to less fuel burn, leading to a smaller MTOM, which reduces fuel burn, etc. To have a better overview of the impact of laminar flow technology per component, these effects are build-up incrementally as seen in table 4.3. The reference aircraft generated by the Initiator is included in the first column. The differences with respect to the turbulent benchmark is indicated by the percentages. Similar tables comparing the results for the other reference aircraft can be found in appendix C.

As mentioned before, the turbulent benchmark is produced with a fixed transition Reynolds number of 100,000, corresponding to transition at approximately $< 1\%$ of the chord of every surface. The transition Reynolds number is then increased in three steps to 1, 3 and 7 million, while allowing the aircraft to convergence to a new feasible points intermediately. The last two Reynolds number values are not expected to be realistic but might illustrate a non-linear trend.

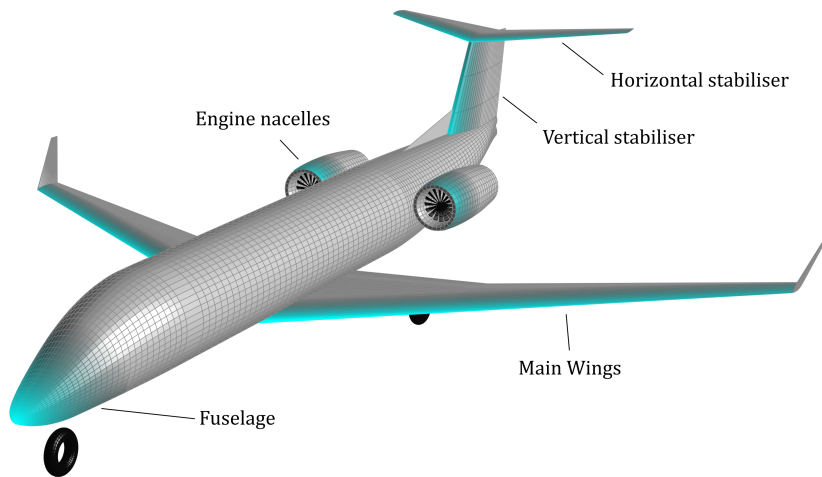


Figure 4.27: Surfaces of the aircraft with increased laminar flow

Table 4.3 shows several interesting trends regarding the sensitivity of some key performance indicators. For example, C_{D0} is influenced the most by an increase in the transition Reynolds number, as is expected. It also seems to be linearly correlated to the increase of the transition Reynolds number, discussed below. The maximum L/D ratio is impacted to a lesser degree, but has a very nonlinear trend. The fuel fraction declines in the same fashion as L/D , but the fuel mass increases at a faster rate as the aircraft converges to lower MTOM values due to the snowball effect. The smaller MTOM relates to smaller wings with less fuel capacity, but this decrease in capacity is not as large as the decrease in fuel volume for the harmonic mission. Therefore, the fuselage fuel tank can be completely removed after a transition Reynolds of 1 million. This is visible in the large change in maximum fuel mass at 1 million, but a stagnating decline at 3 and 7 million, similar in magnitude to the trend in MTOM.

4.7.2. Trendlines

The trends in C_{D0} were not only seen in the Phenom 300. If we normalize the transition Reynolds number to the MAC Reynolds numbers of each aircraft, we can see that this rule applies in general, see figures 4.28. The parameter Re_{tr}/Re_{MAC} might not be a fair representation of the actual requirements to obtain the laminar flow suggested by the parameter: For a given aerodynamic shape (i.e. airfoil) the location of transition moves upstream with increasing Reynolds number. In that sense, the Re_{tr} parameter is more applicable to compare the extend of laminar flow, not the ratio with the MAC Reynolds number. However, aspects such as the inviscid pressure distributions *do* scale and will thereby also scale the favorable pressure gradients that might keep the boundary layer laminar. Therefore, there is no definitive parameter and the trends have to be

Table 4.3: Laminar flow technology applied to the Embraer Phenom 300.

Transition Reynolds	0.1 10 ⁶	1.0 10 ⁶	3.0 10 ⁶	7.0 10 ⁶
MTOM [kg]	7682	7532 (-2.0%)	7019 (-8.6%)	6484 (-15.6%)
OEM [kg]	4848	4795 (-1.1%)	4552 (-6.1%)	4364 (-10.0%)
Fuel fraction	0.226	0.218 (-3.7%)	0.195 (-13.6%)	0.158 (-30.2%)
Harmonic fuel [kg]	1738	1641 (-5.6%)	1371 (-21.1%)	1024 (-41.1%)
Maximum fuel [kg]	1749	1629 (-6.8%)	1504 (-14.0%)	1403 (-19.8%)
(L/D) _{max}	19.88	20.57 (3.5%)	22.54 (13.4%)	27.87 (40.2%)
C _{D0}	0.0155	0.0141 (-8.2%)	0.0114 (-25.4%)	0.0068 (-55.6%)

interpreted. If these trends are plotted with respect to Re_{tr} , size of the aircraft sorts the results and removes any correlation, hence the ratio is used.

The aforementioned business jets and several conventional aircraft are included in the figure. It can be seen that the slope of the linear trends in C_{D0} are consistent between most aircraft. The linear trend is not expected if we consider the empirical approximation of the friction coefficient proportional to Re^{-n} of both laminar ($n = 0.5$) and turbulent ($n = 0.2$) boundary layers. The trend has to be attributed to the snowball effect of the convergence. The C_{D0} results can be normalized to their initial, turbulent values to determine a statistical average. For C_{D0} , it was found that the slope of the curves is -340 drag counts per unit of Re_{tr}/Re_{MAC} , with a standard deviation of 60 drag counts, see figure 4.28b. However, there is a slight correlation with aircraft size. Although the results presented here are coarse, they are useful when estimating these performance parameters for conceptual design.

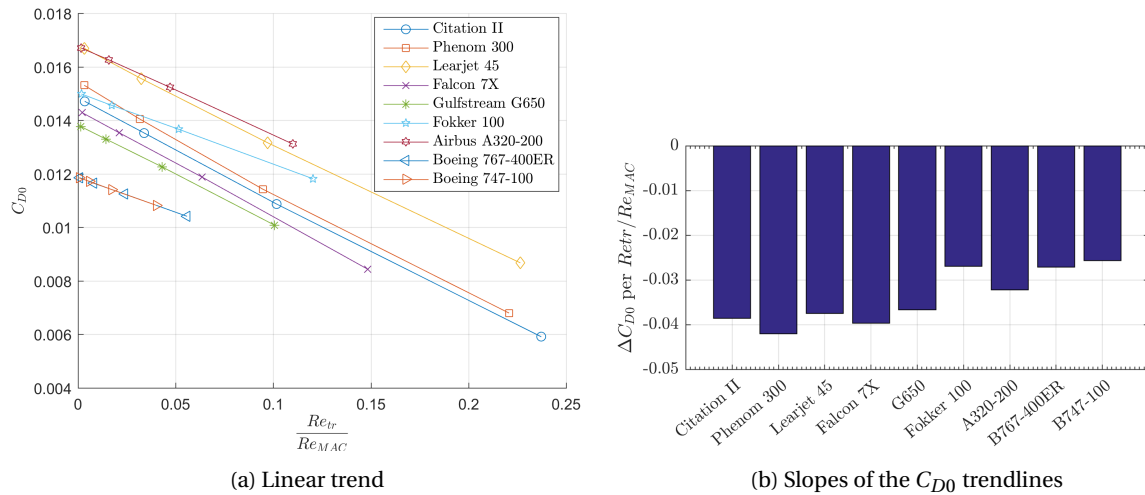


Figure 4.28: Aircraft results regarding C_{D0}

A measure of efficiency of the aircraft can be found for their respective harmonic mission profiles. This is defined as the fuel burn, normalized by the payload and range, having the unit $kg/(kg \cdot km)$. If we normalize this mission efficiency with the extend of laminar flow, we obtain the trend lines in figure 4.29. Several interesting results can be found: The two aircraft benefiting most from the laminar flow are the long range business jets, the Falcon 7X and the Gulfstream G650. The three smaller business jets benefit less and the two smaller, conventional aircraft benefit the least. The two larger conventional seem to be sway between the latter two groups, see the bold lines in the expanded subfigure.

One interpretation of these results is that both aircraft with little payload over long range flights benefit the most from the application of laminar flow under the same Re_{tr}/Re_{MAC} ratio. Inversely, large volumes of payload and short flights have a reduced effect. This can be explained by the subdivision of aircraft weight for these missions: Shorthaul flights have proportionally less fuel than longhaul flights, i.e. the fuel fraction is lower. It can therefore be concluded that is it easier to make laminar flow design cost-effective on long range aircraft with little payload, such as business jets.

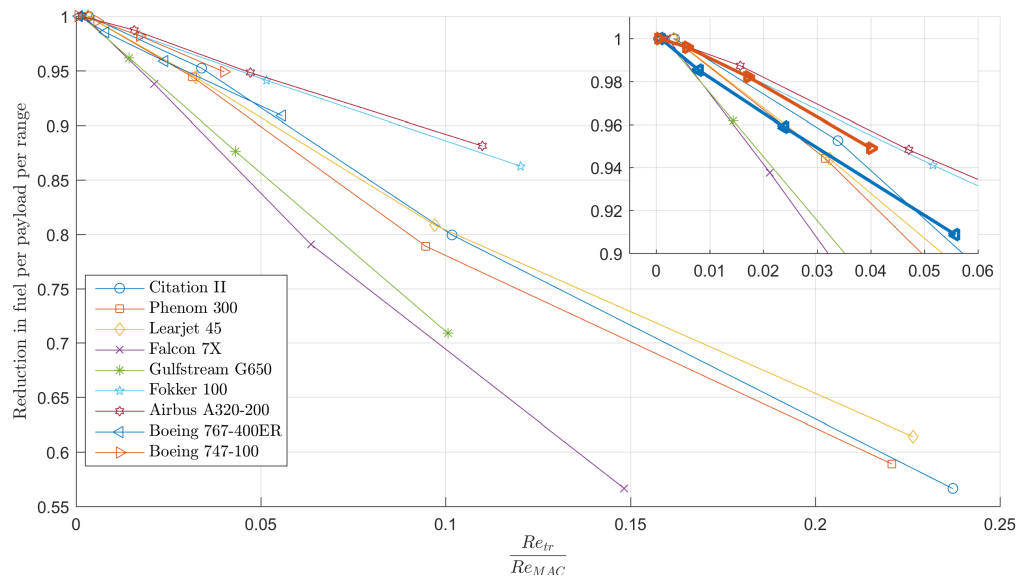


Figure 4.29: Decrease in fuel burn, reduced by payload and range, normalized by turbulent reference

5

Conclusions and Recommendations

This final chapter contains the conclusions and recommendations that were collected in this report. The conclusions are related to the research plan of this thesis, while the recommendations are an extensive overview of possible improvements and modifications of this work plus suggestions of new areas of research to pursue.

5.1. Conclusions

The main research question was given in chapter 1. It was formulated as:

"What are the effects of laminar flow technology on swept wing business jet design?"

The findings of this work for the sub-questions will be discussed first to build the groundwork for the main question. These topics were business jet design, laminar aircraft design and the stability calculations.

Business jets Sizing business jets using empirical design methods intended for conventional transport aircraft did not expose any fundamental limitations. The larger center of gravity shifts from larger fuel volumes were the main cause of problems in sizing the business jets. However, there are still several unexplained discrepancies in the weight estimations and complications in design methodology unique to business jets. Empirical weight estimation methods seem to require separate scaling factors, to account for different contributions of subgroups such as furnishing and system weights. As was observed, the conventional aircraft using the same methods had smaller deviations from validation data. For actual implementation into the Initiator, different design outcomes such as high fuel fractions required more adequate methods to construct and manage additional geometric detail such as additional fuel tanks and cargo storage.

Laminar design To include laminar flow in aircraft design, the zero-lift drag coefficient was linked to the point of transition. Resolving the boundary layer itself is computationally too expensive in conceptual aircraft design, so empirical approximations of the skin friction drag were used for the laminar and turbulent states. The final step is to apply these methods to each aerodynamic surface, which requires reliable geometric definitions from tools such as the Initiator. These definitions include consistent values of sweep, twist, airfoil data points, etc. The design and optimization of airfoils and wings for laminar purposes has briefly been touched, but no conclusive results were obtained.

Stability calculations Computing the stability of the boundary layer of wings of infinite span in subsonic conditions was successfully performed by the linear stability tool. The differences between similar solutions of the boundary layer and numerical solutions from the tool showed the necessity to fully compute the three-dimensional boundary layer. Applicability for design purposes, such as optimizations, was made possible by the automated framework and the eigenfunction filtering principle. The filtering proved to be a fast and robust method that has no causal connection to previous stability computations, removing user interaction in this process. The output of the linear stability tool, the N-curve envelopes, can directly be applied to estimate transition locations induced by either Tollmien-Schlichting or stationary crossflow modes.

Throughout this report, four levels of fidelity regarding transition prediction have been used: Fixed Reynolds number, empirical correlation using Xfoil, surrogate models and the linear stability tool. Deciding on which method to use depends on the required accuracy versus the computational time to be invested. For simple conceptual aircraft design, both the fixed Reynolds number and Xfoil methods are most suited. If building a surrogate model is a feasible option regarding the available airfoil and the computational time needed to run all cases, it is the best compromise accuracy and speed due to the simplicity of interpolation. If no deprecation in accuracy is allowed, as is the case with optimizations, solving the exact case with the linear stability tool is the best option. These conclusions apply if only the four methods presented in this report are considered, as other possibilities exist outside this work.

Research question This brings us to the main research question itself. From the Initiator, some general remarks can be made regarding laminar flow on business jets. The use of laminar flow technology to extend the range of the laminar boundary layer will on average reduce the zero-lift drag coefficient of jet aircraft by 340 drag counts per unit of Re_{tr}/Re_{MAC} . The efficiency of the aircraft is most influenced by the use of laminar flow if the aircraft is designed for long range missions with little payload, in which the fuel mass is the largest contribution to the total aircraft mass. No significant differences have been found between the use of laminar flow on business jets or conventional aircraft.

5.2. Recommendations

For future continuation of the research performed for this thesis, some recommendations can be made. To organize all suggestions, these are separated into three topics: General comments, ones specific to the linear stability tool and finally program improvements to the Initiator.

General Regarding the use of laminar flow in aircraft design, some general recommendations can be made for future work.

1. To further substantiate the benefits of surrogate modeling, an airfoil has to be designed for extended laminar flow at high sweep angles. A surrogate model based on this new airfoil is then a valuable input to the design of laminar wings (and sequentially, aircraft). As design is an iterative process, a fast but accurate evaluation of the wing performance is required when modifying basic parameters such as aspect ratio, taper, etc. The HSNLF airfoil used for this thesis was not sufficient to test this capability.
2. During attempts to optimize an airfoil for a given wing geometry and fixed flight conditions, it was immediately clear that gradient based optimization on the transition location is not feasible. It is inherently discontinuous if the N-factor envelopes are not monotonically increasing at all times, because the intersection with a critical N-factor could occur at any point. For gradient optimizations, it might be possible to prescribe a required N-curve envelope itself and use that as the objective of the optimization. Otherwise, it is necessary to use a more robust method such as a genetic algorithm to investigate the entire design space.
3. The initial topic of this thesis was to utilize flow control to influence the extend of laminar flow. The most prevalent method in literature is boundary layer suction, either actively or passively. In both cases a balance has to be struck between the shaping of the airfoil and the volume of air drawn from the flow, i.e. the suction requirement. Regarding the linear stability tool, it is trivial to implement suction into the boundary layer solver, but the influence on the Orr-Sommerfeld solver is not known. The influence of the components required to build a wing using flow control on the aircraft as a whole can also be incorporated with the Initiator.
4. Although the technical aspect of designing laminar flow surfaces have been addressed, the feasibility of the design has a breaking point regarding the cost aspects of building and maintaining the aircraft. In short, the reduction of fuel costs must out-way the increased manufacturing costs and the increased maintenance related to cleaning and repairing of a laminar surface. This side of the process is of interest because it will quantify the need for the aerospace industry to move to laminar design.
5. The topic of equivalent sand grain roughness has been largely ignored, considering the combination of relatively small Reynolds numbers on business jets and the high production quality required for laminar flow application. For conventional aircraft it is advised to investigate the effects of roughness in further detail. Additional physical effects from steps/gaps at wing elements such as slats and flaps (but also maintenance hatches and paneling joints) require even higher fidelity tools than linear stability theory and are worthwhile to incorporate in laminar design from an early point in the design process.

Linear stability tool The linear stability calculations incorporated in the linear stability tool are a first functional version. Several areas of improvement were already discussed in chapter 2 and will be reiterated here.

1. An investigation into the numerical errors of the Crank-Nicolson scheme of the boundary layer solver during pressure gradients is needed. As was postulated, these will probably be contained in the formulation of the discretization scheme of the forcing term of the equation, as these errors were observed to be directly proportional to the pressure gradient.
2. To increase the speed of the tool, it is worthwhile to implement the temporal stability calculations instead of the spatial methodology. Then, using the Gaster transformation is applied and iterated until convergence. Considering the reduced size of the computational system if the temporal formulation is used, this is likely to significantly speed up the code if convergence is guaranteed to occur within 16 iterations.
3. To accurately resolve the flowfield of transonic aircraft, the addition of a compressible boundary layer and stability solvers might be warranted. While this increases the complexity and thereby computational time of the program, having the capacity to incorporate these effects is valuable for the sake of verification of results. Also, it should be tested whether oblique TS waves and traveling CF instability is properly captured by the methods of the tool. This requires a review on the integration direction, because different integration paths result in different N-factor curves which are all valid.
4. The limits of the domain along the ω or β variables are prescribed at this time. It should be possible to use an empirical correlation at each boundary layer station using parameters such as the Reynolds number, shape factor or crossflow to compute the required limits. For ω for example, the unstable regions of the Falkner-Skan stability diagrams can be used to compute the limits with higher accuracy.
5. The refining of the grid points by solving a coarse and fine grid is functioning as intended. However, a more elaborate method to determine what combinations of Re_l , ω and β to evaluate could be of use, possible in multiple steps of refinement. The primary concern in improving this area is to not interfere with the parallel processing paradigm. For example, to reduce the overhead of the process, the current implementation is limited by passing identical velocity profiles (i.e. Re_l) for a range of points (ω/β).
6. Regarding eigenfunction filtering: The reversal of crossflow due to reversal of the external pressure gradient introduces a new crossflow mode in the eigenvalue spectrum. However, this mode requires an increased level of discretization if the crossflow is still small. As such, the mode might not exist in the eigenvalue spectrum, resulting in no eigenfunction to filter for the same point in the boundary layer (Re_l). Handling this exception has proved to be a struggle and required manual intervention in approximately 5% of the analysed cases, mostly in low Reynolds number conditions. Other than increasing the discretization in all cases, no direct solution is known.

Initiator Specifically to the Initiator program, the recommendations relate to additions and improvements of or algorithms or code. It is hoped these comments will be used as a guide for future development.

1. The design point regarding the wing- and thrust-loading of the aircraft within the Initiator is poorly coupled with the higher fidelity computations already present (Mission Analysis module) or currently in development (high-lift sizing). The results of these computations should feed back to this initial module to replace the assumptions used in the first iteration(s). These assumptions keep the performance constraints constant and hereby inconsistent with the current design and ultimately unfeasible. As such, a more physical determination of the design point is advised.
2. The airfoil class updates made the data related to the airfoil shape and properties more accessible. However, the inputs for specific external programs (such as Xfoil and AVL) are still created separately in different modules, often inconsistently. It would be beneficial to extend the airfoil class with two methods that write *dat* or *txt* files on demand, thereby encapsulating the exact formatting rules.
3. Cabin design has room for improvement regarding the removal of seats in tapered rows. At the moment, the center seats are reduced in number first and all seats are shifted inwards. In conventional aircraft, seats are connected to several rails that are straight in longitudinal direction, to accommodate different layouts for different operators. Hence, some longitudinal aligning of the seats within the tapered section would be beneficial to consider.
4. For the inside-out optimization scheme, it might be useful to include the possibility to use CST coefficients for the outer hull instead of arcs. Although this is not consistent with the definition of the oval fuselage concept, it increases the flexibility of modeling unconventional concepts which not necessarily utilize the oval fuselage concept.

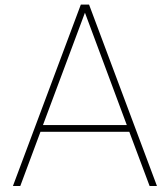
5. A limitation in the fuselage design is the identical tapering lengths of the tail or nose on the top and bottom of the fuselage. Most aircraft have a tail bottom contour that is tapered further to the front than the top contour, to accommodate alleviate the landing gear length: The scrape angle is increased by larger tapering lengths. To include this possibility in the Initiator, several methodological changes are required in the build-up of the fuselage. Also, this will complicate the cabin planform, as there is no precise kink in the planform if the shaping of the nose or tail does not end in a point but over a region.
6. The current implementation of fuel tanks within Initiator does not utilize the object oriented framework. As such, there are duplicate functions for every part that can contain a fuel tank. While this makes the overview of the code unnecessarily complex, it also limits the possibility to include multiple tanks in a single part. It is advised to create a fuel tank class with abstract function to determine parameters such as volume, center of mass, etc. Then, multiple instances (objects) of the class can be added to each part without complicating the methodology.
7. Also related to the placement of fuel tanks, the absence of a wing-body fairing is a discrepancy for wave drag estimations. It is worthwhile to include a new design routine for this fairing that accounts for the storage of fuel, landing gear and the cross-sectional area of the aircraft. The new geometry functions added to build the fuselage are directly applicable for this purpose, but no methodology is available to design this component.
8. The horizontal stability optimization scheme modifies the longitudinal position of the main wing to minimize the horizontal tail surface area. This does not take the landing gear design into account and required a fixed wing position for the feasible convergence of business jets. A combination of horizontal tail size and the landing gear size is required for this optimization to function properly for business jets.
9. By manually adjusting the order and content of the design convergence, the feasibility and computational time of the Initiator have been improved considerably. However, with the addition of future modules, different aircraft configurations or even for further improvements in computational performance it is critical to fundamentally improve the methodology of the convergence. Updating the Initiator to the current state has unveiled that the convergence has to account for three processes: 1) automatic handling of different levels of fidelity, 2) usability of computational results from preceding iterations and 3) thorough usage of the object oriented paradigm to handle relations between modules. Fortunately, research to implement such considerations has already been performed or is in progress.

Bibliography

- [1] Cleansky. *About CleanSky2*. Accessed on 01/05/2015. URL: <http://www.cleansky.eu/content/homepage/about-clean-sky-2>.
- [2] Anonymous. *Clean Sky 2 Joint Technical Program*. Program Proposal. Version 5. Clean Sky 2 J.U., 2015.
- [3] P. Okonkwo and H. Smith. "Review of evolving trends in blended wing body aircraft design". In: *Progress in Aerospace Sciences* 82 (2016), pp. 1–23.
- [4] I. Kroo. "Nonplanar wing concepts for increased aircraft efficiency". In: *VKI lecture series on innovative configurations and advanced concepts for future civil aircraft* (2005), pp. 6–10.
- [5] J.D. Jr Anderson. *Fundamentals of aerodynamics*. Tata McGraw-Hill Education, 1985.
- [6] A.L. Braslow. *A History of Suction-Type Laminar-Flow Control with Emphasis on Flight Research*. NASA History Division, 1999.
- [7] R.D. Joslin. *Overview of laminar flow control*. Citeseer, 1998.
- [8] K.H. Horstmann and L.M.M Boermans. "Evolution of Airfoils for Sailplanes". In: *2003 AIAA/ICAS International Air and Space Symposium and Exposition: The Next 100 Years*. 2003.
- [9] W.S. Saric and H.L. Reed. "Toward practical laminar flow control-remaining challenges". In: *AIAA paper* 2311 (2004), p. 2004.
- [10] A.M.O. Smith and N. Gamberoni. *Transition, Pressure Gradient, and Stability Theory*. Douglas Aircraft Company, 1956.
- [11] J.L. van Ingen. *A Suggested Semi-empirical Method for the Calculation of the Boundary Layer Transition Region*. Tech. rep. Delft University of Technology, 1956.
- [12] G. Schrauf. "Transition prediction using different linear stability analysis strategies". In: *AIAA Paper* 1848 (1994).
- [13] J.L. van Ingen. *A new eN database method for transition prediction*. Technical Report. Delft University of Technology, 2006.
- [14] M. Drela and H. Youngren. *XFOIL 6.9 User Guide*. MIT Aeronautics and Astronautics, Aerocraft Inc.
- [15] H.L. Reed and W.S. Saric. "Stability of three-dimensional boundary layers". In: *Annual Review of Fluid Mechanics* 21.1 (1989), pp. 235–284.
- [16] M. Gaster. "A simple device for preventing turbulent contamination on swept leading edges(Preventing turbulent contamination of laminar flow on highly swept wings by attaching bump on leading edge)". In: *Royal Aeronautical Society* 69 (1965), p. 788.
- [17] A. Smith and D.I.A. Poll. *Instability and Transition of Flow At, and Near, an Attachment-line: Including Control by Surface Suction*. Tech. rep. National Aeronautics and Space Administration, 1998.
- [18] V. Schmitt et al. *Hybrid laminar fin investigations*. Tech. rep. DTIC Document, 2001.
- [19] Gortler-Taylor Vortex Flows. *Figure 2: Vortices in the boundary layer of a concave wall*. Accessed on 21/10/2016. URL: <http://thermopedia.com/content/817/>.
- [20] C.W. Brooks Jr, Harris, and W.D. C.D. Harvey. *The NASA Langley Laminar-Flow-Control Experiment on a Swept, Supercritical Airfoil*. Tech. rep. National Aeronautics and Space Administration, 1989.
- [21] E.M. White. *Viscous Fluid Flow*. McGraw-Hill series in mechanical engineering. McGraw-Hill, 1991.
- [22] W.S. Saric, H.L. Reed, and E.B. White. "Stability and transition of three-dimensional boundary layers". In: *Annual Review of Fluid Mechanics* 35.1 (2003), pp. 413–440.
- [23] D. Arnal, G. Gasparian, and H. Salinas. "Recent advances in theoretical methods for laminar-turbulent transition prediction". In: *AIAA Paper* (1998), pp. 98–0223.

- [24] D. Arnal, G. Casalis, and R. Houdeville. "Practical transition prediction methods: subsonic and transonic flows". In: *VKI Lectures Series Advances in Laminar-Turbulent Transition Modelling* (2008).
- [25] C. Chang. "LASTRAC. 3d: Transition prediction in 3D boundary layers". In: *AIAA Paper 2542* (2004), p. 2004.
- [26] N. Krimmelbein. "Industrialization of the Automatic Transition Prediction in the DLR TAU Code". In: *Computational Flight Testing*. Springer, 2013, pp. 89–98.
- [27] J. Roskam. *Airplane Design, Part VI: Preliminary calculation of Aerodynamic, Thrust and Power Characteristics*. DARcorporation, 1989.
- [28] R.J.M. Elmendorp, R. Vos, and G. La Rocca. "A conceptual design and analysis method for conventional and unconventional airplanes". In: *ICAS 2014: Proceedings of the 29th Congress of the International Council of the Aeronautical Sciences, St. Petersburg, Russia, 7-12 September 2014*. International Council of Aeronautical Sciences. 2014.
- [29] J. Roskam. *Airplane Design, Part I: Preliminary Sizing of Airplanes*. DARcorporation, 1985.
- [30] D.P. Raymer, American Institute of Aeronautics, and Astronautics. *Aircraft design: a conceptual approach*. Educ Series. American Institute of Aeronautics and Astronautics, 1989.
- [31] E. Torenbeek. *Synthesis of Subsonic Airplane Design: An Introduction to the Preliminary Design of Subsonic General Aviation and Transport Aircraft, with Emphasis on Layout, Aerodynamic Design, Propulsion and Performance*. Delft University Press.
- [32] Defence & Security IHS Aerospace. *Jane's online research and analysis platform*. Accessed on 01/05/2015. URL: <https://janes.ihs.com>.
- [33] FlightGlobal. *Falcon 8X cutaway*. Accessed on 16/10/2016. URL: <https://www.flightglobal.com/assets/getasset.aspx?itemid=55649>.
- [34] L.M. Mack. *Transition and laminar instability*. Technical Report. Jet Propulsion Laboratory, 1977.
- [35] H. Schlichting et al. *Boundary-Layer Theory*. Springer, 2003.
- [36] G.H. Golub and C.F. Van Loan. *Matrix computations*. Vol. 3. JHU Press, 2012.
- [37] M. Gaster. "A note on the relation between temporally-increasing and spatially-increasing disturbances in hydrodynamic stability". In: *Journal of Fluid Mechanics* 14.02 (1962), pp. 222–224.
- [38] M.R. Malik. "Numerical methods for hypersonic boundary layer stability". In: *Journal of Computational Physics* 86.2 (1990), pp. 376–413.
- [39] K.J. Groot. "Derivation of and Simulations with BiGlobal Stability Equations". MA thesis. TU Delft, Delft University of Technology, 2013.
- [40] P.J.J. Moeleker. *Linear Temporal Stability Analysis*. Master Booklet. Delft University Press. 1998.
- [41] J.K. Viken et al. *Design of the low-speed NLF (1)-0414F and the high-speed HSNLF (1)-0213 airfoils with high-lift systems*. Tech. rep. Langley Research Center, NASA, 1987.
- [42] M. Drela. *MSES 3.05 User Guide*. MIT Aeronautics and Astronautics. 2007.
- [43] C.J. Atkin and G. Schrauf. "Progress in linear stability methods for design applications". In: *Proceedings of ECCOMAS*. 2000.
- [44] K.J. Groot, F. Pinna, and B.W. Van Oudheusden. "On closing the streamwise BiGlobal stability problem: the effect of boundary conditions". In: *Procedia IUTAM* 14 (2015), pp. 459–468.
- [45] Kristian Schmidt. "A Semi-Analytical Weight Estimation Method for Oval Fuselages in Novel Aircraft Configurations". MA thesis. Delft University of Technology, 2013.
- [46] Y.M. Baan. "A hybrid method for the interior and exterior design of blended-wing-body cabins". MA thesis. Delft University of Technology, 2015.
- [47] M.N. Roelofs. "Semi-Analytical Composite Oval Fuselage Mass Estimation". MA thesis. Delft University of Technology, 2016.
- [48] Wikimedia Commons. Accessed on 01/06/2016. URL: <https://commons.wikimedia.org>.
- [49] B.M. Kulfan. "Universal Parametric Geometry Representation Method". In: *Journal of Aircraft* (2008).
- [50] M. Warmenhoven. "A Preliminary Drag Estimation". MA thesis. Delft University of Technology, 2012.

- [51] D. Decloedt. "Investigation into the effect of relaxed static stability on a business jet's preliminary design". MA thesis. Delft University of Technology, 2016.
- [52] M.T.H. Brown. *Improving the Performance of Longitudinal Stability Estimation within the Initiator*. Master Orientation Project Report (unpublished). Delft University of Technology, 2016.
- [53] A. Elham. "Weight Indexing for Multidisciplinary Design Optimization of Lifting Surfaces". PhD thesis. Delft University of Technology, 2013.
- [54] IHS Engineering Sciences Data Unit. *ESDU 74018. Lost range, fuel and time due to climb and descent: aircraft with turbo-jet and turbo-fan engines*. 2000.
- [55] M.A.Y. Ramakers. "Accelerating aircraft design using automated process generation: An experimental architecture for aircraft design software". MA thesis. Delft University of Technology, 2015.



Aircraft database

Below is a list of the aircraft incorporated into the business jet database. Statistical outliers are excluded when querying data from the Initiator database.

Table A.1: Aircraft in Initiator database

Beechcraft Premier I	Dassault Falcon 50	Hawker 125
Bombardier Challenger 300	Dassault Falcon 5X	Hawker 200
Bombardier Challenger 350	Dassault Falcon 7X	Hawker 400 (450XP)
Bombardier Challenger 600	Dassault Falcon 8X	Hawker 750
Bombardier Challenger 800	Dassault Falcon 900 (EX)	Hawker 800 (850)
Bombardier Global Express 5000	Eclipse 400	Hawker 900 XP
Bombardier Global Express 6000	Eclipse 500/550	IAI Astra SP
Bombardier Global Express 7000	Embraer Legacy 600	IAI 1125 Westwind 1
Bombardier Global Express 8000	Embraer Legacy 650	Learjet 24
Cessna Citation II	Embraer Lineage 1000	Learjet 25
Cessna Citation Bravo	Embraer Phenom 100	Learjet 28
Cessna Citation Encore	Embraer Phenom 300	Learjet 29
Cessna Citation III	Gulfstream 100	Learjet 31 (31ER)
Cessna Citation VI	Gulfstream 150	Learjet 35
Cessna Citation VII	Gulfstream II	Learjet 36
Cessna Latitude	Gulfstream 200	Learjet 40 (40XR)
Cessna 525 Citation M2 (CJ1)	Gulfstream 280	Learjet 45 (45XR)
Cessna Citation Mustang	Gulfstream III	Learjet 55C/ER
Cessna Citation Sovereign	Gulfstream G300 (G350)	Learjet 60
Cessna Citation V	Gulfstream G400 (IV)	Learjet 70
Cessna Citation X	Gulfstream G450	Learjet 75
Cessna Citation XLS	Gulfstream G500	Learjet 85
Cirrus Vision SF50	Gulfstream G550 (V)	Pilatus PC-24
Dassault Falcon 100	Gulfstream G650 (VI)	Sino Swearingen SJ30-2
Dassault Falcon 2000EX (LX)	Gulfstream G600	
Dassault Falcon 200 (20)	Grob G180 SPn	



Initiator modifications

In addition to the modifications presented within this report, large parts of the Initiator were revised or updated to increase performance in both time as accuracy. However, they are not directly related to the thesis topic and instead these changes are listed here.

Additions & Revisions

Modules and calculations which were created to improve accuracy and consistency, or reviewed and modified in an effort to restore (original) functionality.

1. Setting files. First, the creation of several functions to modify all setting XML files simultaneously and consistently. This prevents the common issue of ill-formed XML files and allows for automated parameter sweeps of assumed values (such as transition Reynolds number). Second, the original setting files have been separated into four different degrees of variation: 1) Regulations, 2) Settings unrelated to the aircraft but to the program only, 3) settings general for any aircraft and 4) settings unique to each aircraft. The first three categories were placed in separate files, halving the number of settings to be stored per aircraft. The distinction between categories is at times rather vague but has significantly reduced the workload when modifying inputs or creating new aircraft files.
2. Directional Stability Estimation. Improved computational speed and robustness by optimizing for weight plus drag, instead of tail area. This included major updates in reading data from figures and necessitated the geometrical implementation of the dorsal fin. However, results are still incredibly sensitive to other aircraft parameters and at the time of writing, the vertical tail area is structurally under-predicted for conventional and over-predicted for cruciform/T-tail configurations. A large description of the current state is given in the module's run file.
3. Mission Analysis. Inserted checks and plots to notify the progression of the aircraft and guarantee a feasible mission execution. Most important, out-of-fuel cases are now included in the resulting fuel fractions and design convergence. Remaining issue is the thrust loading and/or flight speed during the climb phase, which at times limits the climb altitude. No feedback mechanism is in place to compensate for this error and it will crash the program for aircraft which are statistical outliers.
4. Position Landing Gear. Restored functionality, but the method is not robust enough to find a feasible design point and is not utilized as such. Currently a lean optimization in the Class 2 module that includes all landing gear design criteria is utilized instead, which can produce feasible landing gear for fuselage and wing mounted gears. In addition, the optimization framework can converge to a near-feasible design instead of crashing the code, if no feasible design is possible. An interesting addition would be to connect the semi-empirical weight estimation of the PLG module to the new optimization.
5. Wing Refinement. Integrated with the existing Initiator wing and airfoil definition, significantly improving the accuracy of the Xfoil analyses used in the root-design section of this module. In addition, included a simple wing twist design routine, but pending further investigation on AVL this has been turned off.

- Engine geometry. Split the engine into its major components, allowing multiple engine architectures to be incorporated into the Initiator. Instead of solely a nacelle, the Engine class is now defined as the combination of nacelle, fan, centerbody, motor and possibly pylon geometries. The nacelle and centerbody are geometric entities using the new *Revolute* class, while the Fan, Motor and Pylon are new classes nested in the engine. The property/attribute fields are hierarchically linked with dependencies, much like the wing and sections as described in section 4.3.

Design convergence

A consequence of using higher fidelity tools to recalculate known values, or design methods of an iterative nature, is to verify the convergence of the results. Within the Initiator, convergence is verified by tracking the maximum take-off mass (MTOM) of the design, see the Initiator's progress monitor in figure B.1. The program will iterate its modules until the MTOM after successive calculations no longer varies outside a fixed margin. This does not guarantee convergence of other parameters (such as the lift-over-drag ratio) but the MTOM does represent the contributions of most, if not all, design parameters. Hence, a convergence in MTOM can be assumed to include a convergence of the full aircraft design. It should be noted that the convergence does not represent the optimal aircraft design, only consistency in calculation and thereby feasibility of the result.

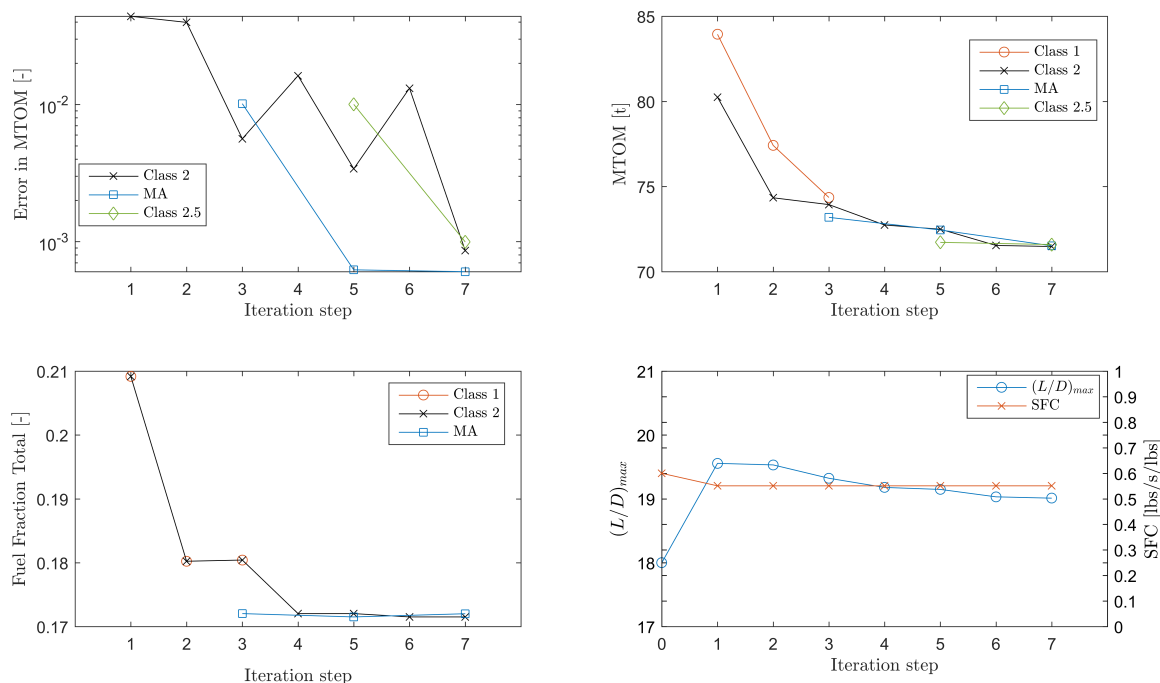


Figure B.1: Initiator design convergence progress of an Airbus A320-200

In the convergence monitor of figure B.1 several subfigures are used to track convergence and the influence of several main parameters. For all subfigures, the black lines with crosses correspond to the individual Class 2 Weight Estimation evaluations, which modifies OEM and not the fuel fractions. Orange circles indicate semi-empirical fuel fractions (lost-range method [54]), blue squares indicate a time-integrated fuel fraction and green diamonds include advanced semi-empirical sizing methods for wing and fuselage contributions to OEM. The bottom two figures are not parameters of the convergence, but will indicate the causality within the convergence. For example, a low lift-to-drag ratio or a high fuel fraction will lead to an increase in MTOM.

N2 chart

In figure B.3, the modules or module groups which are used within the design convergence are placed in a N2 chart. Note, many modules and methods are grouped together under one category or are excluded to make this figure more comprehensible. The chart illustrates the feed-forward (above the diagonal) and feed-

back (below the diagonal) of the flow of convergence related parameters and data. The three program loops representing the levels of fidelity are encased by solid lines drawn in orange, dashed in blue, or double lines in green, matching the scheme in figure B.1. The program will move to the next cycle of fidelity when the MTOM of the previous fidelity level has converged.

The structure of the convergence as is shown in this figure has been constructed manually. That is, no automated method is utilized to determine which modules are run in succession, apart from the two steps between the fidelity cycles described above. The current structure is based on the parameter dependencies of certain modules and the evaluation time of the modules. This will be revised in upcoming Initiator versions, which will also be ported from *Matlab* to the *Python* environment [55]. In this new framework, the order of module evaluations will be determined in-the-loop by considering computational time, fidelity and sensitivity from input to output of each module individually.

As an example of the current implementation, the Mission Analysis module will provide a fuel fraction (FF) and thereby a new MTOM which can be used in low fidelity methods, while it requires an aircraft design defined as a drag polar and the specific fuel consumption (SFC). These parameters could be estimated or assumed with low accuracy at the start of the convergence, making it possible to run the Mission Analysis almost immediately. However, it was decided to postpone this module until these parameters were obtained using more detailed analyses, because this module takes upwards of 20 seconds to complete. Hence, for the sake of computational time, this module should not be evaluated too often. In essence, this structure is a compromise between fidelity and speed. The connection between modules can be seen in figure B.3 by the Mission Analysis dependency on the Aerodynamic and Engine modules, plus the location of the module within the second fidelity cycle drawn in dashed blue.

Convergence problems

During the development and usage of the Initiator, several occurrences of poor convergence were observed. An example of such a case is given in figure B.2. Here we see a repeating trend in the prediction of the MTOM of the Learjet 45. It was expected for this error to reduce in magnitude in successive iterations, but the figure shows a cyclic behavior in the MTOM error that will not eliminate itself by a process of iteration.

The source of such problems has been found to be, on multiple occasions, in modules which take discrete steps in their result instead of a continuous change. For example, the number of wheels on the main landing gear is a discrete correlation with MTOM using the aircraft database. If the convergence passes over a certain empirical threshold the landing gear will use more or fewer wheels, resulting in a discrete step in the landing gear mass estimation.

Considering future development, robustness of the convergence requires that any module produces a continuous solution wherever possible. A consistent design can possibly not be reached if the discrete solution steps over the feasible point. In such cases, only increasing the convergence margin will help terminate an infinite cycle.

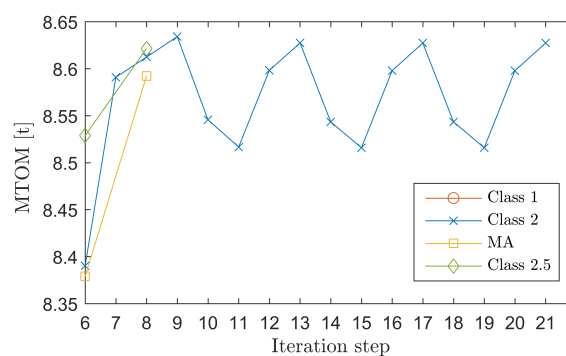
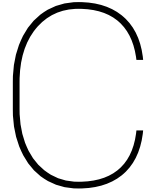


Figure B.2: Non-convergence of the MTOM in the Learjet 45 model

	Class 1 Weight Estimation	MTOM	MTOM	MTOM, FF					↩
		Wing Thrust Loading	W/S, T/W			T/W			
			Geometry Modules	Geometry	Geometry		Wing geometry	Fuselage geometry	
	OEM			Class 2 Weight Estimation	MTOM, FM, OEM	MTOM	Range		
	L/D, CD_{min} , CL_{min}	Polar	Polar		Aerodynamic modules		Polar	Loading	Loading
	SFC					Engine Model	SFC		
		MTOM		MTOM, FF			Mission Analysis		
				Wing weight (OEM)				EMWET	
	↶			Fuselage weight (OEM)					Fuselage Weight Estimation

Figure B.3: Initiator design convergence N2 chart



Initiator results

The results of five business jets produced by the Initiator (version 2.9) are given below. They were created by using the top level requirements of their respective reference aircraft. In addition, the results of three passenger aircraft are included to determine the influence of aircraft size on the results.

Table C.1: Laminar flow technology applied to the Cessna Citation II.

Transition Reynolds	0.1 10⁶	1.0 10⁶	3.0 10⁶	7.0 10⁶
MTOM [kg]	7275	7181 (-1.3%)	6805 (-6.5%)	6253 (-14.0%)
OEM [kg]	4538	4517 (-0.5%)	4376 (-3.6%)	4183 (-7.8%)
Fuel fraction	0.211	0.204 (-3.5%)	0.181 (-14.5%)	0.139 (-34.1%)
Harmonic fuel [kg]	1536	1463 (-4.8%)	1228 (-20.1%)	870 (-43.4%)
Maximum fuel [kg]	2666	2646 (-0.8%)	2428 (-8.9%)	2070 (-22.3%)
$(L/D)_{max}$	20.06	20.61 (2.8%)	22.67 (13.0%)	29.58 (47.5%)
C_{D_0}	0.0147	0.0135 (-8.1%)	0.0109 (-26.1%)	0.0059 (-59.8%)

Table C.2: Laminar flow technology applied to the Dassault Falcon 7X.

Transition Reynolds	0.1 10⁶	1.0 10⁶	3.0 10⁶	7.0 10⁶
MTOM [kg]	29695	28499 (-4.0%)	25599 (-13.8%)	21229 (-28.5%)
OEM [kg]	14722	14307 (-2.8%)	13249 (-10.0%)	11683 (-20.6%)
Fuel fraction	0.422	0.412 (-2.3%)	0.387 (-8.3%)	0.334 (-20.7%)
Harmonic fuel [kg]	12523	11742 (-6.2%)	9900 (-20.9%)	7096 (-43.3%)
Maximum fuel [kg]	12597	11724 (-6.9%)	9810 (-22.1%)	7077 (-43.8%)
$(L/D)_{max}$	21.40	21.94 (2.5%)	23.30 (8.9%)	27.05 (26.4%)
C_{D_0}	0.0143	0.0135 (-5.3%)	0.0119 (-16.9%)	0.0084 (-40.9%)

Table C.3: Laminar flow technology applied to the Learjet 45.

Transition Reynolds	0.1 10⁶	1.0 10⁶	3.0 10⁶	7.0 10⁶
MTOM [kg]	8261	8075 (-2.3%)	7534 (-8.8%)	6896 (-16.5%)
OEM [kg]	5278	5211 (-1.3%)	4960 (-6.0%)	4737 (-10.3%)
Fuel fraction	0.258	0.249 (-3.4%)	0.229 (-11.4%)	0.190 (-26.4%)
Harmonic fuel [kg]	2133	2013 (-5.6%)	1724 (-19.2%)	1310 (-38.6%)
Maximum fuel [kg]	2132	2129 (-0.2%)	1752 (-17.8%)	1623 (-23.9%)
$(L/D)_{max}$	18.31	18.82 (2.8%)	20.25 (10.6%)	24.50 (33.8%)
C_{D_0}	0.0167	0.0156 (-6.8%)	0.0132 (-21.1%)	0.0087 (-48.0%)

Table C.4: Laminar flow technology applied to the Gulfstream G650.

Transition Reynolds	0.1 10⁶	1.0 10⁶	3.0 10⁶	7.0 10⁶
MTOM [kg]	35964	35145 (-2.3%)	33217 (-7.6%)	29483 (-18.0%)
OEM [kg]	19091	18805 (-1.5%)	18068 (-5.4%)	16664 (-12.7%)
Fuel fraction	0.387	0.381 (-1.6%)	0.367 (-5.1%)	0.335 (-13.5%)
Harmonic fuel [kg]	13925	13392 (-3.8%)	12201 (-12.4%)	9872 (-29.1%)
Maximum fuel [kg]	14695	14358 (-2.3%)	13500 (-8.1%)	11920 (-18.9%)
$(L/D)_{max}$	18.40	18.67 (1.5%)	19.36 (5.2%)	21.10 (14.7%)
C_{D_0}	0.0138	0.0133 (-3.4%)	0.0123 (-11.0%)	0.0101 (-26.8%)

Table C.5: Laminar flow technology applied to the Fokker 100.

Transition Reynolds	0.1 10⁶	1.0 10⁶	3.0 10⁶	7.0 10⁶
MTOM [kg]	44012	43804 (-0.5%)	43341 (-1.5%)	42540 (-3.3%)
OEM [kg]	25544	25461 (-0.3%)	25288 (-1.0%)	25038 (-2.0%)
Fuel fraction	0.160	0.157 (-1.3%)	0.152 (-4.4%)	0.142 (-10.8%)
Harmonic fuel [kg]	7023	6898 (-1.8%)	6609 (-5.9%)	6057 (-13.7%)
Maximum fuel [kg]	13863	13802 (-0.4%)	13671 (-1.4%)	13476 (-2.8%)
$(L/D)_{max}$	18.93	19.10 (0.9%)	19.63 (3.7%)	20.91 (10.4%)
C_{D_0}	0.0150	0.0146 (-2.8%)	0.0137 (-8.8%)	0.0118 (-21.1%)

Table C.6: Laminar flow technology applied to the Airbus A320-200.

Transition Reynolds	0.1 10⁶	1.0 10⁶	3.0 10⁶	7.0 10⁶
MTOM [kg]	71083	70960 (-0.2%)	70096 (-1.4%)	68908 (-3.1%)
OEM [kg]	38333	38366 (0.1%)	37979 (-0.9%)	37611 (-1.9%)
Fuel fraction	0.172	0.170 (-1.1%)	0.165 (-3.8%)	0.156 (-9.1%)
Harmonic fuel [kg]	12213	12057 (-1.3%)	11581 (-5.2%)	10761 (-11.9%)
Maximum fuel [kg]	18846	18866 (0.1%)	18628 (-1.2%)	18356 (-2.6%)
$(L/D)_{max}$	19.10	19.31 (1.1%)	19.90 (4.2%)	21.33 (11.7%)
C_{D_0}	0.0167	0.0163 (-2.6%)	0.0152 (-8.8%)	0.0131 (-21.5%)

Table C.7: Laminar flow technology applied to the Boeing B767-300ER.

Transition Reynolds	0.1 10⁶	1.0 10⁶	3.0 10⁶	7.0 10⁶
MTOM [kg]	213736	212331 (-0.7%)	209820 (-1.8%)	204921 (-4.1%)
OEM [kg]	112143	111598 (-0.5%)	110614 (-1.4%)	108611 (-3.1%)
Fuel fraction	0.270	0.268 (-0.8%)	0.264 (-2.3%)	0.256 (-5.2%)
Harmonic fuel [kg]	57794	56934 (-1.5%)	55407 (-4.1%)	52511 (-9.1%)
Maximum fuel [kg]	101593	100733 (-0.8%)	99206 (-2.3%)	96310 (-5.2%)
$(L/D)_{max}$	19.04	19.20 (0.9%)	19.51 (2.5%)	20.18 (6.0%)
C_{D_0}	0.0119	0.0117 (-1.7%)	0.0112 (-5.2%)	0.0104 (-12.2%)

Table C.8: Laminar flow technology applied to the Boeing B747-100.

Transition Reynolds	0.1 10⁶	1.0 10⁶	3.0 10⁶	7.0 10⁶
MTOM [kg]	319043	318696 (-0.1%)	317184 (-0.6%)	313432 (-1.8%)
OEM [kg]	170023	169977 (-0.0%)	169485 (-0.3%)	168178 (-1.1%)
Fuel fraction	0.231	0.230 (-0.3%)	0.228 (-1.2%)	0.223 (-3.4%)
Harmonic fuel [kg]	73689	73389 (-0.4%)	72369 (-1.8%)	69924 (-5.1%)
Maximum fuel [kg]	149019	148719 (-0.2%)	147699 (-0.9%)	145254 (-2.5%)
$(L/D)_{max}$	18.78	18.87 (0.5%)	19.12 (1.8%)	19.59 (4.3%)
C_{D_0}	0.0118	0.0117 (-1.1%)	0.0114 (-3.7%)	0.0108 (-8.7%)

D

Eigenfunction mapping study

The diagrams created while searching for function parameters for mapping of the Chebyshev polynomials on the eigenfunctions are given below. They illustrate the convergence on feasible mapping parameters for the case of the velocity profile given in figure 2.5. The starting parameters of the analysis were given the (intentionally) coarse values of $NC=20$, y_{max} as half of the solution domain and y_i a quarter of the solution domain.

In each figure, the start of the "plateau" is selected as the minimum value for that parameter, repeated for four different Reynolds numbers. The same procedure is repeated for the next parameter while using the minimum value of the previous step. These values are logged in the titles of each subfigure. The entire process for this velocity profile has been included, which in total required a second iteration on each parameter to illustrate a convergence of the study.

Ultimately, the parameters converged to the values in table D.1. As can be seen, only the number of polynomials NC seemed to scale with Reynolds number. The actual mapping itself was independent of Reynolds number and was postulated to most likely depend on the type of stability (Tollmien-Schlichting in this case) and the velocity profile shape. Successive studies including crossflow instability and velocity profiles with larger boundary layers confirmed this hypothesis. The linear stability tool was consequently programmed with a constant y_{max} and a y_i dependent on the profile shape.

The total study also showed that the number of polynomials is not only dependent on the Reynolds number, but also scales with the magnitude of the amplification, i.e. the complex part of the eigenvalue α_i . As this value is not known a priori, no simple method could be constructed. This observation was one of the reasons contributing to the coarse grid/fine grid methodology of the linear stability tool.

Table D.1: Results of the eigenfunction mapping study.

Parameter	<i>Re</i> = 500	<i>Re</i> = 1000	<i>Re</i> = 2000	<i>Re</i> = 3500
NC	50	55	65	73
y_{max}	100	100	100	100
y_i	6	6	6	6

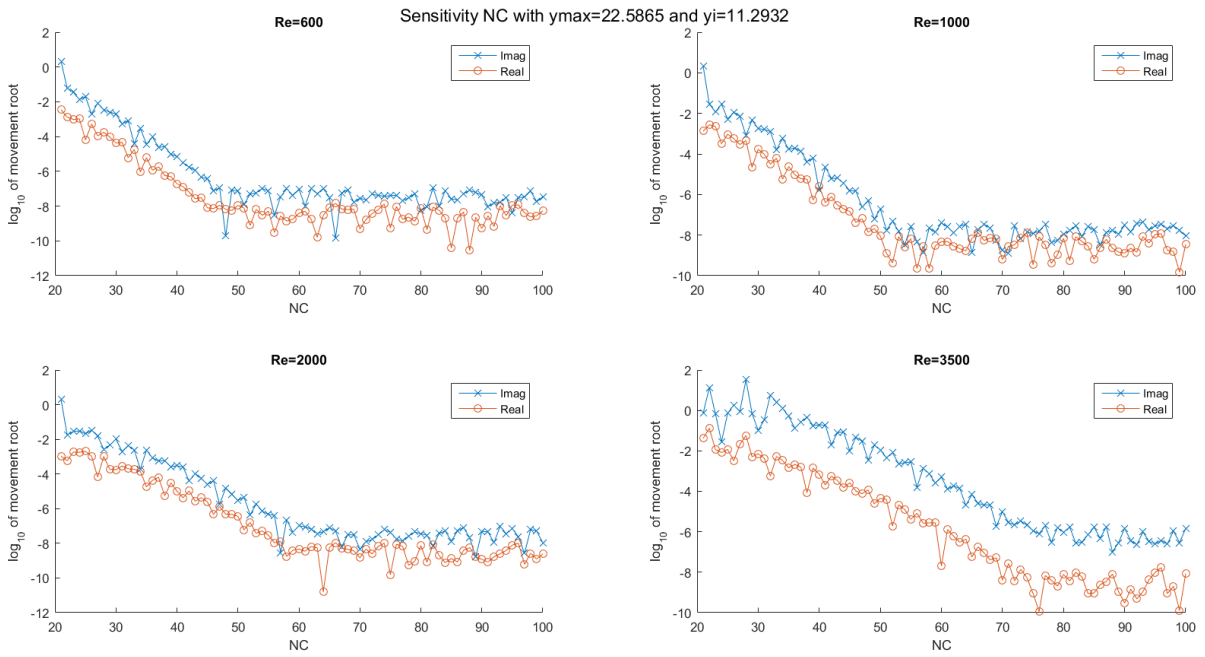


Figure D.1: NC parameter convergence 1

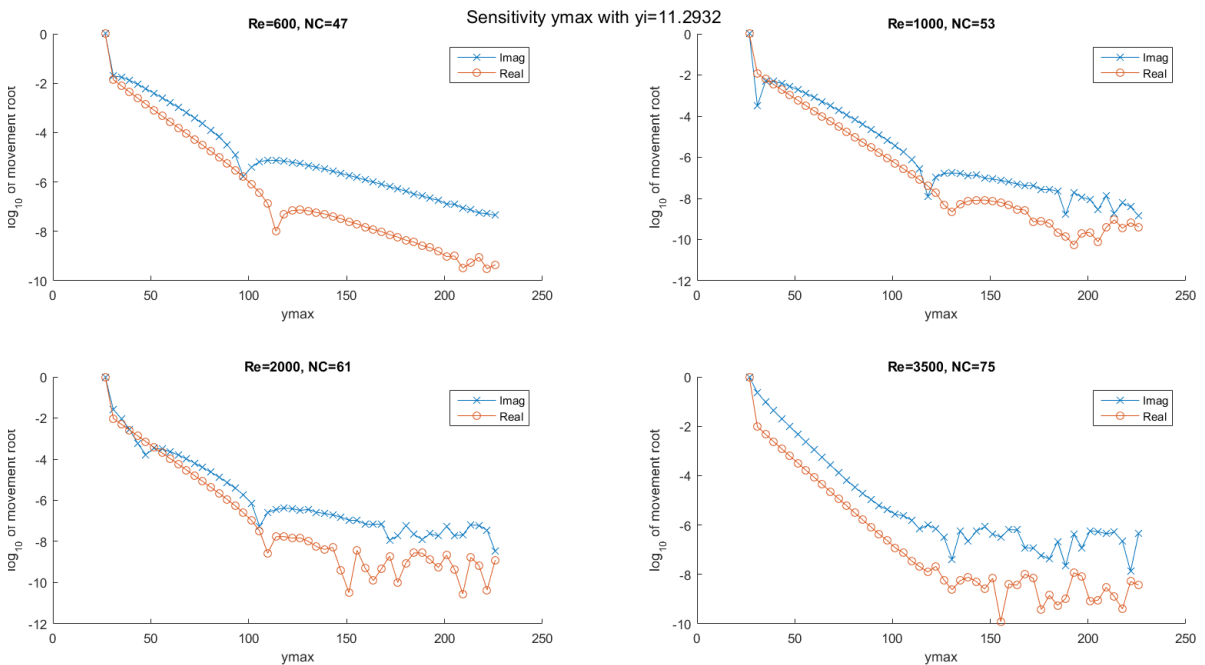


Figure D.2: y_{max} parameter convergence 1

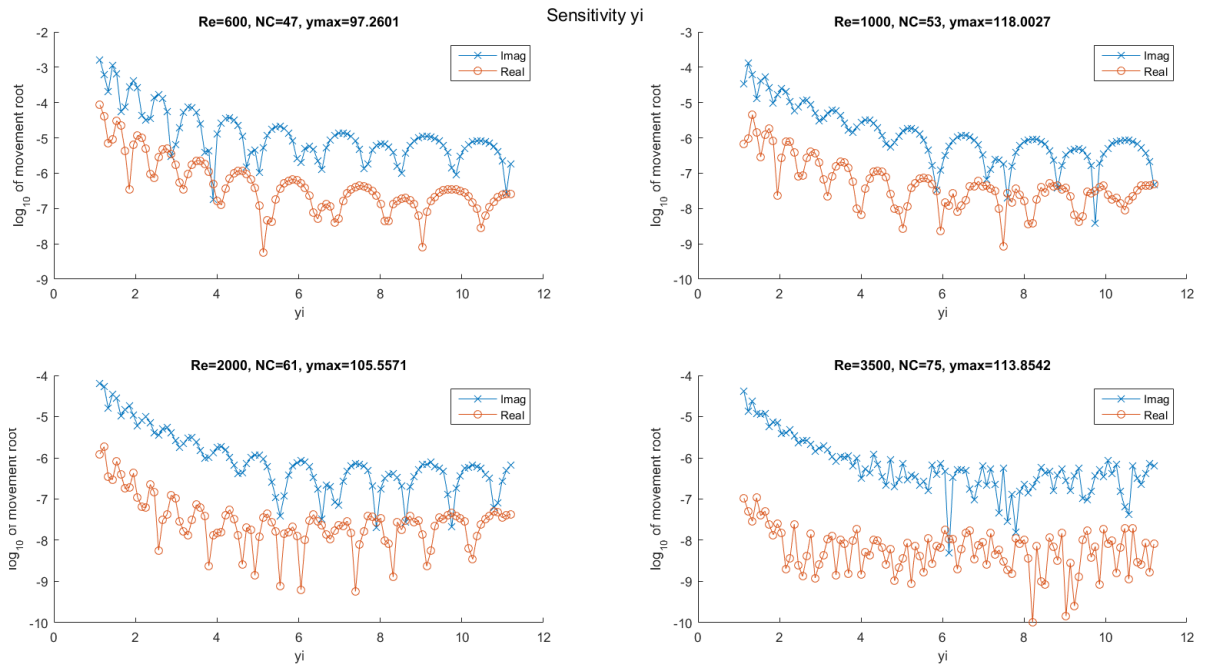


Figure D.3: y_i parameter convergence 1

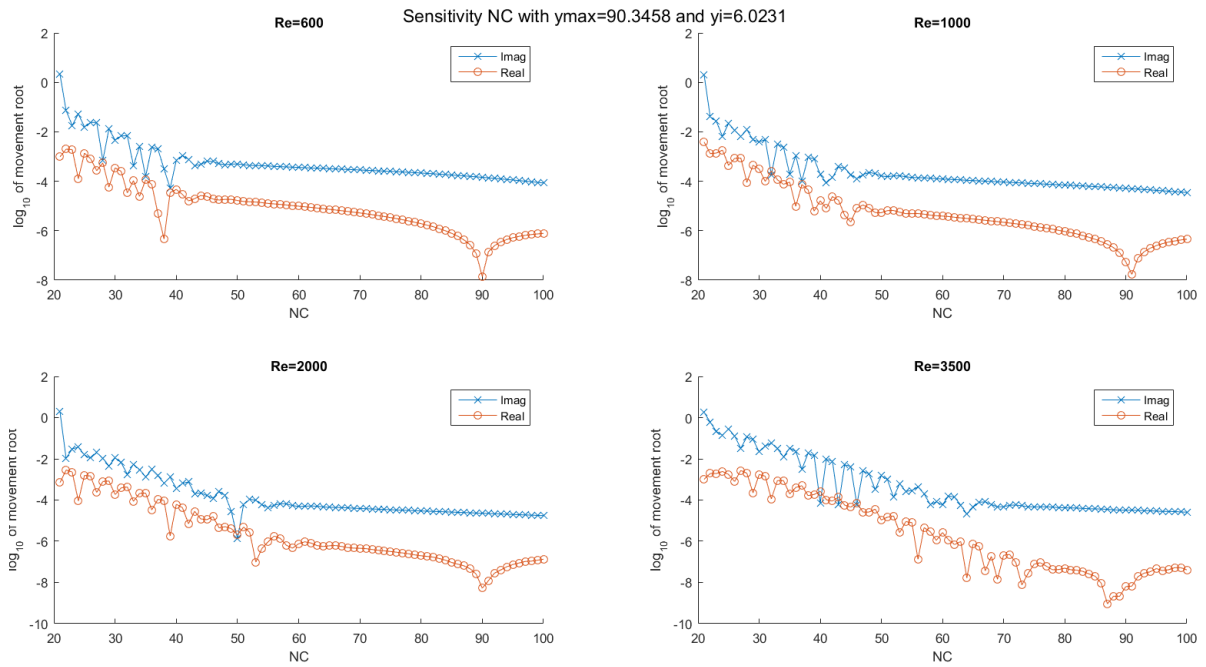


Figure D.4: NC parameter convergence 2

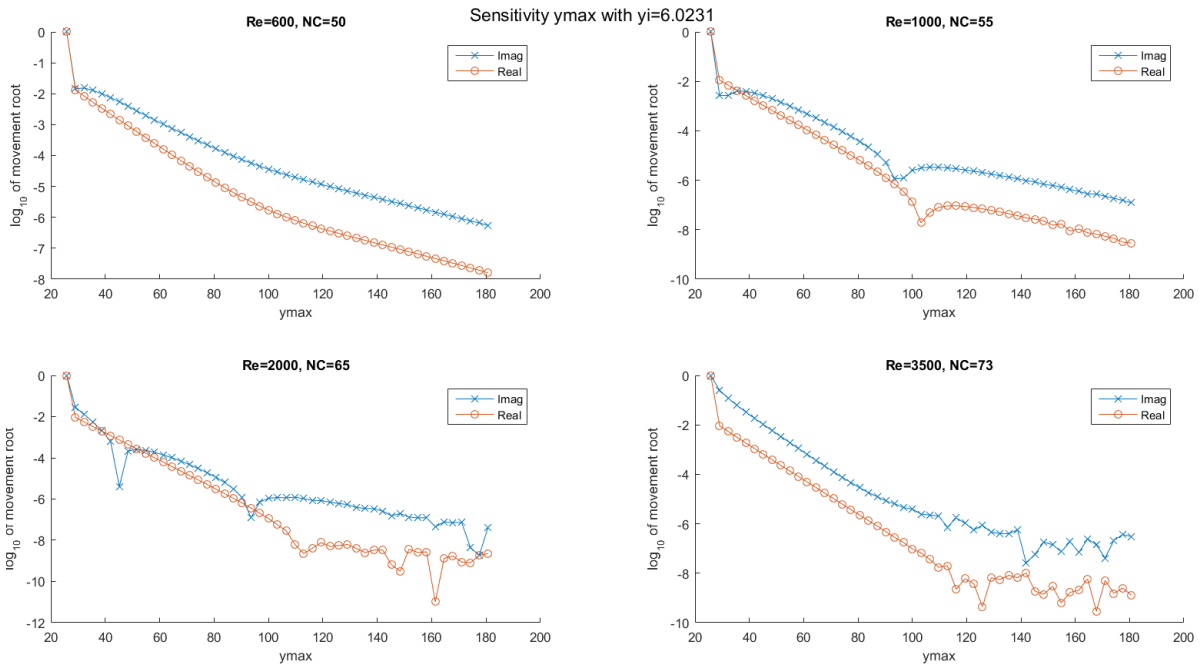


Figure D.5: y_{max} parameter convergence 2

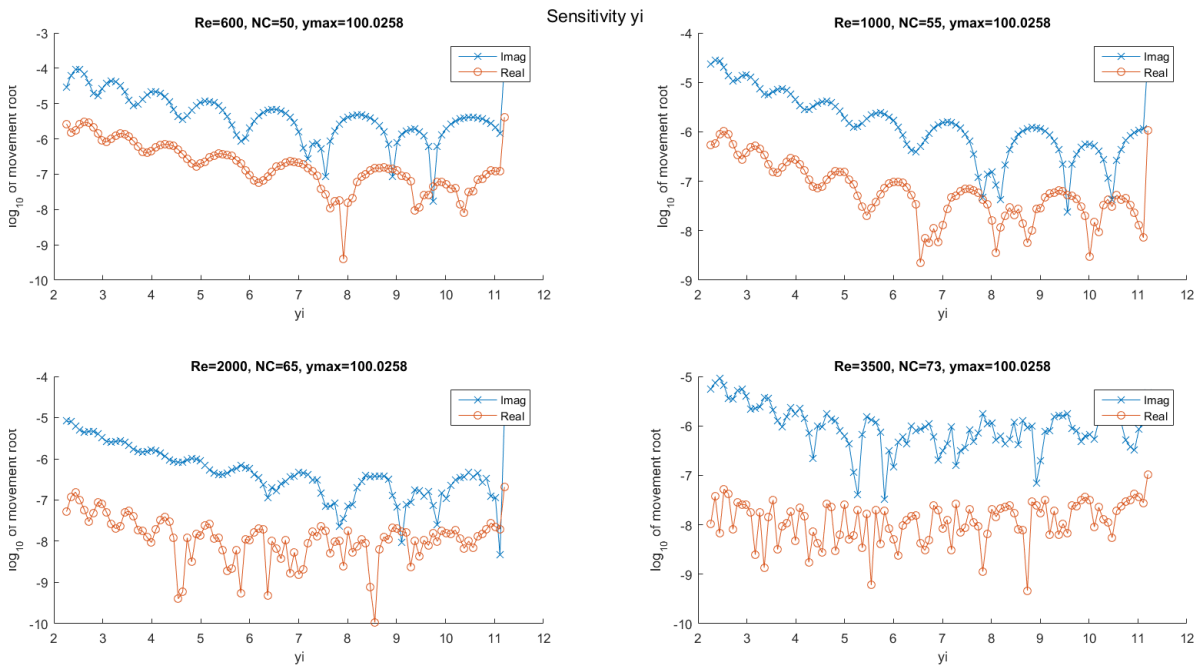


Figure D.6: y_i parameter convergence 2